School of Physics and Astronomy

Full stack development for gravitational waveform modelling

E. J. Fauchon-Jones

Submitted for the degree of Doctor of Philosophy
School of Physics and Astronomy
Cardiff University

7th December 2020

Summary of thesis

This thesis will present the results of several projects that each represent a specific stage in the life cycle of gravitational waveform model development.

This thesis is split into two parts. Part I is about gravitational waveform development projects. Part II is about numerical methods and software development. The material presented in Part II all started as components of larger GW research projects. However these numerical methods and software patterns each had features that potentially had application to other areas of GW research or beyond.

Part I will begin with Chapter 1 that presents the foundations of GW theory and the many frameworks and tools that exist to enable contemporary GW research. Chapter 2 will present a new GW model for neutron star black hole binary systems. Chapter 3 will present a new catalogue of numerical relativity (NR) simulations of binary black holes that will be used to construct an improved precessing GW model. Chapter 4 will present the results of investigations into GW model and NR accuracy requirements for third generation detectors and what is necessary to enable the next generation of GW models.

Part II will begin with Chapter 5 that presents new linear modelling techniques that have been applied to GW modelling efforts. Chapter 6 will present the development of a repository of NR simulations for the LVC and the associated continuous integration framework. Finally Chapter 7 will present the development of a web-based service that has been used to perform on demand analysis of NR simulations.

The beginning of the title of this thesis, *Full stack development*, is assumed from *full stack web developers* and reflects the idea that this thesis presents material from low level numerical methods up to high level parameter estimation.

Contents

List of Figures

List of Tables

Once upon a time, in a land not so far away, and a time happening right now, there were two wanderers, a Brother and a Brother, a soul guarding a soul. This is for my Brother, who gives my life meaning.

Acknowledgments

I would like to acknowledge that my PhD was supported by the European Research Council Consolidator Grant 647839. I will forever be grateful to have been given the opportunity to explore this field because of this support.

Normally I spend days writing acknowledgements, today I have less than 1 hour to prepare. I hope that anyone who I miss in these acknowledgements knows that you will always have a place in my heart, and hopefully my examiners will allow me to add anyone I know I have missed.

I would never have reached this far without the support of the truly amazing person, my supervisor Mark Hannam. Twice he believed in me enough to allow me to come to Cardiff, first as an intern, and then as a PhD student. I am honoured to have been your student, and I only hope that one day I am able to repay you for all the kindness you have shown me.

I am so grateful to have fallen in with a crowd of amazing people when I came to Cardiff as an intern, Liz, Ronaldas, Franziska and Eve. The wonderful experiences then told me that Cardiff could be my home if I was lucky enough to return, and thankfully they were all in Cardiff (although not all at the same time) when I did return.

When I started my PhD we did not have permanent desks. Instead for several months all new PhD students worked in a computer room. This was a blessing in disguise, I got to know everyone so well, and apart from a few rocky starts (my own fault) I am so grateful to have started my PhD life like this. Thank you Aris, Chinmay, Eleni, Iain, Rosie, and Ruth for being wonderful friends.

There are many people in the Gravitational Waves research group who have supported. Seb, you came before me, and showed me the way, thank you so much. Max always had a wink for me, and I am so grateful for that. Talking tech with Paul was always amazing, and so are you Paul. My life is better for having Lionel in it.

Many of my friends also started as PhD after me and I am so honoured to have been able to work with them all. For the times when I was able to pass on my knowledge I am so grateful. I was never a master, and never really a teacher, but to paraphrase Yoda, I am what you have grown beyond. Eleanor, Charlie, Dave, Rhys, Virginia, Vasilis, and everyone who I have forgotten, thank you so much for sharing your lives with me.

To every other amazing person in the gravitational waves research group, thank you for creating an amazing place. It does not matter if I have know you for many years or a few months, everyone of you has a place in my heart.

My family have always supported everything I do. We are incredibly close, my Mother is without question my best friend, there is no one in the world who I respect more than my Father who has sacrificed so much to ensure that we could aspire to whatever we could dream of, and my Brother who I was born along side shares a soul with me. I have been away from them for far to long. I am not sure what the future hold for me, but I know they must be a part of my future.

Collaborative work

The following sections of this thesis contain work that has been co-authored with others, are results of collaborative work or builds upon work started by others:

- Chapter 2 presents the gravitational waveform model `PhenomNSBH`. This work was led by Edward Fauchon-Jones and Jonathan Thompson. The main contributions by Edward Fauchon-Jones were initial prototyping and development of the model, implementation in LALSuite and paper writing. The material presented in Chapter 2 has been published in [264].
- Chapter 3 presents a new catalog of numerical relativity simulations produced by `BAM`. This work was initially led by Edward Fauchon-Jones. The main contributions by Edward Fauchon-Jones were managing the simulations, preparing workflow environments for running `BAM`, and paper writing. Contributions were made to the planning for all chapters, with specific contributions to introductory material and detailed descriptions of the simulations. The material presented in Chapter 3 is currently in preparation for publication as part of a larger work that includes more detailed convergence analysis and mismatch analysis against waveform models [120].
- Chapter 5 presents a numerical method for fitting rational functions to data. This work was originally published as part of a larger work on producing new fits for quasi-normal mode data [184]. Edward Fauchon-Jones contributed to the development of this method and to the section of the publication that describes this method and relevant supporting text that describes this method.

Part I

Gravitational waveform development

Chapter 1

Foundations

This thesis is presented as an anthology of various related projects, each describing contributions to the research area of model development for gravitational waves generated by compact binary coalescence. There are three key research questions that are considered. How can neutron star black hole gravitational wave models be improved? How can precessing binary black hole models be improved? What model improvements need to be made for data analysis at next generation sensitivities? To address these questions this thesis is split into two parts. Part I presents three projects, each designed to address one of these questions. Part II presents several tools that were developed to facilitate the projects of Part I. Each of the tools described in Part II are intended to be used at different stages in the lifecycle of a gravitational wave model. However each tool also has the potential for use beyond their intended scope and as such were decoupled from the research described in Part I.

Chapter 2 addresses the first research question by presenting a new model for the merger of neutron star black hole systems, building on previous theoretical work, alongside new expressions and construction patterns, including a new black hole ringdown model developed using the method described in Chapter 5. Chapter 3 describes a new collection of numerical relativity simulations produced in a workflow using the analysis tool described in Chapter 7. The primary purpose of these simulations is to support the development of a new phenomenological precessing gravitational wave model, and addresses the second research question. To address the final research question, Chapter 4 presents results of the applicability of a current binary black hole model for a future gravitational wave detector. The numerical relativity data used for analysis in Chapter 2 and Chapter 4 was processed using the numerical relativity validation system described in Chapter 6. For the rest of Chapter 1 material on the foundations of gravitational wave model development will be presented to support the rest of this thesis.

1.1 General relativity

At the turn of the 20th century great change was taking place to redefine our understanding of the laws of nature. Building on the work of many scientists from the end of the 19th

century, most notably the work of Hendrik Lorentz and Henri Poincaré, Albert Einstein developed the theory of *special relativity* [111]. This axiomatised two ideas, the *Relativity principle* and the *Principle of Constant Speed of Light*. While a great achievement in itself that addressed many issues with similar theories of the time, it did not directly address the concept of gravity. Over the subsequent decade Einstein sought to incorporate gravity in a theory of relativity. Once again progress was made over this decade by many scientists including the influential work on relativity by Hermann Minkowski. Inspired by the work of Bernhard Riemann on differentiable manifolds from the previous century, Einstein published a series of papers in 1915 [113, 115, 112, 114] which were followed up in greater detail in Einstein's exposé of this work the following year [116]. Together these works formed Einstein's theory of *general relativity*.

General relativity re-established gravity not as a force but a result of *curvature* of a differentiable manifold that represents the three dimensions of space and single dimension of time as a single object called *spacetime*. Through this new mathematical framework in which to perform calculations involving gravity, general relativity has been used to explain previous anomalies such as the advance of the perihelion of Mercury [112] and successfully passed experimental tests such as the deflection of light by the Sun observed during a total eclipse in 1919 [110].

The body of work surrounding general relativity is vast. This thesis is concerned with *gravitational waves* which is just one of the many branches of general relativity. Even the mathematical foundations of general relativity are too much to recapitulate here. However the bare necessities that are required to support this thesis will be summarized in the rest of this section. This will be mostly based on the excellent pedagogical treatment of general relativity by Sean Carroll [90]. *Gravitation* by Charles Misner, Kip Thorne, and John Wheeler [199] or *General Relativity* by Robert Wald [277] are great alternatives that often provide more mathematical details to complement [90].

General relativity is built on a four-dimensional Lorentzian manifold M equipped with a symmetric metric tensor $g_{\mu\nu}$ and endowed with a Levi-Civita connection. The set $(M, g_{\mu\nu})$ then represents spacetime. For this thesis the convention $(-,+,+,+)$ will be used for the metric signature. The metric is of fundamental importance to calculations within GR including the determination of causality and computation of path lengths on the manifold M. In general the components of $g_{\mu\nu}$ will be intractable as will be seen in Sec. 1.5, however an important instance is the metric of flat spacetime otherwise know as *Minkowski space* that has the metric

$$g_{\mu\nu} = \eta_{\mu\nu} \equiv \begin{pmatrix} -1 & 0 & 0 & 0 \\ 0 & 1 & 0 & 0 \\ 0 & 0 & 1 & 0 \\ 0 & 0 & 0 & 1 \end{pmatrix}. \tag{1.1}$$

It is often useful to express the metric in terms of the *line element* which is much more compact,

$$ds^2 = g_{\mu\nu} dx^\mu dx^\nu. \tag{1.2}$$

Depending on the level of rigour that is applied to this object, it can be interpreted in different ways. However a useful interpretation is as an infinitesimal distance ds induced by infinitesimal changes dx^μ along the coordinates x^μ. Because of the line element's interchangeability with the metric, it is often also referred to casually as the metric.

The geometrical concept of curvature is of central importance to GR and is represented by the *Riemann curvature tensor* $R^\rho{}_{\sigma\mu\nu}$. The metric alone is not sufficient to define curvature. To define curvature within GR a *covariant derivative* ∇_μ is required which acts on a vector V^ν according to

$$\nabla_\mu V^\nu = \partial_\mu V^\nu + \Gamma^\nu_{\mu\lambda} V^\lambda. \tag{1.3}$$

where the symbols $\Gamma^\nu_{\mu\lambda}$ are known as *connection coefficients*. The Riemann curvature tensor $R^\rho{}_{\sigma\mu\nu}$ may then be defined through the equation

$$\nabla_\mu \nabla_\nu V^\rho - \nabla_\nu \nabla_\mu V^\rho = R^\rho{}_{\sigma\mu\nu} V^\sigma. \tag{1.4}$$

This equation can be interpreted as the parallel transport of the vector around a loop and as such encodes in the Riemann tensor the curvature of the manifold.

While in general there is no unique definition of the covariant derivative on a manifold, the Levi-Civita connection that is chosen for GR does allow it to be defined uniquely. It requires the following,

$$\Gamma^\lambda_{\mu\nu} - \Gamma^\lambda_{\mu\nu} = 0, \qquad \text{(torsion-free)}$$

$$\nabla_\rho g_{\mu\nu} = 0. \qquad \text{(metric compatible)}$$

With these requirements imposed the connection coefficients may be expressed in terms of the metric

$$\Gamma^\sigma_{\mu\nu} = \frac{1}{2} g^{\sigma\rho} \left(\partial_\mu g_{\nu\rho} + \partial_\nu g_{\rho\mu} - \partial_\rho g_{\mu\nu} \right), \tag{1.5}$$

and when written in this form the connection coefficients are known as the *Christoffel symbols*. The Riemann tensor can then be expressed in terms of partial derivatives and Christoffel symbols

$$R^\rho{}_{\sigma\mu\nu} = \partial_\mu \Gamma^\rho_{\nu\sigma} - \partial_\nu \Gamma^\rho_{\mu\sigma} + \Gamma^\rho_{\mu\lambda} \Gamma^\lambda_{\nu\sigma} - \Gamma^\rho_{\nu\lambda} \Gamma^\lambda_{\mu\sigma}. \tag{1.6}$$

At the heart of GR is the relationship beautifully captured by John Wheeler, *"Space tells matter how to move. Matter tells space how to curve"* [199]. Matter is encoded mathematically in the *energy-momentum tensor* $T_{\mu\nu}$ and spacetime is represented by the *Einstein tensor*

$$G_{\mu\nu} = R_{\mu\nu} - \frac{1}{2} R g_{\mu\nu}, \tag{1.7}$$

$$R_{\mu\nu} = R^\lambda{}_{\mu\lambda\nu}, \tag{1.8}$$

$$R = R^\mu{}_\mu, \tag{1.9}$$

where $R_{\mu\nu}$ is the *Ricci curvature tensor* and R is the *Ricci scalar*. The relationship between these objects is finally expressed in the *Einstein field equations* (EFE),

$$G_{\mu\nu} = 8\pi T_{\mu\nu}. \tag{1.10}$$

Taking the trace of the field equations by contracting with the metric shows that $R = -8\pi GT$ where $T \equiv T^{\mu}{}_{\mu}$. This allows the field equations to be re-expressed as

$$R_{\mu\nu} = 8\pi \left(T_{\mu\nu} - \frac{1}{2} T g_{\mu\nu} \right). \tag{1.11}$$

While this is not particularly interesting by itself, in the context of gravitational waves it exposes a particularly appealing form of the field equations. Much of the theory of gravitational waves is concerned with calculations in vacuum, where $T_{\mu\nu} = 0$. The *vacuum Einstein field equations* then reduce to the particularly simple form

$$R_{\mu\nu} = 0. \tag{1.12}$$

In the rest of this chapter the theory described in this section will be used to introduce the concept of gravitational waves.

1.2 Foundations of gravitational waves

As Einstein completed his general theory of relativity he began to explore how candidate gravitational fields might propagate in GR [117, 118]. The results demonstrated not only that gravitational fields could propagate as plane waves, but also how a *gravitational wave* (GW) could be generated from a physical system, and the effect a GW would have on mechanical systems. This section will summarize the theory of how GWs manifest in GR and the theoretical systems that can generate them.

1.2.1 Emergence of gravitational waves

Consider a spacetime that deviates by a small amount from flat Minkowski spacetime. This can be written as a small perturbation $h_{\mu\nu}$, where $|h_{\mu\nu}| \ll 1$, to Minkowski spacetime,

$$g_{\mu\nu} = \eta_{\mu\nu} + h_{\mu\nu}. \tag{1.13}$$

Substituting this expression into the EFE Eq. (1.10) and expanding to linear order in $h_{\mu\nu}$ gives the linearized EFE,

$$\begin{aligned} \partial^{\rho}\partial_{\mu}h_{\nu\rho} + \partial^{\rho}\partial_{\nu}h_{\mu\rho} - \partial^{\rho}\partial_{\rho}h_{\mu\nu} - \partial_{\mu}\partial_{\nu}h \\ - \eta_{\mu\nu}\partial^{\rho}\partial^{\sigma}h_{\rho\sigma} + \eta_{\mu\nu}\partial^{\rho}\partial_{\rho}h = 16\pi T_{\mu\nu}. \end{aligned} \tag{1.14}$$

By introducing the *trace-reversed* perturbation,

$$\bar{h}_{\mu\nu} = h_{\mu\nu} - \frac{1}{2} h \eta_{\mu\nu}, \tag{1.15}$$

and imposing the *Lorentz gauge* condition,

$$\partial^{\nu} \bar{h}_{\mu\nu} = 0, \tag{1.16}$$

the linearized EFE reduce to a much simpler system in $\bar{h}_{\mu\nu}$,

$$\partial^{\rho} \partial_{\rho} \bar{h}_{\mu\nu} = -16\pi T_{\mu\nu}. \tag{1.17}$$

The simplified form of the linearized EFE Eq. (1.17) is the wave equation. The first task is to understand what gravitational fields propagating in vacuum look like. The vacuum solutions can easily be verified to be the complex homogeneous solutions of the wave equation,

$$\bar{h}_{\mu\nu} = A_{\mu\nu} e^{i k_{\rho} x^{\rho}}, \tag{1.18}$$

where the wave vector k^{μ} is a null vector $k^{\mu} k_{\mu} = 0$ and can be written as $k^{\mu} = (\omega, k^{i})$ to emphasize that the time component of the vector represents the frequency of the wave solution. In vacuum it can be shown that the additional *transverse-traceless* (TT) gauge conditions $\bar{h} = 0$ and $h_{0\mu} = 0$ are consistent with the Lorentz gauge condition Eq. (1.16). Applying these gauge conditions implies that $h \equiv \bar{h}$, $A_{0\mu} = 0$, and for the solution Eq. (1.18) to satisfy the Lorentz gauge condition it is necessary that,

$$A_{\mu\nu} k^{\mu} = 0. \tag{1.19}$$

Without loss of generality the wave vector can be chosen to point along the spatial z-axis $k^{\mu} \equiv (\omega, 0, 0, k^{3}) = (\omega, 0, 0, \omega)$, where the second equality is because k^{μ} is null. Expanding Eq. (1.18) in this context,

$$\begin{aligned} 0 &= A_{\mu\nu} k^{\mu}, \\ &= A_{0\nu} k^{0} + A_{3\nu} k^{3}, \qquad (1.20) \\ &= A_{3\nu} \omega, \qquad (1.21) \end{aligned}$$

which implies that $A_{3\nu} = A_{\nu 3} = 0$. All together the TT gauge vacuum solution simplifies to,

$$h_{\mu\nu} = \begin{pmatrix} 0 & 0 & 0 & 0 \\ 0 & A_{11} & A_{12} & 0 \\ 0 & A_{12} & -A_{11} & 0 \\ 0 & 0 & 0 & 0 \end{pmatrix} e^{i\omega(z-t)} = \begin{pmatrix} 0 & 0 & 0 & 0 \\ 0 & h_{+} & h_{\times} & 0 \\ 0 & h_{\times} & -h_{+} & 0 \\ 0 & 0 & 0 & 0 \end{pmatrix}. \tag{1.22}$$

The final form of the solution for the perturbation $h_{\mu\nu}$ expresses the important results that vacuum solutions are characterized by only two independent components, h_{+} and $h_{\times}$, that

are called *polarizations*.

1.2.2 Gravitational wave generation in linearized general relativity

Having demonstrated that it is possible for gravitational waves to propagate through space-time vacuum the next task is to understand what sort of systems could produce gravitational waves. The following results summarize the work surrounding the quadrupole formula, for more details please see [90, 128]. Starting from Eq. (1.17) in the non-vacuum case the general solution can be written as,

$$\bar{h}_{\mu\nu}(t,\boldsymbol{x}) = 4 \iiint \frac{T_{\mu\nu}(t-|\boldsymbol{x}-\boldsymbol{y}|,\boldsymbol{y})}{|\boldsymbol{x}-\boldsymbol{y}|} d^3y, \tag{1.23}$$

where the 4-vector is explicitly separated into its temporal and spatial components $x^\mu \equiv (t,\boldsymbol{x}) \equiv (t,x^i)$. If the characteristic velocity of the volume is not fast such that $|v/c| \ll 1$ and the solution is observed at large distances such that $r \equiv |\boldsymbol{x}-\boldsymbol{y}|$ is approximately constant, Eq. (1.23) can be simplified to,

$$\bar{h}_{\mu\nu}(t,\boldsymbol{x}) = \frac{4}{r} \iiint T_{\mu\nu}(t-r,\boldsymbol{y}) d^3y. \tag{1.24}$$

The energy-momentum tensor must be conserved $\partial_\mu T^{\mu\nu} = 0$. Using this it can be shown that [128],

$$\partial_t^2 \left(T^{tt} x^i x^j\right) = \partial_k \partial_l \left(T^{kl} x^i x^j\right) - 2\partial_k \left(T^{ik} x^j + T^{kj} x^i\right) + 2T^{ij}, \tag{1.25}$$

where indices (i,j,k,l) are used for spatial tensor components and summation is performed over spatial indices (k,l). The energy-momentum tensor is of order of the perturbation $h_{\mu\nu}$ which means that its tensor indices can be raised and lowered with $\eta_{\mu\nu}$. It follows that the spatial components of the energy-momentum tensor satisfy $T_{ij} \equiv T^{ij}$. The spatial components of Eq. (1.24) can then be written as,

$$\begin{aligned}
\frac{4}{r} \iiint T_{ij}(t-r,\boldsymbol{y}) d^3y &= \frac{2}{r} \iiint \Big(\partial_t^2 (T^{tt} y^i y^j) + 2\partial_k (T^{ik} y^j + T^{kj} y^i) \\
&\qquad - \partial_k \partial_l (T^{kl} y^i y^j)\Big) d^3y, \qquad (1.26) \\
&= \frac{2}{r} \iiint \partial_t^2 (T^{tt} y^i y^j) d^3y + \oiint 2n_k (T^{ik} y^j + T^{kj} y^i) dS \qquad (1.27) \\
&\qquad - \oiint n_k \partial_l (T^{kl} y^i y^j) dS, \\
&= \frac{2}{r} \frac{\partial^2}{\partial t^2} \iiint T^{tt}(t-r,\boldsymbol{y}) y^i y^j d^3y, \qquad (1.28)
\end{aligned}$$

where the surfaces integrals induced by the divergence theorem vanish because at the assumed large distance r the surface will be in vacuum. In the assumed slow motion approximation the T^{tt} component of the energy-momentum tensor is approximately the mass density ρ. The *second moment of mass tensor* or *quadrupole moment tensor* can be

defined as,

$$I_{ij}(t) = \iiint \rho(t, \boldsymbol{x}) x^i x^j d^3x. \tag{1.29}$$

In the limit of observing the solution at infinite distance and assuming slow motion of the source, the general solution of the linearized EFE can then be written as *Einstein's quadrupole formula*,

$$\bar{h}_{ij}(t, \boldsymbol{x}) = \frac{2}{r} \frac{\partial^2}{\partial t^2} I_{ij}(t - r). \tag{1.30}$$

The quadrupole formula is important because it provides information about the types of sources that can produce GWs. It indicates that GWs come from sources of accelerating mass that have a non-vanishing quadrupole moment. For example a spinning spherical body with uniformly distributed mass produces no GW because its quadrupole moment is zero. In contrast the quadrupole moment for a binary system does not vanish and so does produce GWs. Consider such a binary system as a pair of point particles with equal mass in a circular orbit of radius R in the xy-plane. The Newtonian trajectories of the first body $\boldsymbol{r}_1$ and the second body $\boldsymbol{r}_2$ can be written as,

$$\boldsymbol{r}_1 = R \begin{pmatrix} \cos(\Omega t) \\ \sin(\Omega t) \\ 0 \end{pmatrix}, \qquad \boldsymbol{r}_2 = -R \begin{pmatrix} \cos(\Omega t) \\ \sin(\Omega t) \\ 0 \end{pmatrix}, \tag{1.31}$$

where the orbital frequency of a circular binary is given by $\Omega = \sqrt{M/4R^3}$, and the mass density of the system can be written as,

$$\rho(t, \boldsymbol{x}) = M\delta(x^3)\Big(\delta(x^1 - r_{1,1})\delta(x^2 - r_{1,2}) + \delta(x^1 - r_{2,1})\delta(x^2 - r_{2,2})\Big). \tag{1.32}$$

The spatial quadrupole moment components can then be calculated as,

$$I_{11} = MR^2(1 + \cos(2\Omega t)), \tag{1.33}$$
$$I_{22} = MR^2(1 - \cos(2\Omega t)), \tag{1.34}$$
$$I_{12} = I_{21} = MR^2 \sin(2\Omega t), \tag{1.35}$$
$$I_{i3} = I_{3i} = 0, \tag{1.36}$$

which implies the quadrupole time derivatives are,

$$\frac{\partial^2 I_{11}}{\partial t^2} = -4M\Omega^2 R^2 \cos(2\Omega t), \tag{1.37}$$
$$\frac{\partial^2 I_{22}}{\partial t^2} = 4M\Omega^2 R^2 \cos(2\Omega t), \tag{1.38}$$
$$\frac{\partial^2 I_{12}}{\partial t^2} = -4M\Omega^2 R^2 \sin(2\Omega t). \tag{1.39}$$

The resulting spatial component solutions of the trace-reversed perturbation can then be

written as,

$$h_{ij} = \frac{8}{r} M\Omega^2 R^2 \begin{pmatrix} -\cos(2\Omega t) & -\sin(2\Omega t) & 0 \\ -\sin(2\Omega t) & \cos(2\Omega t) & 0 \\ 0 & 0 & 0 \end{pmatrix} \tag{1.40}$$

This expression for GWs is not the end of the story. What has been described here are conservative dynamics assuming Newtonian physics. This does not yet describe the characteristic inspiral of a relativistic binary system. Einstein went on to explain this feature as a result of the orbit losing energy as GW are emitted. However since the presentation of the quadrupole formula new methods have been applied to go beyond the Newtonian approximations required to derive Eq. (1.40) and these will be explored in Sec. 1.6.

1.3 Detecting gravitational waves

Since 1975 the Hulse-Taylor pulsar [156] has provided indirect evidence for gravitational waves through radio observations. In 2015 direct observations of gravitational waves were made with ground-based detectors. What sort of a device constructed on Earth could be used to observe a gravitational wave described by Eq. (1.22)? In this section this question will be addressed. The results will motivate the types of candidate sources that could generate GWs detectable on Earth which will be explored in Sec. 1.4.

1.3.1 Detector response to gravitational waves

The results of Sec. 1.2 demonstrate that in general gravitational waves will be plane waves composed of a plus and cross polarisation $h_+(t)$ and $h_\times(t)$. Sec. 1.2 also implies that it is theoretically possible to detect the effect of these polarisations by observing the change in proper distance between points as gravitational waves travel through. As a simple example consider the metric of a GW in the transverse-traceless gauge, where the plane wave is propagating along the z axis and only the effect of the h_+ polarisation is considered,

$$ds^2 = -dt^2 + (1 + h_+)dx^2 + (1 - h_+)dy^2 + dx^2. \tag{1.41}$$

If the change in just the x axis is considered then the proper length $L \equiv L_0 + \Delta L$ is given by the integral from the origin out to the coordinate length L_0,

$$L(t) = \int_0^{L_0} \sqrt{g_{\mu\nu} dx^\mu dx^\nu} = \int_0^{L_0} dx \sqrt{1 + h_+} = L_0 \sqrt{1 + h_+} \tag{1.42}$$

$$\approx L_0(1 + h_+). \tag{1.43}$$

This implies that the relative change in proper length is equal to the h_+ polarisation of the GW. This simple argument used the fact that GW amplitudes are very small to expand the square root term. It is also assumed that the *long-wavelength approximation* [244] is valid. This means that the wavelength of GWs is much larger than the coordinate length L_0 such

that the GW polarisations are approximately equal and constant over the path integral.

Measuring such changes over a single path would require at least one incredibly accurate clock, which limits the types of measurements that could be made. However interferometry provides a mechanism to overcome this barrier, a *Michelson interferometers* [197]. A *Michelson Interferometer* effectively measures the relative changes in proper distance $\Delta L/L_0 \approx h_+$ between two paths without the need for any clock. Based on this idea the first generation of GW interferometers LIGO [4, 46, 254], VIRGO [28, 29], GEO 600 [48], and TAMA [50] were constructed. Since then second generation detectors have been built and begun operation with Advanced LIGO [47, 3] and Advanced VIRGO [30, 31] making the first direct detection of gravitational waves and now KAGRA [255, 56] has also joined the second generation of ground based GW detectors. While GEO 600 has by construction not been able to reach the same levels of sensitivity as the primary two LIGO detectors, it has continued to successfully operate and has received many upgrades and acts a a critical pathfinder for the primary detectors [190, 189, 32, 106]. For the rest of this thesis the output time dependant signal from a GW detector will be symbolized as $d(t)$.

The small amplitude approximation is extremely well satisfied for GWs observed by these ground based detectors with typical gravitational wave amplitudes of $\sim 10^{-21}$ [237]. While the long-wavelength approximation is mostly satisfied, for higher frequency signals $> 1\mathrm{kHz}$ is has been shown that this approximation can lead to errors greater than 2% [62, 228]. While it is important to consider the validity of the long-wavelength approximation as ground based GW detectors are improved and upgraded, for this thesis it will be assumed that the long-wavelength approximation is valid for all results discussed.

GWs will not in general be aligned with detectors in such a way as to only observe a single polarisation. In general the detector output $d(t)$ will contain the *detector response* or *antenna response* which will be a combination of the two polarisations,

$$h(t) \equiv h_{\mathrm{resp}}(t) \equiv F_+ h_+(t) + F_\times h_\times(t) \tag{1.44}$$

where the coefficients $(F_+, F_\times)$ are called *antenna pattern* functions. These depend on the three dimensions of orientation a GW source can have with respect to a detector, its relative location in the sky and the rotation about the line of sight between the source and detector. For an L-shaped detector like the current generation of ground based GW detectors the antenna pattern written in spherical polar coordinates (θ, ϕ) and line-of-sight polarisation ψ becomes,

$$\begin{aligned} F_+(\theta, \phi, \psi) &= \frac{1}{2}\left(1 + \cos^2\theta\right)\cos 2\phi \cos 2\psi - \cos\theta \sin 2\phi \sin 2\psi, \\ F_\times(\theta, \phi, \psi) &= \frac{1}{2}\left(1 + \cos^2\theta\right)\cos 2\phi \sin 2\psi + \cos\theta \sin 2\phi \cos 2\psi. \end{aligned} \tag{1.45}$$

In Chapters 2 and 3 sections of the results are obtained using this antenna pattern. For a more detailed discussion and derivation of the antenna patterns for L-shaped detectors please see [237].

Part of this thesis is also concerned with the third generation detector Einstein Telescope [224, 152, 27]. This detector is designed to use a triangle topology. The triangle will be equilateral and each length of the triangle will be used twice to form three Michelson interferometers. The detector response for a single interferometer in the array of three takes exactly the same form as Eq. (1.44) and the antenna pattern functions Eq. (1.45) however an L-shaped detector with the same arm length will be more sensitive by a factor of $2/\sqrt{3}$ [27, 237]. This antenna pattern is used indirectly to produce injections for the study presented in Chapter 4. Please see [27, 234] for full details of the antenna pattern for ET.

1.3.2 Sensitivity of gravitational wave interferometers

Sec. 1.3.1 presented an idealised version of detecting GWs with ground based detectors. However in general there are many other sources of unwanted noise that corrupt the signal from the large Michelson interferometers. A non-exhaustive list of sources of noise includes seismic noise from ground vibrations that can be generated from objects like cars driving around detectors, thermal noise from heat in the mirrors and suspension systems, quantum noise sources of shot noise and radiation pressure, and gravity gradient noise from small changes in the gravitational field due to objects moving around the detectors [3]. In the absence of gravitational waves the output $d(t)$ will just be a time series of noise $n(t)$ which is the additive result of all the various sources of noise. In theory the noise is considered to be stationary and Gaussian. In this thesis there is no analysis of actual detector data and as such these assumptions can be satisfied. However in practice this is not true and great care is taken to characterize the non-stationary and non-gaussian nature of noise in GW detectors [6, 205, 25]. The noise can be represented by its *one-sided power spectral density* (PSD) which can be defined as the fourier transform of the ensemble average of the auto-correlation of the noise $R(\tau)$ [191]

$$\frac{1}{2}S_n(f) \equiv \begin{cases} \int_{-\infty}^{-\infty} R(\tau)e^{2\pi i f\tau}d\tau, & f \geqslant 0 \\ \infty, & f < 0 \end{cases} \tag{1.46}$$

$$R(\tau) \equiv \int_{-\infty}^{\infty} \overline{n(t+\tau)n(t)}\, dt. \tag{1.47}$$

In practice when working with actual data there is only one data time series and different methods have been developed to estimate the PSD, such as averaging methods [278, 2] and methods that fit models to numerical PSD instances [182].

For this thesis several different PSDs will be used to perform calculations for different detectors. Several PSDs are presented in Fig. 1.1 that show the evolution of the sensitivity of ground based GW detectors and the projected sensitivity of future detectors. This includes all PSDs that are used in this thesis. Some of these PSDs are analytical fits to legacy data [235, 33] while more recent PSD estimates are calculated using the GWINC model [178] based on recent experimental measurements [61] that includes estimates for the

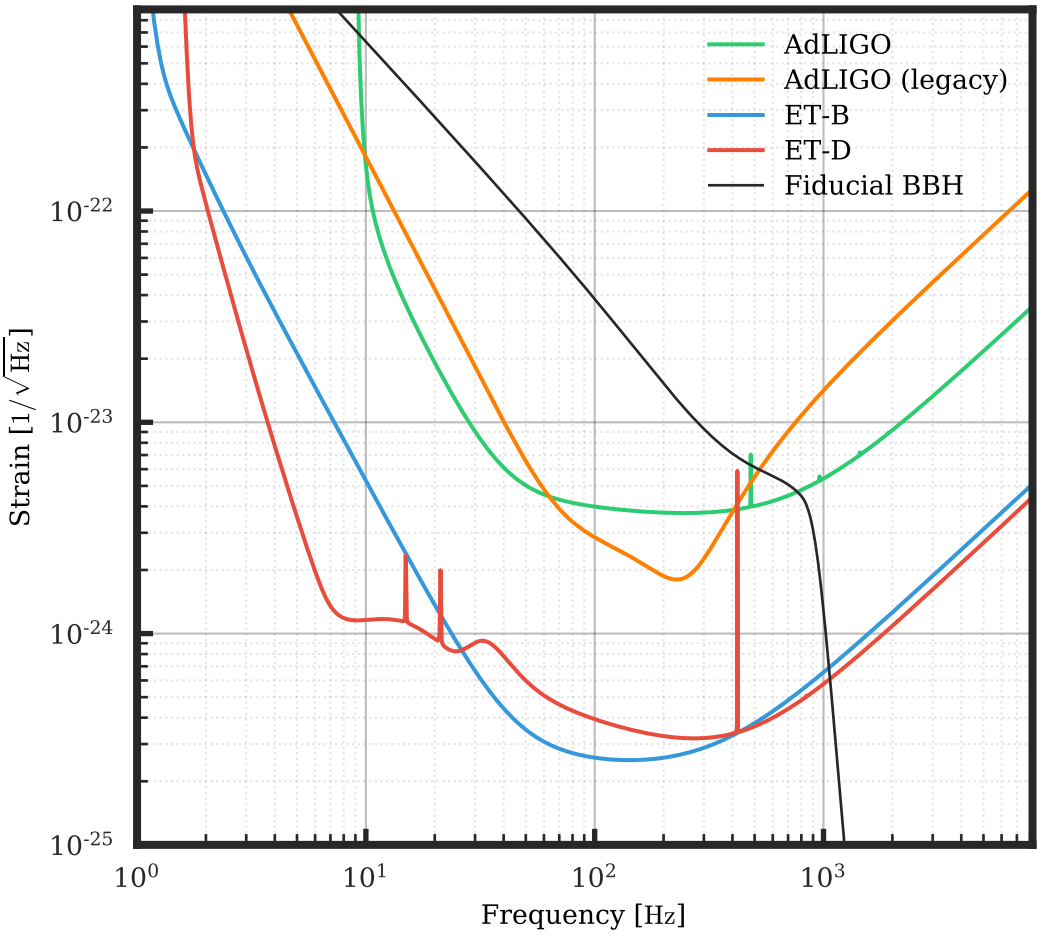

Figure 1.1: Comparison of sensitivity curves for multiple generations of detectors. The green line is the Advanced LIGO, Zero Det, High Power simulated sensitivity curve [249], the orange line is a legacy projection of the Advanced LIGO sensitivity curve [235, 33], the blue and red lines are the ET-B and ET-D sensitivity options for Einstein Telescope [151, 152] and the thin grey line is the amplitude of the strain for a fiducial BBH system at a distance of $100\mathrm{Mpc}$ where each BH has mass $10M_{\odot}$.

noise sources previously discussed.

The Advanced LIGO, Zero Det, High Power simulated sensitivity curve [249] is used for analysis in Chapters 2 and 3. Advanced LIGO makes use of a signal recycling mirror (SRM) between the main interferometer arms and the output photodetector. This component can be calibrated or *detuned* to change the frequency at which the detector is most sensitive. *Zero Det* means that the SRM is not detuned and as such the peak sensitivity of the detector is not changed by the SRM. The ET-D sensitivity option for Einstein Telescope [152] is used in Chapter 4. The older ET-B sensitivity option was based on a single interferometer detector with broadband response like Advanced LIGO. The more recent and improved ET-D sensitivity option incorporates new and updated noise sources and is based on a *xylophone-design* where the detector is composed of two interferometers, one sensitive to low-frequency and one sensitive to high-frequency.

Throughout this thesis, unless otherwise stated, calculations will be performed in geometric units where $G = c = 1$. However, momentarily these can be reintroduced to the EFE to perform an order of magnitude analysis of the GWs emitted by a conservative Newtonian system Eq. (1.40). The GW frequency and spatial amplitude of such a system become,

$$f \equiv \frac{\Omega}{2\pi} = \sqrt{\frac{GM}{8\pi^2 R^3}}, \qquad |h| = \frac{8}{r}\frac{G}{c^4} M\Omega^2 R^2 = \frac{2G^2M^2}{rc^4R}. \tag{1.48}$$

For a fiducial system of two objects each of mass $M = 10M_\odot \sim 10^{31}\mathrm{kg}$ and orbiting with a radius 10 times their Schwarzschild radius $R = 10r_s \sim 10^5\mathrm{m}$, and observed at a distance of $r = 100\mathrm{Mpc} \sim 10^{24}\mathrm{m}$, the GW frequency and strain will be,

$$f = \sqrt{\frac{10^{-11}\cdot 10^{31}}{8\pi^2 10^{15}}} \sim 10^2\mathrm{s}^{-1}, \qquad |h| = \frac{2\cdot 10^{-22}\cdot 10^{62}}{10^{24}\cdot 10^{32}\cdot 10^5} \sim 10^{-21}. \tag{1.49}$$

These order of magnitude estimates suggest that ground based gravitational wave detectors as described in this section should be able to detect GW from such systems. In particular binary systems that are comparable to stellar-mass. These types of systems will be explored next in Sec. 1.4.

1.4 Sources of gravitational waves

The results of Sec. 1.2 provided a mechanism by which GWs can be created. Sec. 1.3 established how GWs can be detected and importantly the range of frequencies over which GW can be detected with ground-based detectors. Motivated by these results it becomes clear that candidate sources of GWs that could be detectable on Earth are accelerating objects that are stellar mass in size, ranging from masses comparable to our own host star up to $\sim 100M_\odot$. There are a wide range of astrophysical objects that fulfil these criteria. For this thesis the focus will be on a subset of compact binary coalescence (CBC) type systems and their remnants. These sources will be described in detail in this section.

Before introducing these relevant sources, other important sources of GWs for current generation ground based detectors will be briefly summarized. GW *burst* events that emit detectable levels of GWs are expected to come from a wide range of phenomena including gravitational collapse of stellar cores leading to supernovae explosion, transient change in the rotational frequency of neutron stars known as pulsar glitches, and neutron stars collapsing into black holes. Some of these types of events have associated GW models while others do not. Currently no GWs from burst events have been detected [17, 21, 16]. *Continuous waves* (CW) are predicted to come from spinning neutron stars that have an asymmetry with respect to their rotational axis. These waves are expected to have approximately constant frequency but at a much lower amplitude than other sources of GWs. Searches for these types of events requires analysis of weeks worth of data, much longer than most other GW events that last seconds. Currently there is no evidence of continuous wave signals in data from current generation detectors [15]. Finally there is the *stochastic gravitational wave*

background (SGWB) which is the combined effect of many gravitational waves from low amplitude astrophysical sources such as very distant CBC events and cosmological sources like the early expansion of the universe. No evidence of the SGWB was found in current data [23].

1.4.1 Binary black hole systems

A binary black hole (BBH) system is composed of two black holes in a gravitationally bound quasi-circular orbit. Unless otherwise stated, for this thesis the secondary black hole (BH) with properties labelled with a 2 is the larger black hole to be consistent with the conventions of the BAM code, which will be discussed in Sec. 1.5. At any instance a BBH system can be fully described by the masses of the two black holes m_1 and m_2, their positions $\boldsymbol{c}_1$ and $\boldsymbol{c}_2$, linear momenta $\boldsymbol{p}_1$ and $\boldsymbol{p}_2$, and their dimensionful *spin angular momenta* $\boldsymbol{S}_1$ and $\boldsymbol{S}_2$. Dimensionless spin vectors $\boldsymbol{\chi}_i = \boldsymbol{S}_i/m_i^2$ are also often used.

An important conserved quantity in general relativity is the *total angular momentum* $\boldsymbol{J}$ which can be represented as the sum of *orbital angular momentum* $\boldsymbol{L}$ and spin angular momentum $\boldsymbol{S}_1$ and $\boldsymbol{S}_2$. For a given spacetime it is possible to calculate $\boldsymbol{J}$ [38, 66], however $\boldsymbol{S}_1$ and $\boldsymbol{S}_2$ cannot be unambiguously defined. Similarly $\boldsymbol{L}$ cannot be unambiguously defined, unlike its classical analogue, the *Newtonian orbital angular momentum* $\boldsymbol{L}_{\rm N}$ which is the sum of the cross product of the position and linear momenta. Even though $\boldsymbol{L}_{\rm N}$ originates in classical mechanics, as it defines the instantaneous orbital plane of a binary system it is still useful in general relativity and will be used throughout this thesis. One approximate method to calculate the spin angular momenta of the individual black holes is briefly summarised in Sec. 1.5.4, and as such provides an approximate method to define orbital angular momentum in general relativity.

For this thesis the focus is primarily on GWs emitted by CBC systems like this. A gravitational wave from a non-eccentric BBH system can be parameterized by eight *intrinsic parameters* $\boldsymbol{\theta}_{\rm in}$,

$$\boldsymbol{\theta}_{\rm in} = \begin{pmatrix} m_1 \\ m_2 \\ \boldsymbol{S}_1 \\ \boldsymbol{S}_2 \end{pmatrix} \begin{matrix} \text{Mass of primary object} \\ \text{Mass of secondary object} \\ \text{Dimensionful spin angular momentum of primary object} \\ \text{Dimensionful spin angular momentum of secondary object.} \end{matrix} \tag{1.50}$$

These are simply representations of the mass and angular momentum parameters of the Kerr metric for each black hole. All CBC systems also have to be parameterized by 8 *extrinsic parameters* $\boldsymbol{\theta}_{\rm ex}$ that describe the relative location and orientation of the system with respect to an observer, and the moment in time that the spins of each component black hole are

specified,

$$\boldsymbol{\theta}_{\rm ex} = \begin{pmatrix} d_L & \text{Luminosity distance} \\ \alpha & \text{Right ascension} \\ \delta & \text{Declination} \\ \iota & \text{Inclination angle} \\ \psi & \text{Polarization angle} \\ t_0 & \text{Reference time} \\ \phi_0 & \text{Reference orbital phase} \\ \omega_0 & \text{Reference orbital frequency} \end{pmatrix} \tag{1.51}$$

Some of these extrinsic parameters have already appeared in the detector antenna patterns described by Eq. (1.45). The parameterization $\boldsymbol{\theta} = \boldsymbol{\theta}_{\rm in} \cup \boldsymbol{\theta}_{\rm ex}$ is not unique, and different combinations of parameters are often used instead such as the mass ratio $q \equiv m_2/m_1$, chirp mass $\mathcal{M} \equiv (m_1 m_2)^{3/5}/(m_1+m_2)^{1/5}$, and time and phase of coalescence (t_c, ϕ_c).

A CBC system typically evolves through three stages as it emits gravitational waves. The *inspiral* stage occurs first, while the separation between the component bodies is large. The *merger* stage is a transition period when the two bodies plunge towards each other and merge. The final stage is *ringdown* where the non-axisymmetric body resulting from the merger transitions to equilibrium as it emits its final gravitational waves. For CBC systems that involve at least one BH, if the two objects merge then it is expected to result in a perturbed Kerr BH. The perturbed Kerr BH will emit a GW evolving as exponentially damped oscillations with characteristic dimensionless complex frequencies called *Quasi-Normal Mode* (QNM) frequencies that describe the central frequency of the oscillations and the rate at which the GWs decay. These GWs are typically decomposed into spheroidal harmonics [176]. The spheroidal harmonic functions of the spheroidal decomposition, together with the QNM frequencies, are collectively called the QNM solutions of Teukolsky's equations [263]. The QNM solutions are identified by three indices, l, m, and n. The indices l and m are equivalent to the indices of regular spherical harmonic functions, and n is the *overtone* index indicating the different resonant QNM frequencies.

There are lots of ways that BBH systems can be classified, such as systems where each component black hole has the same mass, or the component black holes have no spin. However two classes of BBH systems that have been very important for the first era of GW astronomy are *non-precessing* or *aligned-spin* BBH systems and *precessing* systems.

For a non-precessing systems the component spins $\boldsymbol{S}_i$ are both parallel to the orbital angular momentum $\boldsymbol{L}$, and as a result the Newtonian orbital angular momentum $\boldsymbol{L}_{\rm N}$. For such systems the direction of all angular momenta remain fixed and the component black holes orbit in a fixed plane. For precessing systems at least one of the component spins will point in a direction that is not parallel to the orbital angular momentum. The directions of $\boldsymbol{L}$, $\boldsymbol{L}_{\rm N}$ and $\boldsymbol{J}$ no longer remain fixed and $\boldsymbol{L}$ will precess around $\boldsymbol{J}$.

Modelling GWs from either of these classes of systems is a challenge. Several combina-

tions of parameters have been discovered that capture the dominant characteristics of GWs emitted by these systems. For example the *effective spin* parameter [36],

$$\chi_{\rm eff} \equiv \frac{m_1(\boldsymbol{\chi}_1 \cdot \hat{\boldsymbol{L}}) + m_2(\boldsymbol{\chi}_2 \cdot \hat{\boldsymbol{L}})}{m_1 + m_2}, \tag{1.52}$$

is closely related to the leading order spin effects in the phase of a binary system in post-Newtonian theory [102, 220], which will briefly be discussed in Sec. 1.6. There is also a dimensionless *precession spin* parameter [242] that is a combination of in-plane spin components, and has been used in models for precessing systems,

$$\chi_p \equiv \frac{\max(A_1 S_{1\perp}, A_2 S_{2\perp})}{2A_2 m_2^2}, \tag{1.53}$$

$$\boldsymbol{S}_{i\perp} \equiv \boldsymbol{S}_i - (\boldsymbol{S}_i \cdot \hat{\boldsymbol{L}})\hat{\boldsymbol{L}}, \tag{1.54}$$

$$A_1 \equiv 2 + \frac{3m_2}{2m_1}, \quad A_2 \equiv 2 + \frac{3m_1}{2m_2}. \tag{1.55}$$

Identifying and using these combinations of parameters has enabled the development of approximate but accurate GW models for CBC systems and will be explored further in Sec. 1.6.

1.4.2 Neutron star black hole systems

A neutron star black hole binary (NSBH) system is composed of one black hole and one neutron star (NS) that are in a gravitationally bound orbit. These types of CBC system are described by all the same physical attributes as a BBH system and parameterization of GWs emitted by these systems also include all of the intrinsic and extrinsic parameters for BBH as defined in Eqs. (1.50) and (1.51). However there is an added complexity from the neutron star, where the matter of a neutron star is distributed over a non-singular point. Neutron stars typically have a radius of $\sim 10\mathrm{km}$.

The matter distribution within a neutron star can be approximated by the spherically symmetric *Tolman-Oppenheimer-Volkoff* equations [267, 268, 210]. These equations depend on an equation of state (EoS) that is a relationship between the pressure and density within the NS. For a particular EoS and density ρ_c given at the center of a NS, the Tolman-Oppenheimer-Volkoff equations can be integrated out to a radius R where the pressure drops to zero, which bounds matter with total mass M . The *compactness* C of a NS is defined as the ratio of its radius R and mass M.

As a result of the matter distribution of neutron star, they experience *tidal forces* which can deform the neutron star and can lead to tidal disruption events where the tidal forces are so great that the neutron star is pulled apart. The amount that a neutron star is able to deform due to an external gravitational field is quantified by a dimensionless *tidal deformability*

parameter,

$$\Lambda = \frac{2}{3}\frac{k_2}{C^5}, \tag{1.56}$$

where k_2 is the tidal Love number [188, 126, 153].

The set of parameters $\boldsymbol{\theta} = \boldsymbol{\theta}_{\rm in} \cup \boldsymbol{\theta}_{\rm ex} \cup \{\Lambda\}$ are then sufficient to parameterize GW emitted by NSBH systems. The phenomenology of NSBH will be explored in more detail in Chapter 2 where a new model for GW from NSBH systems will be presented.

1.5 Simulating gravitational waves

There are very few exact solutions to the EFE Eq. (1.10) and no exact solutions exist for BBH systems. The only way to explore more general solutions of the ten non-linear, coupled, partial differential equations is to use numerical methods and high-performance computing which is the objective of the field of *numerical relativity*. Because measurable GWs are only emitted by relativistic systems numerical relativity has been a crucial component of simulating GW sources that are theoretically measurable by current ground based detectors. In particular simulating the coalescence of two inspiraling black holes was a key challenge for early numerical relativity research and is still an active area of development today.

During the 20th century simulations of BBH systems using numerical relativity were seen as the only way to get accurate information about the late-time evolution of such systems and ultimately the only way to produce gravitational waves from such systems. Since this time, in parallel to the developments in NR, progress has also been made in post-Newtonian and effective-one-body approximations. The developments in these two approximations has resulted in GW waveforms that are very accurate up until very late times in BBH evolution and some of this work will be summarized in Sec. 1.6. However numerical relativity is still the only way to evolve a BBH system through its merger to form a single black hole experiencing ringdown, and as such the only way to simulate accurate GWs of such systems at the late-inspiral and merger stages of their evolution.

The earliest attempt to simulate two interacting bodies using numerical relativity in the framework of *geometrodynamics* was by Hahn and Lindquist in 1964 [138]. However it wasn't until the next decade when head-on collisions of two black hole resulting in merger were simulated [252, 119]. These frameworks were all restricted to simulating systems with various levels of symmetry. Various efforts to simulate the inspiral and merger of BBH systems were carried out at the end of the 20th century [95]. However it was not until 2005 when Frans Pretorius produced the first non-axisymmetric BBH simulation through merger and ringdown [223]. While the simulation was short compared to today's standards, with the binary system performing only a single orbit before merger, it marked a major turning point for numerical relativity.

Since then many independent numerical relativity codes have been able to simulate BBH systems for many orbits and add support for more complex configurations such as highly

spinning black holes. The data products from numerical relativity have been crucial for the field of gravitational waves, including as input to developing approximate GW models, to calculate remnant properties of binary mergers, and used directly for GW injection studies. The numerical relativity code BAM [83, 84, 157] was used to produce NR simulations of BBH systems for this thesis. For the remainder of this section the numerical methods used by BAM to simulate compact binary coalescences of BBH systems will be described, starting with the reformulation of the EFE in a form that is amenable to computation, how the apparent horizons of the black holes are tracked, and finally how GWs are extracted from these simulations. For a more detailed description of the methods used by BAM please see [83, 84, 157].

1.5.1 Initial value problem

Many methods have been developed to solve the EFE numerically with the earliest methods solving for the full four-dimension metric $g_{\mu\nu}$ [138]. The class of methods that has been most widely used for simulating binary systems are the 3+1 decompositions of the EFE. Before considering the 3+1 reformulation of the EFE the metric first needs to be decomposed. This can be achieved by considering a *foliation* of the spacetime.

To define a foliation, consider a spacetime $(M, g_{\mu\nu})$, and a smooth scalar field $t(x^\mu)$ defined on the manifold M. Three-dimensional submanifolds Σ_s are defined such that for all $s \in \mathbb{R}$

$$\Sigma_s = \{m \in M | t(m) = s\}. \tag{1.57}$$

If everywhere the scalar field t has a non-zero gradient then Σ_{s_1} will not intersect with Σ_{s_2} for $s_1 \neq s_2$. The set of non-intersecting submanifolds

$$S = \{\Sigma_s | \forall s \in \mathbb{R}\}, \tag{1.58}$$

then represents a *foliation* of the spacetime, and each element of S is called a *slice* of the foliation [135].

That a foliation exists for a given spacetime is not guaranteed. Moreover it is required that the slices are spacelike for a 3+1 decomposition. For this thesis the spacetimes that are simulated with `BAM` can always be foliated by spacelike submanifolds. In general spacetimes simulated with a 3+1 decomposition will be of a type known as *globally hyperbolic* which amongst their properties do admit spacelike foliations. Intuitively the different slices of a spacelike foliation represent different time steps of evolving a spatial system.

With a foliated spacetime in hand an aim of the 3+1 decomposition is to consider how a three-dimensional purely spatial metric γ_{ij} on the slices of the foliations evolves. Note that Roman indices i, j as used to distinguish the spatial coordinates from spacetime coordinates. A simplified geometric argument can be made to relate γ_{ij} to the four-dimensional metric $g_{\mu\nu}$ which is visualized in Fig. 1.2.

Consider a slice Σ_{t_1} and a slice an infinitesimal time later Σ_{t_1+dt}. The proper time

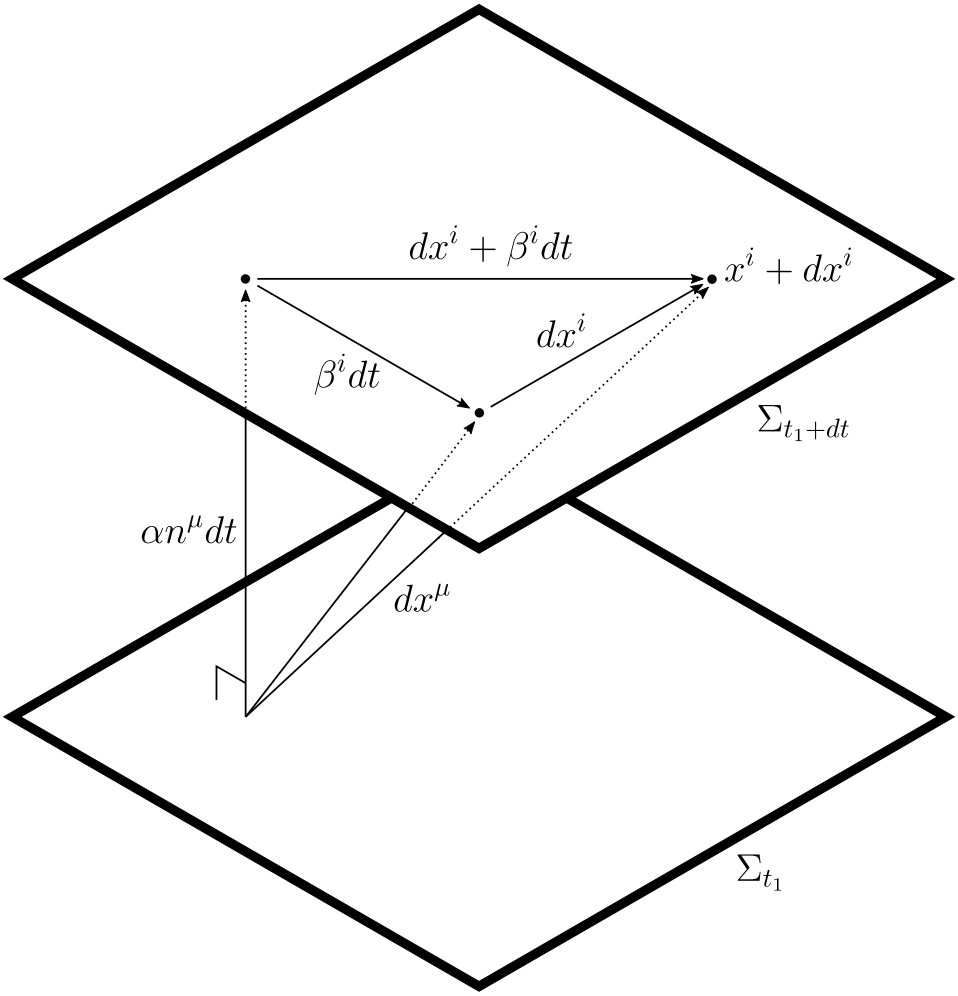

Figure 1.2: Geometric visualization of the four-dimensional line element ds decomposed into it's temporal and spatial components as is done for a 3+1 decomposition. n^μ is the normal vector to a slice Σ_{t_1}. Given a scalar field t and lapse α, it can be shown that $n^\mu = -\alpha \nabla^\mu t$.

for a *normal observer* following a normal to Σ_{t_1} such that there is no spatial displacement can be written as $d\tau = \alpha(x^\mu)dt$ where $\alpha(x^\mu)$ is introduced to relate the coordinate time to proper time. This function is called the *lapse*. In general a normal observer will not follow lines of constant spatial coordinates. For an observer with constant spatial coordinates x^μ the position of a normal observer starting at the same spatial coordinates can be written as $x^\mu - \beta^i(x^\mu)dt$ where $\beta^i(x^\mu)$ is introduced to describe the relative velocity of normal observers and constant spatial observers. This vector is called the *shift*. An infinitesimal displacement dx^μ can then be written in terms of the purely spatial and temporal parts as $dx^\mu = (\alpha dt, dx^i + \beta^i dt)$. The four-dimensional line element can then be written down as

$$ds^2 = -\alpha^2 dt^2 + \gamma_{ij}(dx^i + \beta^i dt)(dx^j + \beta^j dt), \tag{1.59}$$

where the first additive expression is the temporal displacement perpendicular to the slice

and the second expression is the spatial line element within the slice. The four functions (α, β^i) represent the gauge freedom of GR. For a more rigorous derivation of this 3+1 metric decomposition please see [38, 65, 66].

The EFE are second-order differential equations in the metric $g_{\mu\nu}$ or equivalently in the 3+1 decomposition second-order in γ_{ij}. However it is more convenient to recast these as a set of first-order equations. To facilitate this the *extrinsic curvature* K_{ij} can be introduced in the form given by [38]

$$K_{ij} = -\frac{1}{2\alpha}\left(\frac{\partial \gamma_{ij}}{\partial t} - \gamma_i{}^k \nabla_k \beta_j - \gamma_j{}^k \nabla_k \beta_i\right), \tag{1.60}$$

The EFE can now be theoretically written as a set of first-order differential equations in (γ_{ij}, K_{ij}).

With the metric decomposed and all the necessary definitions established it is now possible to discuss the candidate 3+1 reformulations of the EFE. The first widely used 3+1 decomposition of the EFE was developed by Arnowitt, Deser and Misner [53] and subsequently refactored by York [281] that are now referred to as the *ADM equations*. These equations consists of two *constraint* equations, the *momentum constraint* and *Hamiltonian constraint* equations, and evolution equations for (γ_{ij}, K_{ij}). While an important theoretical stepping stone, it was found that these equations are unstable for evolving systems relevant for GW research and code implementations typically crash.

A modification to the standard ADM equations was developed by Shibata and Nakamura [247] and Baumgarte and Shapiro [64] which are commonly referred to as the *BSSN equations*. In this modification the standard ADM variables (γ_{ij}, K_{ij}) are replaced by the *BSSN variables* with the introduction of a *conformal factor* $\psi(x^\mu)$,

$$\phi \equiv \ln \psi, \tag{1.61}$$

$$K \equiv \gamma^{ij} K_{ij}, \tag{1.62}$$

$$\tilde{\gamma}_{ij} \equiv \psi^{-4} \gamma_{ij}, \tag{1.63}$$

$$\tilde{A}_{ij} \equiv \psi^{-4} A_{ij}, \tag{1.64}$$

$$\tilde{\Gamma}^i \equiv \tilde{\gamma}^{jk} \Gamma^i_{jk} = -\partial_j \tilde{\gamma}^{ij}, \tag{1.65}$$

where the trace-free part of the extrinsic curvature is defined as $A_{ij} = K_{ij} - \gamma_{ij} K/2$. Evolution equations for BSSN variables $(\phi, K, \tilde{\gamma}_{ij}, \tilde{\gamma}_{ij}, \tilde{A}_{ij}, \tilde{\Gamma}^i)$ are derived from the The ADM equations to form the BSSN system where unlike the ADM variables the BSSN variables are not independent. The ADM and BSSN equations were directly compared in many studies [64, 63, 40, 39, 177, 42] with different choices of the gauge functions (α, β^i) and initial conditions. It was consistently demonstrated that this modification leads to long-term stable evolutions in contrast to the ADM system that typically crashed after a very short evolution time.

While the explicit form of the BSSN equations introduce several other non-independent

variables with an overspecified set of evolution equations in effect both the ADM and BSSN reformulations provide the necessary equations to evolve the spatial tensors (γ_{ij}, K_{ij}). `BAM` uses the BSSN system. For a concise summary of the ADM and BSSN systems please see the comparison study [64].

To complete the definition of the initial value problem initial data also needs to be defined on an initial slice. The strategy used by BAM is to apply the conformal transverse-traceless (CTT) approach [281] where *Conformal flatness* is assumed for the metric $\tilde{\gamma}_{ij} = \eta_{ij}$ and *maximimal slicing* such that $K = 0$. The momentum constrain can then be solved for the trace-free part of the extrinsic curvature A_{ij} as *Bowen-York data* [77]. The Hamiltonian constraint can then be reduced to an elliptical equation in the conformal factor ψ. This can be solved by *puncture data* [79] which is an extension of the *Brill-Lindquist data* [81] for black holes with arbitrary momenta and spin. Finally the gauge functions for BAM are chosen to be $(\alpha, \beta_i) = (\psi^{-2}, 0)$ [84]. Initial values for all the BSSN variables can now be defined and this completes the specification of the initial value problem.

1.5.2 Evolving moving punctures with adaptive mesh refinement

To evolve the initial data BAM uses the χ-method of the moving-puncture approach [88, 142]. The puncture solution for the conformal factor is not a real analytic function as it has singularities at the locations of the black holes. To address this a new conformal factor $\chi \equiv \psi^{-4}$ is defined [88] and an evolution equation for χ replaces the evolution equation for ϕ. In addition the gauge functions are determined by the *1+log* slicing condition [74] and the Gamma-driver conditions [43].

The system is evolved numerically using the *method of lines* [238, 239] with a fourth order finite-difference Runge-Kutta scheme. Instead of a uniform cartesian grid covering the entire spatial computational domain, a Berger-Oliger adaptive mesh refinement method is used [67]. This consists of a hierarchy of $L+1$ levels of nested three dimensional Cartesian grids with uniform spacing on each level given by $h_n \forall n \in \{0...L\}$,

$$h_n = \frac{h_0}{2^n}. \tag{1.66}$$

As these nested grids are finite in size they are also referred to as *boxes*. On the finest level L the grid is centred on the motion of the smallest black hole. At some chosen level M, a second grid is introduced such that each black hole has one grid that follows its motion. Note that it is possible to require $L = M$. When a level N is reached such that the two grids on level $N+1$ tracking the motion of the black holes would overlap, a single grid is used with grid spacing h_N that is large enough to cover the nested grids following each black hole. All levels $n \leqslant N$ remained fixed and centred on the origin of the coordinate system.

The grid on any given level is composed of N_n^3 grid points, N_n grid points in each dimension. The number of grid points N_n on each level can be freely chosen however they should be chosen such that they can always contain any nested grids. For a BAM simulation, the grid spacing on the finest level h_L is specified along with the number of grid points on

the finest level N_L. For a typically exploratory BAM simulation, $N_L = 80$ and h_L is chosen to satisfy some auxiliary requirements. Examples of such requirements will be presented in Chapter 3. *Higher resolutions* runs are then performed once a simulation configuration has been found. In higher resolution runs the number of grid points is increased, for example $N_L \in \{96, 120, 144\}$, and the grid spacing is decreased such that $N_L \times h_L$ is left unchanged. The number of grid points for all *moving box* levels $n \in \{N+1, ..., L\}$ is the same. As such it is typical to refer to a run simply by its N_L number, for example if $N_L = 96$ then this would be called a 96-point run. h_L is also required to fully qualify the resolution of a simulation and may be denoted as d.

1.5.3 Tracking properties of apparent horizons

Gravitational waves are not the only useful properties that can be gained from an NR simulation. The physical quantities of mass and spin of each of the black holes are also important. In order to extract these properties for each component black hole of a BBH system, these need to be defined as *quasi-local* properties that only depend of a finite spacetime region around each black hole [260].

Quasi-local definitions of the mass and spin can given by integrals over the *apparent horizons* surrounding each black hole. Given a slice Σ and a closed two-dimension sub-manifold S of Σ with outward facing normal s^i, S is an apparent horizon if the *expansion*,

$$H(x^k) \equiv \nabla_i s(x^k)^i + K_{ij}(x^k) s(x^k)^i s(x^k)^j - K(x^k), \tag{1.67}$$

is zero for all $x^i \in S$ [41, 38]. Quasi-local definitions of the apparent horizon masses $M_{\rm AH}$ and dimensionful spin vectors $\mathbf{S}_{\rm AH}$ can then be defined for each black hole in a binary system as given by [108, 89]. These apparent horizon properties will be used in Chapter 3 when analysing a new set of NR simulations.

BAM uses the *fast flow algorithm* to find apparent horizons on each slice as the initial data is evolved [41, 136]. A candidate apparent horizon solution $h(\theta, \phi)$ is decomposed into spherical harmonics. The expansion coefficients are then heuristically chosen initially to describe a sphere embedded in the current slice that should surround the apparent horizon that is being searched for. An iteration scheme is then applied to the expansion coefficients until they have converged to the desired tolerance.

1.5.4 Extracting gravitational waves

For BAM GW information is calculated using the *Newman-Penrose* (NP) formalism [202, 218]. Within this framework a set of scalar fields can be defined called the *Weyl scalars*. The complex valued Weyl scalar Ψ_4 is of particular relevance because it is related to the

complex representation of GW strain $h(t)$ by two time derivatives,

$$\Psi_4(t) = \frac{\partial h(t)}{\partial t}, \tag{1.68}$$

$$h(t) \equiv h_+(t) - ih_\times(t). \tag{1.69}$$

Ψ_4 can be conveniently constructed just from the ADM variables along with the choice of null-tetrad required to engage with the NP formalism.

The relationship between Ψ_4 and GW strain is only strictly valid in the infinite radius limit. However BAM does not perform simulations on an infinite grid. Instead Ψ_4 is calculated on a set of concentric spherical shells at user defined radii. For the simulations produced for this thesis these radii are at $\{50, 60, 70, 80, 90\}M$ which are typical values for other BAM simulations. In theory the information of Ψ_4 on each shell can be used to extrapolate Ψ_4 to radial infinity. However extrapolation has its own challenges. Instead it is typical for Ψ_4 to be used from the largest extraction radii of finest grid level that GWs are extracted on. This is typically the first fixed boxed grid level M.

Converting Ψ_4 to strain is not as trivial as performing two time integrals as Eq. (1.68) would suggest. A naive application of two time integrals will typically result in non-linear drifts in the result. In part this is as a result of the finite extraction radius, however it has also been attributed to the unavoidable discretization schemes used to simulate the spacetime. An empirical solution to this problem is the method of *fixed-frequency integration* [231]. In this method the time integrals are performed in the frequency domain,

$$\tilde{h}(f) = \begin{cases} \dfrac{\tilde{\Psi}_4(f)}{(2\pi f_0)^2}, & f \leqslant f_0 \\ \dfrac{\tilde{\Psi}_4(f)}{(2\pi f)^2}. & f > f_0 \end{cases} \tag{1.70}$$

In the fixed-frequency integration method the frequency parameter f_0 is chosen to be the lowest physical GW frequency for the system.

1.6 Modelling gravitational waves

Simulating GWs with NR is the most accurate method to produce GWs for BBH systems. However it is slow often taking months to simulate a single system configuration. To make most GW analysis practicable it is necessary to have approximate GW models that can be evaluated in much less time. In this section some of the methods of modelling GWs will be summarized. Both NR and GW modelling are crucial to GW research. This thesis will demonstrate that it is the syntheses of both of these approaches to generating artificial GWs that enables fast and accurate detection and parameter estimation of GWs.

In the Newman–Penrose formalism briefly discussed in the previous Sec. 1.5.4 the Weyl scalar Ψ_4 was presented along side its important complex valued representation of the GW

strain field as two time derivatives of the two GW strain polarizations. Similar to other areas of physics like electromagnetism, this field can be decomposed using a multipole expansion. It has been shown that appropriate expansion functions are the *spin weight -2 spherical harmonics* [202]. Suppressing the contextually irrelevant GW parameters and the full expansion can be written as [265, 232],

$$h(t, r, \theta, \phi) = h_+(t, r, \theta, \phi) - ih_\times(t, r, \theta, \phi) \tag{1.71}$$

$$= \frac{M}{r} \sum_{\ell=2}^{\infty} \sum_{m=-\ell}^{\ell} h_{\ell m}(t - r) \, {}^{-2}Y_{\ell m}(\theta, \phi). \tag{1.72}$$

The objective of GW modelling then reduces to the task of approximating the complex valued *expansion coefficients* $h_{\ell m}$. These coefficients are called *multipole moments*, however they are very commonly referred to as *modes* and less commonly just *moments*. All names will be used interchangeably throughout this thesis. The complex modes are typically further decomposed into amplitude and phase parts,

$$h_{\ell m}(t, \boldsymbol{\theta}) = A_{\ell m}(t, \boldsymbol{\theta}) e^{-i\phi_{\ell m}(t, \boldsymbol{\theta})}. \tag{1.73}$$

For non-precessing CBC systems the $(\ell, |m|) = (2, 2)$ mode contains a large amount of the gravitationally radiated power and as such had been the focus of much of the GW modelling community. While work still continues on improving the accuracy of models of the (2,2) mode, several models have also now been produced that capture the *higher mode* $\ell = |m|$ and *sub-dominant mode* $\ell \neq |m|$ content of GWs, as will be shown throughout the rest of this section.

1.6.1 Post-Newtonian methods

Beyond Einstein's quadrupole formula that was presented in Sec. 1.2, the collection of *post-Newtonian* (PN) methods were the first approximations that provided a more detailed description of the dynamics of multiple bodies in GR and the GW they emit. These methods assume that the motion of the bodies being modelled are slow with respect to the speed of light, and are perturbative expansions in the small parameter v/c. These methods are used to address three key challenges, the conservative dynamics of multiple interacting bodies that include the evolution of properties like spin angular momentum, the radiation-reaction part of the dynamics that describe the effect of gravitational radiation emitted by these multi-body systems on the dynamics of these systems, and expression for the GW strain emitted by these systems. With the direct association of the orbital phase with the GW phase this amounts to PN expressions for the GW amplitude.

Expressions for the various properties that post-Newtonian theory has been applied to have been calculated to different perturbative orders. PN expressions are usually expressed as having a *PN order* which is half the maximum order of the perturbation parameter v/c. However, there are different but equally valid ways of performing PN expansions up to a

given order. Additionally because PN expansions are asymptotic expansions, increased PN order does not guarantee a better approximation. For a complete review of the current status of PN theory and current state of the art PN orders please see the Living Review article by Luc Blanchet [69].

The different strategies for PN expansions gives rise to multiple PN approximants for GWs. A summary of these can be found in the comparison study by Buonanno et al. [86]. The particular PN approximants that are used in this thesis are the TaylorT2 amplitude model up to 3PN order [69] (now known up to 3.5PN order [122]) that incorporates spin-orbit corrections up to 1.5PN order and quadratic spin corrections up to 2PN order [54], and the TaylorF2 phase model that incorporates spin-independent corrections up to 3.5PN order [86, 69], linear spin-orbit corrections up to 3.5PN order [73] and quadratic spin corrections up to 2PN order [219, 54, 198].

1.6.2 Effective-one-body methods

As you get closer to merger in a CBC system the slow motion, weak field approximations used in the perturbative expansion of PN methods break down and the results are no longer accurate. The *effective-one-body* (EOB) methods were created to address this issue, and to enable construction of complete waveforms all the way through merger also known as inspiral-merger-ringdown (IMR) models that can accurately generate waveforms through the entire life of a CBC system and not just the inspiral stage.

The EOB method is based on high PN order expressions, and as such can be divided into the same three classes as PN theory, methods for conservative dynamics, radiation-reaction, and expressions for gravitational waveforms. The expressions for the PN conservative dynamics that describe two massive objects are resummed to describe the dynamics of a test particle in a deformed Kerr metric. The radiation-reaction expressions are often resummed as Padé approximants. The GW strain expressions are refactored and a new resummation procedure was developed.

To be able to create an accurate model past merger, the ringdown stage was modelled by taking results from BH perturbation theory briefly described in Sec. 1.4.1 to produce waveforms that model a perturbed Kerr BH. These are then attached to the inspiral-merger waveform with a Heaviside step function. Even the most accurate EOB models still break down at some point and lose accuracy to NR. To solve this issue as the EOB methods have developed, expressions with free coefficients have been incorporated which are then calibrated to NR.

Results of standard EOB models are time domain waveforms where as GW data analysis is typically carried out in the frequency domain. To evaluate EOB waveforms requires the evolution of the dynamics to be computed unlike the PN waveforms which can be evaluated pointwise at a specific GW frequency. Both of these features can add significant computational cost to model evaluation. To address this issue the *reduced order models* (ROM) method [226] was developed. Based on a singular value decomposition of fine

sampling of a model evaluation across it's parameter space, a ROM can create fast frequency domain implementations of time domain models.

The state of the art EOB models that have been used for the first and second observing runs of the Advanced LIGO and Advanced VIRGO detectors are a ROM of the aligned spin model `SEOBNRv4` [71] and the precessing model `SEOBNRv3` [211] .

1.6.3 Phenomenological models

The PN and EOB methods start from the basic physics of GR, construct approximations to system dynamics and eventually end up producing waveforms. The *phenomenological* models remove the intermediate steps of this process and instead directly model waveforms with rational and non-linear functions over physical parameters such as mass and spin. In the original phenomenological approach [34] an input data was constructed from NR waveforms hybridized (see Sec. 1.6.4) with PN approximants and then fourier transformed. These input waveforms were constructed across a range of $q \in [1, 4]$ non-spinning parameters. The amplitude and phase of this data set were then fit using a multi-level approach. On the first level each waveform was fit with a ansatz that was piecewise in frequency. Then the fitted coefficients of this ansatz for each waveform in the input data set formed a new data set. On the second level this new data set was fitted with a linear polynomial. The second level fit is combined with the first level ansatz to produce the final model.

Since the introduction of the first phenomenological model many new models have been developed that incorporate higher mode content and can accurately model precessing GWs. However the multi-level process has remained mostly unchanged, with significant improvements being made through the development of better ansatz and combining the piecewise parts of the different frequency bands. Collectively these are often call *Phenom* models.

The Phenom models are frequency domain models that can be evaluated pointwise, and they are simple non-linear functions, which means they are fast to evaluate. This makes them ideal for GW data analysis. However unlike the PN and EOB approaches to the inspiral, these models require input GW data which is why accurate NR has been crucial to the development of the Phenom family of models. The current state of the art Phenom model is `PhenomPv3HM` [165] which is a precessing model that includes higher order modes and sub-dominant modes.

1.6.4 Hybridization

An important approach to constructing complete IMR waveforms is *hybridization*. PN and EOB waveforms (with and without calibration to NR) can provide inspiral waveforms up to sufficiently late times before merger. NR can supply waveforms sufficiently early in time before merger but computational costs prohibit simulations from very early times that are trivial for PN and EOB models. Waveforms generated using both PN or EOB and NR can be fused together to form a complete *hybrid waveform*.

In this thesis hybrid waveforms are used in the analysis of PhenomNSBH in Sec. 2 and to predict NR accuracy requirements for third generation detectors in Sec. 4. The definition for hybrid waveforms used in this thesis is given below, which follows the procedure described in [87] for single mode hybridization, and uses the piecewise bounds as defined by [34, 35, 207].

A hybrid waveform $h_{\rm hy}(t)$ can be defined by piecewise construction from component waveforms $h_{\rm ins}$ and $h_{\rm NR}$. These two components are an inspiral waveform, typically a PN or EOB approximant, and NR waveform. Choose a region $t \in [t_0, t_1]$ with respect to the time range of the NR waveform, and define the $h_{\rm hy}(t)$ as,

$$h_{\rm hy} \equiv \begin{cases} e^{i\Delta\phi} h_{\rm ins}(t+\Delta t), & t < t_0 \\ w^{-}_{t_0,t_1}(t) e^{i\Delta\phi} h_{\rm ins}(t+\Delta t) + w^{+}_{t_0,t_1}(t) h_{\rm NR}(t), & t_0 < t < t_1 \\ h_{\rm NR}(t). & t_1 < t \end{cases} \tag{1.74}$$

The window functions $w^{\pm}_{t_0,t_1}(t)$ used for this thesis are the Planck taper functions [194],

$$w^{+}_{t_0,t_1}(t) \equiv \begin{cases} 0, & t < t_0 \\ \dfrac{1}{\exp\left(\dfrac{t_1-t_0}{t-t_0} + \dfrac{t_1-t_0}{t-t_1}\right)+1}, & t_0 < t < t_1 \\ 1. & t_1 < t \end{cases} \tag{1.75}$$

$$w^{-}_{t_0,t_1}(t) \equiv 1 - w^{+}_{t_0,t_1}(t) \tag{1.76}$$

The time shift Δt is the parameter that minimizes the integral of the difference of the GW frequency between each component over the interval $t \in [t_0, t_1]$,

$$\int_{t_0}^{t_1} \left(\omega_{\rm NR}(t) - \omega_{\rm ins}(t+\Delta t)\right)^2 dt, \tag{1.77}$$

and the phase shift $\Delta\phi$ is the parameter that minimizes the integral of the difference of the GW phase between each component over the same interval with the time shift applied,

$$\int_{t_0}^{t_1} \left(\phi_{\rm NR}(t) - \phi_{\rm ins}(t+\Delta t) + \Delta\phi\right)^2 dt. \tag{1.78}$$

The times t_0 and t_1 can be chosen freely from the time interval where the two component waveforms overlap. They will typically be chosen by considering properties of the component waveforms. For example t_0 might be chosen a fixed number of GW cycles after the start of $h_{\rm NR}$ and t_1 a fixed number of GW cycles after t_0.

1.7 Analysing gravitational waves

Sec. 1.3 demonstrated that it is theoretically possible to observe a GW signal but that because of the many other sources of noise in candidate detectors the observed signal data $d(t)$ will be a combination of a GW signals antenna response $h(t)$ and detector noise $n(t)$

$$d(t) = h(t) + n(t). \tag{1.79}$$

Processing of data $d(t)$ naturally motivates two questions. Is there a GW signal contained in the data? What are the most likely parameters of a candidate GW signal in the data? There can be lot of overlap between these two questions, but in general knowing that there is a GW signal in the data doesn't have to mean you know the most likely parameters, and similarly knowing the most likely parameters does not guarantee that there is an actual GW signal in the data.

The first question is the concern of GW search pipelines [259, 270]. This thesis is not about GW searches, however some of the theory used by search pipelines is used in modelling gravitational waves. As such this will be briefly discussed in Sec. 1.7.1 to introduce the theory of *matched filtering*. The second question is the concern of GW parameter estimation [275]. Parameter estimation methods are used in Sec. 4 and so the theory of *Bayesian inference* will be introduced in Sec. 1.7.2.

1.7.1 Matched filtering

Matched filtering [148] is an efficient method of identifying signals buried in noisy data if you know the shape of the signal you are looking for. The method performs a cross-correlation $c(\tau)$ between data $d(t)$ and a *filter* $K(t)$

$$c(\tau) \equiv \int_{-\infty}^{\infty} K(t+\tau)d(t)dt = \int_{-\infty}^{\infty} \tilde{K}^*(f)\tilde{d}(f)e^{-2\pi i f\tau}df \tag{1.80}$$

$$= 2\mathrm{Re}\int_{0}^{\infty} \tilde{K}^*(f)\tilde{d}(f)e^{-2\pi i f\tau}df. \tag{1.81}$$

The objective is to find an *optimal filter* that maximizes the cross-correlation for some value of τ. It has been shown [266, 236, 237] that an optimal filter is given by the GW signal $h(t)$ buried in the data divided by the PSD of the noise where by convention it is divided by the two-sided PSD [191] $S_n^d(f) \equiv S_n(f)/2$,

$$\tilde{K}_{\mathrm{opt}}(f) = \frac{\tilde{h}(f)}{S_n^d(f)} = 2\frac{\tilde{h}(f)}{S_n(f)}. \tag{1.82}$$

In general the exact shape of the signal will not be known ahead of time. In this case large sets of candidate optimal filters are generated called *template banks* and all the filters can be applied to the data to observe if any induce a significant correlation. If the optimal template $h(t)$ is replaced with a general template $g(t)$ then the *matched-filter SNR* ρ_m [44]

can be written as

$$\rho_m(\tau) = \frac{4\mathrm{Re}\int_0^\infty \frac{\tilde{g}^*(f)\tilde{d}(f)e^{-2\pi i f\tau}}{S_n(f)}df}{\sqrt{4\mathrm{Re}\int_0^\infty \frac{\tilde{g}^*(f)\tilde{g}(f)}{S_n(f)}df}} = \frac{\left\langle ge^{-2\pi i f\tau}|d\right\rangle}{\|g\|}, \tag{1.83}$$

where the *noise weighted inner product* for real valued functions $h(t)$ and $g(t)$ is defined as

$$\langle h|g\rangle \equiv 4\mathrm{Re}\int_0^\infty \frac{\tilde{h}^*(f)\tilde{g}(f)}{S_n(f)}df, \tag{1.84}$$

$$\|h\| \equiv \sqrt{\langle h|h\rangle} \tag{1.85}$$

where the notation for the *norm* $\|h\|$ is used to distinguish the norm with respect to the noise weighted inner product from the point-wise absolute value of the waveform $|h|$. The cross-correlation variable τ is degenerate with the coalescence time t_c for compact binaries and so it is typical to remove the exponential expression and simply define the matched-filter SNR as a single value $\rho_m = \langle g|d\rangle/\|g\|$.

For waveform modelling the noise weighted inner product provides a natural method to evaluate the closeness of different waveforms. The *match* M or *faithfulness* $\mathcal{F}$ between two waveforms $h(t)$ and $g(t)$ is defined as noise weighted inner product of the normalized waveforms $\hat{h} \equiv h/\|h\|$ and $\hat{g} \equiv g/\|g\|$ maximized over extrinsic parameters coalescence time t_c and phase ϕ_c

$$M(h,g) \equiv \mathcal{F} \equiv \max_{\phi_c,t_c}\left\langle \hat{h}(\phi_c,t_c)|\hat{g}\right\rangle. \tag{1.86}$$

This is used extensively during GW model development to compare with accurate GW signals such as from NR or to compare to other GW models. The match is often expressed as the *mismatch* $\mathcal{M} \equiv 1 - M$. Another measure that is also used is the *effectualness* $\mathcal{E}$ which is the noise weighted inner product now maximized over all parameters of the model

$$\mathcal{E}(h,g) \equiv \max_{\boldsymbol{\theta}}\left\langle \hat{h}(\boldsymbol{\theta})|\hat{g}\right\rangle. \tag{1.87}$$

In practice the noise weighted inner product and expressions that use it will not integrate over the entire range $f \in [0,\infty]$. While in most contexts the integration range will be described separately, it is sometimes useful to indicate the range in expressions. This is done using a subscript tuple of the bounds, for example the norm evaluated over $f \in [f_0, f_1]$ would be written as $\|h\|_{(f_0,f_1)}$.

1.7.2 Parameter estimation

One of the main GW data analysis tasks is estimating the parameters of any candidate GW signal in detector data. This task is normally performed within the framework of *Bayesian inference*. Given a model for GWs $h(\boldsymbol{\theta})$, the question of what are the most likely parameters

$\boldsymbol{\theta}$ if you have some detector data d can be written as,

$$P(\boldsymbol{\theta}|d,h) \propto \mathcal{L}(d|\boldsymbol{\theta},h)P(\theta|h), \tag{1.88}$$

which is interpreted as the probability $P(\boldsymbol{\theta}|d,h)$ of parameters $\boldsymbol{\theta}$ given the observed data d and model h is proportional to the probability $\mathcal{L}(d|\boldsymbol{\theta},h)$ of the data given parameters $\boldsymbol{\theta}$ and model h weighted by the probability $P(\theta|h)$ of the parameters given the model.

The last probability $P(\theta|h)$ is called the *prior* and is an essential concept in Bayesian inference that enables prior knowledge of parameters to be incorporated into future analysis. Often the prior is simply a uniform distribution over certain parameters, for example the prior probability of the signal phase ϕ_0 is typically chosen to be uniform between $\phi_0 \in [0, 2\pi]M_\odot$. However the prior does depend on the model being used. If an aligned spin model is being used then the priors on the spin component magnitudes should in general be different than the priors on the spin magnitudes for a precessing model. This is to correctly encode prior knowledge of isotropic spins for each component object [275].

The probability $\mathcal{L}(d|\boldsymbol{\theta},h)$ is known as the *likelihood*. The probability that data d contains a GW signal $h(\boldsymbol{\theta})$ is equivalent to saying that the residual of the data with respect to the candidate GW signal should be Gaussian. The likelihood function for Gaussian noise is known and so the likelihood can be written as,

$$\mathcal{L}(d|\boldsymbol{\theta},h) \equiv \exp\left(-\frac{\|d-h(\boldsymbol{\theta})\|^2}{2}\right). \tag{1.89}$$

In general the *posterior* distribution $P(\boldsymbol{\theta}|d,h)$ cannot be written down analytically. As such the process of parameter estimation through Bayesian inference is to estimate the posterior distribution through numerical methods. For GW parameter estimation two of the primary numerical methods are the Markov Chain Monte Carlo (MCMC) method using the Metropolis-Hasting [196, 146] algorithm and Nested sampling [250, 251]. For more details of GW parameter estimation using these method please see [275, 25].

Chapter 2

Modelling gravitational waves from neutron star black hole coalescences

2.1 Introduction

Stellar-mass compact-binary coalescences have been the source of all current gravitational-wave (GW) observations made by the Advanced LIGO [3] and Advanced Virgo detectors [30]. The data collected during the first and second observing runs is publicly available [271, 99], and analyses of it have been published in several GW catalogues [19, 276, 203, 204]. The compact-binary mergers expected to be observed by current ground-based detectors come in three varieties: black-hole binaries (BBHs), neutron-star binaries (BNSs), and binaries that consist of one black hole and one neutron star (NSBHs). The majority of GW signals detected so far comes from BBH mergers, with two detections, GW170817 [20] and GW190425 [26], inferred to be from BNS mergers. Although the GW signals from these two events are also consistent with NSBH mergers, *e.g.*, [101, 169], this class of merger has yet to be unambiguously observed.

To extract physical information from GW signals, template waveforms constructed from theoretical models are compared with the data using a Bayesian framework. Much of the previous waveform modelling efforts have focused successfully on BBHs — for examples of recent BBH waveform models, see `SEOBNRv4HM` [100], `PhenomPv3HM` [163, 165], and surrogates `NRSur7dq4` [273] and `NRHybSur3dq8` [274]. These BBH waveform models do not capture the changes to the waveform morphology introduced when one or both of the binary companions is a neutron star (NS). One effect is a shift to the waveform phase that arises from tidal deformation of the NS during the inspiral of the two bodies [126]. This shift has been the focus of recent research into BNS waveform modelling efforts, and has produced several available models: `TEOBResumS` [201], `SEOBNRv4T` [154, 257, 173], and the `NRTidal` models [103, 104, 105]. These phase corrections have been sufficient in observations to date, because disruption of the NSs produces changes in the GW amplitude at high frequency [98, 269, 80], where the detectors have been largely insensitive to the merger and post-merger BNS signal [131, 109].

In signals from NSBH systems, the phase shift during the inspiral stage due to NS tidal deformation is present, but it is unlikely that it will be observable with current detectors [216]. Further, and in contrast to BNS signals, merger and post-merger dynamics in NSBH systems are potentially accessible to current ground-based detectors due to these systems' potential for higher total masses, which can shift the GW signal at merger to a more sensitive part of the frequency band. As the mass-ratio of the system increases, the merger morphology of the waveform can range from total disruption of the NS, in which case the amplitude of the waveform is exponentially suppressed at high frequency [280], to non-disruptive signals for which the waveform is comparable to a BBH waveform, where the high-frequency amplitude is governed by the ringdown of the companion black hole (BH) [130]. Observations of the merger signal in an NSBH could allow us to place tighter constraints on the NS equation of state (EOS) [170, 171, 214] and identify its source as an NSBH binary. Of the waveform models existing currently, `LEA` [172] and the upgraded `LEA+` models are the only existing NSBH waveform models that include an NSBH-specific merger morphology and are calibrated against NSBH NR waveforms. While effective in their shared calibration range, their parameter space coverage is limited, in particular only to mass ratios between 2 and 5.

The aim of this chapter is to produce a new NSBH model called `PhenomNSBH` that combines an approximate reparameterization of the NSBH amplitude model described by [213] with the state-of-the-art tidal phase model described in [105]. As with previous work, the new model supports a spinning BH with spin vector parallel to the orbital angular momentum of the system and a non-spinning NS. Furthermore, the previous amplitude modelling efforts are simplified by replacing dependence on the NS EOS with a single tidal deformability parameter. This change is essential to allow the new model to be used for parameter estimation. With these changes to the amplitude model and the integration of an improved phase description, the new model is valid over a larger parameter space and it is capable of generating accurate waveforms from equal mass up to mass-ratio 15. At high mass ratios, the NS merges with the BH before disrupting, and the GW signal approaches that of an equivalent BBH. As will be shown in Sec. 2.3, beyond mass-ratio 8 a BBH model will be sufficient for observations with a signal-to-noise ratio less than 300. The material in this chapter has been published in [264].

In Sec. 2.2 the waveform model `PhenomNSBH` presented in this chapter is described and outlined, which is implemented as `IMRPhenomNSBH` in the open-source LIGO-Virgo algorithms library, LALSuite [180], which is the collection of collaboration reviewed and approved codes for official LIGO-Virgo analysis. To assess the `PhenomNSBH` model, it is compared against numerical-relativity (NR) data for various NSBH systems in Sec. 2.3, presenting alongside the same comparisons for other relevant waveform models, and the regions of parameter space where an NSBH model will be necessary to prevent measurement biases are identified. This chapter concludes with Sec. 2.4, where the results are summarized and directions for future work are discussed. In the remaining sections of this chapter geometric units are used such that $G = c = 1$.

2.2 Modelling neutron star-black hole waveforms

In this section a model for the GW signal emitted by an NSBH binary system is presented that consists of a non-spinning NS and a BH with spin angular momentum $\mathbf{S}_{\rm BH}$ parallel to the orbital angular momentum $\mathbf{L}$ of the system. Such a system may be parameterized by four intrinsic parameters: M, the total mass of the system, $M = M_{\rm BH} + M_{\rm NS}$, where $M_{\rm BH}$ and $M_{\rm NS}$ are the component masses of the BH and NS, respectively; q, the mass ratio of the system where $q = M_{\rm BH}/M_{\rm NS} \geq 1$; χ, the dimensionless spin of the BH given by $\chi = \mathbf{S}_{\rm BH} \cdot \hat{\mathbf{L}}/M_{\rm BH}^2$; and Λ, the dimensionless NS tidal deformability parameter [126, 153] defined in terms of the quadrupolar Love number, k_2, and compactness $C = M_{\rm NS}/R_{\rm NS}$ of the NS,

$$\Lambda = \frac{2}{3}\frac{k_2}{C^5}, \tag{2.1}$$

as previously described in Sec. 1.4.2. These four parameters are encapsulated in the vector $\boldsymbol{\theta} = (M, q, \chi, \Lambda)$. Note that, unlike BBH models, the total mass M cannot be separated as a scaling factor due to the scale-dependent effects that arise in the waveform from the presence of the NS.

A model of the complex strain in the frequency domain is required, $\tilde{h}(f; \boldsymbol{\theta}, \vartheta, \varphi)$, where the extrinsic parameters (ϑ, φ) represent the orientation of the system with respect to a distant observer. The strain may be written as an expansion in spin-weighted spherical harmonics ${}_{-2}Y_{\ell m}(\vartheta, \varphi)$. For the first step in this preliminary model, following previous phenomenological models [233, 159, 164, 213], focus is only on the dominant $(\ell, |m|) = (2, 2)$ multipole moments, *i.e.*,

$$\begin{aligned}\tilde{h}(f; \boldsymbol{\theta}, \vartheta, \varphi) &= \sum_{\ell,m} \tilde{h}_{\ell m}(f; \boldsymbol{\theta})\, {}_{-2}Y_{\ell m}(\vartheta, \varphi) \\ &\approx \sum_{m=\pm 2} \tilde{h}_{2m}(f; \boldsymbol{\theta})\, {}_{-2}Y_{2m}(\vartheta, \varphi).\end{aligned} \tag{2.2}$$

The $\tilde{h}_{22}$ multipole moment is further decomposed in terms of an amplitude A and phase ϕ,

$$\tilde{h}_{22}(f; \boldsymbol{\theta}) = A(f; \boldsymbol{\theta}) e^{-i\phi(f;\boldsymbol{\theta})}, \tag{2.3}$$

and note the relationship $\tilde{h}_{2-2}(f) = \tilde{h}^*_{22}(-f)$, where $*$ denotes complex conjugation. Higher multipoles are also necessary for unbiased parameter measurements for systems with $q \geq 3$ [272, 162]. A quadrupole-only model is however sufficient to capture the broad phenomenology of the signal from an NSBH system including the effects of tidal disruption, and for all of the conclusions that are drawn in this chapter. Further extensions will be discussed in Sec. 2.4.

In the text that follows, a detailed outline is presented for how the amplitude and phase are modelled for an NSBH system.

2.2.1 Waveform evaluation workflow

2.2.1.1 Amplitude model

To create an amplitude model for `PhenomNSBH` the NSBH amplitude description of Pannarale *et al.* in [213] is used as a starting point. This model describes an amplitude based on the aligned-spin BBH waveform amplitude of `PhenomC` [233], which depends on three intrinsic parameters (M, q, χ) and an explicit choice of a NS equation of state (EOS). Four choices of EOS were used in its calibration, listed in order of increasing softness, *i.e.*, decreasing tidal deformability: 2H, H, HB, and B [230]. Given an EOS and NS gravitational mass $M_{\rm NS}$ (assuming $M_{\rm NS} \leq M_{\rm BH}$), the amplitude model of Pannarale *et al.* integrates the Tolman-Oppenheimer-Volkoff equations [267, 268, 210] to find the NS radius $R_{\rm NS}$ associated with its gravitational mass. From the mass and radius, the NS compactness is computed via $C = M_{\rm NS}/R_{\rm NS}$ and the baryonic mass $M_{\rm b,NS}$ from Eq. (8) of [129].

While determination of the NS EOS may be possible after several detections [174], it is more practical for the new waveform model to not be directly dependent on the EOS . To this end, the dependency of the amplitude model on the EOS is replaced with a dependency on the dimensionless tidal deformability Λ, outlined in Sec. 2.2.3. With these augmentations made to the original amplitude model, a working amplitude for an aligned-spin NSBH system is obtained, with dependence on the four intrinsic parameters (M, q, χ, Λ). Based on the workflows provided in Ref. [215, 213], the amplitude model is evaluated using the following steps:

1. **Calculate the NS compactness** C
   Evaluate Eq. (2.29) to calculate compactness $C(\Lambda)$ of the NS.

2. **Calculate the tidal disruption frequency** $f_{\rm tide}$
   Evaluate Eq. (2.5) to calculate the tidal disruption frequency $f_{\rm tide}(q, \chi, C)$.

3. **Calculate the baryonic mass ratio** $M_{\rm b,torus}/M_{\rm b,NS}$
   Evaluate Eq. (2.8) to calculate the baryonic mass ratio of the NS. This model depends only on the torus remnant baryonic mass $M_{\rm b,torus}$ and the baryonic mass $M_{\rm b,NS}$ of the isolated NS at rest through expressions of the form $M_{\rm b,torus}/M_{\rm b,NS}$. As such it is not necessary to calculate an explicit value for $M_{\rm b,NS}$, which was required by [213].

4. **Calculate remnant BH properties** (χ_f, M_f)
   Evaluate Eq. (2.10) to calculate the final spin $\chi_f(\eta, \chi, \Lambda)$ and final mass $M_f(\eta, \chi, \Lambda)$ of the remnant black hole, where $\eta = q/(1+q)^2$ is the symmetric mass ratio.

5. **Calculate the remnant BH quantities** $(f_{\rm RD}, Q)$
   Evaluate Eqs. (2.13) and (2.14) to calculate the ringdown frequency $f_{\rm RD}(M_f, \chi_f)$ and quality factor $Q(\chi_f)$.

6. **Calculate merger-type dependent quantities**
   Calculate the merger-type dependent quantities $(\epsilon_{\rm tide}, \epsilon_{\rm ins}, \sigma_{\rm tide}, \tilde{f}_0, \tilde{f}_1, \tilde{f}_2)$ using the

conditions on $f_{\rm tide}$, $f_{\rm RD}$, and the magnitude of $M_{\rm b,torus}$, and expressions provided in Table 2.1.

7. **Calculate non-merger-type dependent quantities**
   Evaluate Eq. (2.28) to calculate the phenomenological parameters γ_1, δ_1, and δ_2. Evaluate Eqs. (2.23) and (2.26) to calculate the phenomenological correction parameters γ_1' and δ_2', respectively. While δ_1 and δ_2' are not explicitly dependent on any merger-type dependent quantities, they are not required if the onset of tidal disruption happens before the ringdown frequency is reached.

8. **Evaluate the amplitude**
   Evaluate the amplitude $A(f;\boldsymbol{\theta})$,

$$\begin{aligned} A(f) = & A_{\rm PN}(f)\omega^{-}_{\tilde{f}_0,0.015+\sigma_{\rm tide}}(f) \\ & + \gamma_1' f^{5/6}\omega^{-}_{\tilde{f}_1,0.015+\sigma_{\rm tide}}(f) \\ & + A_{\rm RD}(f)\omega^{+}_{\tilde{f}_2,0.015+\sigma_{\rm tide}}(f), \end{aligned} \tag{2.4}$$

   where the windowing functions $\omega^{\pm}_{f_0,d}(f)$ are defined by Eq. (2.27), which differ from the hybridization windowing functions $w^{\pm}_{t_0,t_1}(t)$ defined by Eqs. (1.75) and (1.76), and $A_{\rm PN}$ and $A_{\rm RD}$ are defined by Eqs. (2.22) and (2.24), respectively. All explicit parametrization in the component functions of the amplitude A have been suppressed for legibility.

A more detailed description of the amplitude model workflow is given in Sec. 2.2.2. For full details of the amplitude model, along with the different merger types, please see Sec. IV of Ref. [213].

2.2.1.2 Phase model

In addition to a proper amplitude description, a model is needed for the GW phase ϕ for the NSBH coalescence in such a way that it provides an accurate description within a large region of the parameter space and incorporates tidal effects imprinted in the signal. As a BBH baseline, the frequency-domain phase approximant from `PhenomD` [159, 164] is used. This model allows for a description of BBH systems up to mass ratios of $q \leq 18$ and aligned-spin components up to $|\chi| \leq 0.8$. This BH baseline is augmented with tidal effects modelled within the `NRTidal` approach [103, 104], using the newest version as described in Ref. [105]. The `NRTidal` phase model includes matter effects in the form of a closed-form, analytical expression, combining post-Newtonian knowledge with EOB and NR information. While this model was designed to be an accurate phase model for BNS systems, recent work [131] has shown that it is also a valid description in the NSBH limit.

2.2.2 Amplitude development

The high level evaluation workflow described in Sec. 2.2.1 provides a convenient overview of `PhenomNSBH`. In this section the individual parts that compose the amplitude of `PhenomNSBH` will be presented in more detail and explanations of why these parts were constructed.

To begin, the compactness of the NS is determined from the input tidal deformability, as described in detail in Sec. 2.2.3. The tidal disruption frequency $f_{\rm tide}$ is then computed, which approximates the frequency at which the external quadrupolar tidal force acting on the NS from the companion BH is comparable in magnitude to the self-gravitating force maintaining the NS. This follows from the initial parameters of the binary according to [129, 248]

$$f_{\rm tide} = \frac{1}{\pi\left(\chi M_{\rm BH} + \sqrt{\tilde{r}_{\rm tide}^3/M_{\rm BH}}\right)}, \tag{2.5}$$

$$\tilde{r}_{\rm tide} = \xi_{\rm tide} M_{\rm BH} \frac{(1-2C)}{\mu}, \tag{2.6}$$

where $\mu = qC$ and $\xi_{\rm tide}$ is the largest positive real root of the following equation,

$$0 = \xi_{\rm tide}^5 - 3\mu\xi_{\rm tide}^4 + 2\chi\sqrt{\mu^3\xi_{\rm tide}^7} - 3q\xi_{\rm tide}^2 + 6q\mu\xi_{\rm tide} - 3q\mu^2\chi^2. \tag{2.7}$$

Next, the ratio of the baryonic mass of the torus remaining after merger to the initial baryonic mass of the NS, $M_{\rm b,torus}/M_{\rm b,NS}$, is determined according to fits from [129],

$$\frac{M_{\rm b,torus}}{M_{\rm b,NS}} = 0.296\xi_{\rm tide}(1-2C) - 0.171qC\bar{r}_{\rm ISCO}, \tag{2.8}$$

where $\bar{r}_{\rm ISCO}$ is the radius of the innermost stable circular orbit of a unit-mass BH [60],

$$\begin{aligned}
\bar{r}_{\rm ISCO} &= \left[3 + Z_2 - {\rm sign}(\chi)\sqrt{(3-Z_1)(3+Z_1+2Z_2)}\right], \\
Z_1 &= 1 + \left(1-\chi^2\right)^{1/3}\left[(1+\chi)^{1/3} + (1-\chi)^{1/3}\right], \\
Z_2 &= \sqrt{3\chi^2 + Z_1^2}.
\end{aligned} \tag{2.9}$$

The fit for $M_{\rm b,torus}$ was recently updated in Ref. [132]; incorporating it in the amplitude model would require recalibrating the NSBH amplitude model itself as a whole and is left for future work.

The final mass, M_f, and final spin, χ_f, of the remnant BH after merger are calculated using NSBH-specific fits for the remnant properties parameterized by tidal deformability [282],

$$F(\eta,\chi,\Lambda) = F_{\rm BBH}(\eta,\chi)\frac{1 + p_1(\eta,\chi)\Lambda + p_2(\eta,\chi)\Lambda^2}{\left(1 + [p_3(\eta,\chi)]^2\Lambda\right)^2}, \tag{2.10}$$

$$p_k(\eta,\chi) = p_{k1}(\chi)\eta + p_{k2}(\chi)\eta^2, \tag{2.11}$$

$$p_{kj}(\eta,\chi) = p_{kj0}\chi + p_{kj1}. \tag{2.12}$$

Merger type	**non-disruptive** *(no torus remnant)*	**mildly disruptive** *(torus remnant)*	**mildly disruptive** *(no torus remnant)*	**disruptive** *(torus remnant)*
	$f_{\rm tide} \geq f_{\rm RD}$		$f_{\rm tide} < f_{\rm RD}$	
	$M_{\rm b,torus} = 0$	$M_{\rm b,torus} > 0$	$M_{\rm b,torus} = 0$	$M_{\rm b,torus} > 0$
$\epsilon_{\rm tide}$	$\omega^{+}_{x_1,d_1}(x_{\rm ND})$ $[x_1 = -0.0796251, d_1 = 0.0801192]$		0.0	0.0
$\epsilon_{\rm ins}$	1.0	$1.29971 - 1.61724 x_D$		
$\sigma_{\rm tide}$	$\omega^{-}_{x_2,d_2}(x'_{\rm ND})$ $[x_2 = -0.206465, d_2 = 0.226844]$		$(\omega^{-}_{x_2,d_2}(x'_{\rm ND}) + 0.137722 - 0.293237 x'_{\rm D})/2$	$0.137722 - 0.293237 x'_{\rm D}$
$\tilde{f}_0$	$\tilde{f}_{\rm RD}$	$\epsilon_{\rm ins}\tilde{f}_{\rm RD}$	$[(q-1)\tilde{f}_{\rm RD} + \epsilon_{\rm ins} f_{\rm tide}]/q$	$\epsilon_{\rm ins} f_{\rm tide}$
$\tilde{f}_1$	$\tilde{f}_{\rm RD}$	$\epsilon_{\rm ins}\tilde{f}_{\rm RD}$	$[(q-1)\tilde{f}_{\rm RD} + f_{\rm tide}]/q$	$f_{\rm tide}$
$\tilde{f}_2$	$\tilde{f}_{\rm RD}$		–	–

Table 2.1: Summary of merger type dependent components of the amplitude model. For the definitions of $x_{\rm ND}$, $x'_{\rm ND}$, $x_{\rm D}$ and $x'_{\rm D}$, see Eqs. (2.18)-(2.21) in Sec. 2.2.2. Note that all applications of window functions $\omega^{\pm}$ for merger-type dependent quantities are a factor of two smaller to correct for a typographical error in [213]. The adjusted ringdown frequency is defined as $\tilde{f}_{\rm RD} = 0.99 \times 0.98 f_{\rm RD}$ for $\Lambda > 1$ and $\tilde{f}_{\rm RD} = 0.98 f_{\rm RD}$ for $\Lambda = 0$ with a smooth interpolation given by Eq. (2.17).

The remnant model $F_{\rm BBH}$ is the model for the final mass and spin of a BBH coalescence described in [161], and the coefficients p_{kji} for the final mass M_f and final spin χ_f can be found in the supplementary material for [282]. Once the final mass and spin are determined, the ringdown frequency $f_{\rm RD}$ and quality factor Q are calculated via,

$$f_{\rm RD} = \frac{{\rm Re}(\tilde{\omega})}{2\pi M_f}, \tag{2.13}$$

$$Q = \frac{{\rm Re}(\tilde{\omega})}{2{\rm Im}(\tilde{\omega})}, \tag{2.14}$$

where $\tilde{\omega}$ is a fit to the $(l, m, n) = (2, 2, 0)$ Kerr quasi-normal mode frequency given in [184],

$$\begin{aligned}\tilde{\omega}(\kappa) = {} & 1.0 + 1.5578 e^{2.9031 i}\kappa \\ & + 1.9510 e^{5.9210 i}\kappa^2 + 2.0997 e^{2.7606 i}\kappa^3 \\ & + 1.4109 e^{5.9143 i}\kappa^4 + 0.4106 e^{2.7952 i}\kappa^5,\end{aligned} \tag{2.15}$$

$$\kappa(\chi_f) = \sqrt{\log_3(2 - \chi_f)}. \tag{2.16}$$

The amplitude ansatz in Eq. (2.4) uses the merger-type-dependent frequencies $\tilde{f}_0$, $\tilde{f}_1$, and $\tilde{f}_2$ to blend the post-Newtonian, pre-merger, and merger-ringdown amplitude contributions

together. These frequencies are determined based on the conditions in Table 2.1. Not listed are the specific functional form of the various component functions $x_{\rm ND}$, $x'_{\rm ND}$, $x_{\rm D}$ and $x'_{\rm D}$ of the merger-type dependent quantities given in [213]. The non-disruptive fitting functions $x_{\rm ND}$ and $x'_{\rm ND}$ also require the scaled ringdown frequency $\tilde{f}_{\rm RD}$ calculated according to

$$\tilde{f}_{\rm RD} = \begin{cases} 0.99 \times 0.98 f_{\rm RD}, & \Lambda > 1 \\ (1 - 0.02\Lambda + 0.01\Lambda^2) \times 0.98 f_{\rm RD}, & \Lambda \leq 1, \end{cases} \tag{2.17}$$

$$\begin{aligned} x_{\rm ND} = &\left(\frac{f_{\rm tide} - \tilde{f}_{\rm RD}}{\tilde{f}_{\rm RD}} \right)^2 - 0.571505C \\ &- 0.00508451\chi, \end{aligned} \tag{2.18}$$

$$\begin{aligned} x'_{\rm ND} = &\left(\frac{f_{\rm tide} - \tilde{f}_{\rm RD}}{\tilde{f}_{\rm RD}} \right)^2 - 0.657424C \\ &- 0.0259977\chi, \end{aligned} \tag{2.19}$$

$$\begin{aligned} x_{\rm D} = &\frac{M_{\rm b,torus}}{M_{\rm b,NS}} + 0.424912C \\ &+ 0.363604\sqrt{\eta} - 0.060559\chi, \end{aligned} \tag{2.20}$$

$$\begin{aligned} x'_{\rm D} = &\frac{M_{\rm b,torus}}{M_{\rm b,NS}} - 0.132754C + 0.576669\sqrt{\eta} \\ &- 0.0603749\chi - 0.0601185\chi^2 \\ &- 0.0729134\chi^3. \end{aligned} \tag{2.21}$$

The amplitude component function for the inspiral, $A_{\rm PN}$, is given by the Fourier transform of the time-domain amplitude given in Eq. (3.14) of [233] using the stationary phase approximation,

$$A_{\rm PN}(x) = \sqrt{\frac{2\pi}{3\dot{x}\sqrt{x}}} 8\eta x \sqrt{\frac{\pi}{5}} \sum_{k=0}^{6} \mathcal{A}_k x^{k/2}, \tag{2.22}$$

where $x = \omega^{2/3}$, ω is the orbital angular frequency of the binary, and $\dot{x}$ is computed using the TaylorT4 expansion [85]; see [233] for the expansion coefficients $\mathcal{A}_i$.

The phenomenological correction parameter γ'_1 for the pre-merger region is calculated according to,

$$\gamma'_1 = \begin{cases} 1.25, & \Lambda > 1 \\ 1 - 0.5\Lambda - 0.25\Lambda^2, & \Lambda \leq 1. \end{cases} \tag{2.23}$$

The merger-ringdown component function $A_{\rm RD}$ is defined by [213],

$$A_{\rm RD}(f) = \epsilon_{\rm tide} \delta_1 \frac{\sigma^2}{(f - f_{\rm RD})^2 + \sigma^2/4} f^{-7/6}, \tag{2.24}$$

$$\sigma = \delta'_2 f_{\rm RD}/Q, \tag{2.25}$$

where the phenomenological correction parameter δ_2' is calculated according to,

$$\delta_2' = \begin{cases} \frac{A}{2}\omega^-_{x_3,d_3}\left(\frac{f_{\rm tide}-\tilde{f}_{\rm RD}}{\tilde{f}_{\rm RD}}\right), & \Lambda > 1 \\ \delta_2 - 2\left(\delta_2 - b_0\right)\Lambda + \left(\delta_2 - b_0\right)\Lambda^2, & \Lambda \leqslant 1 \end{cases} \tag{2.26}$$

with $A = 1.62496$, $x_3 = 0.0188092$, and $d_3 = 0.338737$, $b_0 = 0.81248$ and $\omega^{\pm}_{f_0,d}(f)$ is a hyperbolic tangent windowing function,

$$\omega^{\pm}_{f_0,d}(f) = \frac{1}{2}\left[1 \pm \tanh\left(\frac{4(f-f_0)}{d}\right)\right]. \tag{2.27}$$

Note that the factor of 1/2 multiplying the windowing function $\omega^-_{x_3,d_3}$ in Eq. (2.26) corrects a typographical error in [213]. The `PhenomC` phenomenological parameters δ_1, δ_2 and γ_1 are given as an expansion in symmetric mass-ratio and spins by,

$$\delta_1, \delta_2, \gamma_1 \sim \sum_{i+j\in\{1,2\}} \zeta^{ij}\eta^i\chi^j, \tag{2.28}$$

with the coefficients ζ^{ij} in the δ_1, δ_2, and γ_1 fit parameters given in [233]. Also imposed are the additional constraints that $\delta_1, \gamma_1 \geq 0$ and $\delta_2 \geq 10^{-4}$ to ensure that the amplitude function Eq. (2.4) remains positive for all regions of parameter space that `PhenomNSBH` is expected to be used in. It is necessary to invoke these constraints on these coefficients in the non-spinning limit for $q > 25$ and $q > 15$ for spinning cases. In this region the model no long remains sensible and comparisons between other BBH waveforms break down. This constraint on the coefficients motivates the suggested upper bound placed on the mass ratio for the parameter space of the model.

2.2.3 Replacing Equation of State

Removing explicit EOS-dependence from the NSBH amplitude model is achieved by finding the compactness C of the NS from its tidal deformability parameter Λ using the fit determined in Ref. [279] with an additional piecewise component for $\Lambda \leq 1$ from [193],

$$C(\Lambda) = \begin{cases} a_0 + a_1\log\Lambda + a_2(\log\Lambda)^2, & \Lambda > 1 \\ 0.5 + (3a_0 - a_1 - 1.5)\Lambda^2 & \\ \qquad + (a_1 - 2a_0 + 1)\Lambda^3, & \Lambda \leq 1, \end{cases} \tag{2.29}$$

where $a_0 = 0.360$, $a_1 = -0.0355$, and $a_2 = 0.000705$. Fig. 2.1 shows how the compactness values yielded by this fit compare to those directly obtained from the EOS information presented in [172] by integrating the Tolman-Oppenheimer-Volkoff equations [267, 268, 210].

As the original model was calibrated only to a specific set of EOSs, replacing EOS-

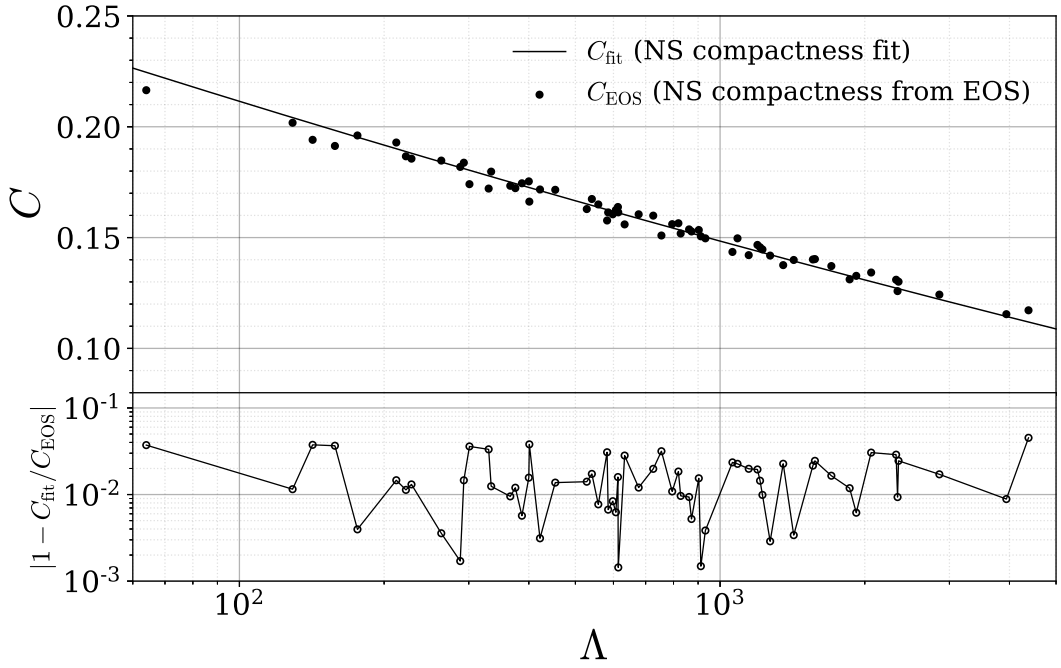

Figure 2.1: Comparison between the NS compactness as calculated from the EOS information presented in [172] and the NS compactness fit from [279] which has a root-mean-squared relative percentage error of 1.95% and maximum relative percentage error of 4.52%.

dependence with the fit in Eq. (2.29) will invariable introduce some error to the amplitude model. The effects of this error on the model are conservatively estimated in the following way.

The error in the fit model is given pessimistically as a 6% error in the computed value of C across realistic NS EOSs [279]; for the EOSs used in the calibration of the amplitude model, the error in the fit is bounded by 5%. The mapping in Eq. (2.29) is inverted and then the spread in Λ produced around a given Λ_0 is computed by varying the compactness within the 6% error bounds. Matches are then computed across the parameter space of `PhenomNSBH` between two waveforms with all parameters equal except the tidal deformability, which is fixed at Λ_0 for one waveform and allowed to vary between the bounds determined from the compactness error for the other. After sampling waveforms across the model's parameter space, a maximum mismatch of $\sim 10^{-3}$ is found for the pessimistic 6% error estimate in the fit.

2.3 Analysis of model

To quantify the effectiveness of the model at reproducing NSBH waveforms, it is compared against a selection of NR NSBH waveforms produced by the SXS collaboration [130, 93, 131] with simulation parameters listed in Table 2.2. To carry out these comparisons, it is useful

Name	SXS Name	q	$M_{\rm BH}$	$M_{\rm NS}$	$\chi_{\rm NS}$	Λ	Merger Type
q1a0	SXS:BHNS:0004	1	1.4	1.4	0	791	Disruptive
q1.5a0	SXS:BHNS:0006	1.5	2.1	1.4	0	791	Disruptive
q2a0	SXS:BHNS:0002	2	2.8	1.4	0	791	Disruptive
q3a0	SXS:BHNS:0003	3	4.05	1.35	0	607	Mildly Disruptive
q6a0	SXS:BHNS:0001	6	8.4	1.4	0	525	Non-disruptive
q1a2	SXS:BHNS:0005	1	1.4	1.4	-0.2	791	Disruptive
q2a2	SXS:BHNS:0007	2	2.8	1.4	-0.2	791	Disruptive

Table 2.2: SXS waveforms [130, 93, 131] and their parameters used for comparisons and in making the hybrids. Along with the name given in the SXS public catalog, an abbreviated name given to each waveform in this chapter is also listed.

to introduce the notion of the *overlap* between two waveforms h_1 and h_2,

$$\langle h_1|h_2\rangle = 4\mathrm{Re}\int_{f_1}^{f_2}\frac{\tilde{h}_1(f)\tilde{h}_2^*(f)}{S_n(f)}\mathrm{d}f, \tag{2.30}$$

which is the functional inner-product introduced in Sec. 1.7 weighted by the detector noise power-spectral density, $S_n(f)$, taken for this chapter to be the Advanced LIGO zero-detuned, high-power (AZDHP) noise curve [249], which is the current goal for the detector's design sensitivity. By maximizing the normalized overlap over phase (ϕ_c) and time (t_c) shifts to h_1, one determines the *faithfulness* with which h_1 represents h_2,

$$\mathcal{F} = \max_{\phi_c,t_c}\frac{\langle h_1(\phi_c,t_c)|h_2\rangle}{\|h_1\|\|h_2\|}. \tag{2.31}$$

As an initial test of the model, `PhenomNSBH` is compared against the `LEA+` model [172]. The original `LEA` model was constructed as a phenomenological NSBH model from baseline `PhenomC` [233] and `SEOBNR` [262] BBH waveform models. Additions to the BBH models were made to include tidal PN terms during the inspiral, and a taper was applied to the merger contributions of the waveform that was calibrated against NSBH NR waveforms. The `LEA+` model was introduced as an improvement to the `LEA` model by substituting a reduced-order model of `SEOBNRv2` [261] for the underlying BBH waveform. The `LEA+` model is calibrated for NS masses ranging between $1.2-1.4M_\odot$, mass-ratios $q\in[2,5]$, and BH spins $-0.5\leq\chi\leq 0.75$. To perform the comparison, waveforms are generated across the overlapping parameter spaces covered by the calibration ranges of `LEA+` and `PhenomNSBH` and the faithfulness between waveforms generated using identical parameters is computed. The results show good agreement between the models, with $\mathcal{F}>0.99$. The comparison only deviates noticeably when $\chi<-0.4$, where the faithfulness drops to 0.98.

2.3.1 Comparison to numerical relativity

NR simulations typically cover the last orbits before coalescence. For the NSBH NR waveforms that are considered in validating the model, the typical starting GW frequency

Sim Name	PhenomNSBH	PhenomD	PhenomDNRT	SEOBNRv4NRT	SEOBNRv4T	LEA+
q1a0	0.988 (0.978)	0.911 (0.834)	0.986 (0.972)	0.988 (0.976)	0.997 (0.994)	-
q1.5a0	0.997 (0.994)	0.955 (0.906)	0.998 (0.995)	0.998 (0.995)	0.999 (0.997)	-
q2a0	0.999 (0.997)	0.973 (0.931)	0.994 (0.983)	0.994 (0.983)	0.997 (0.994)	0.999 (0.997)
q3a0	0.994 (0.990)	0.984 (0.971)	0.929 (0.841)	0.930 (0.842)	0.983 (0.963)	0.994 (0.994)
q6a0	0.999 (0.998)	0.999 (0.999)	0.893 (0.842)	0.893 (0.842)	0.983 (0.966)	-
q1a2	0.894 (0.844)	0.809 (0.701)	0.885 (0.822)	0.888 (0.826)	0.900 (0.850)	-
q2a2	0.986 (0.974)	0.947 (0.900)	0.992 (0.985)	0.994 (0.988)	0.985 (0.969)	0.964 (0.944)

Table 2.3: The computed faithfulness between the seven SXS NSBH numerical relativity waveforms and the waveform approximants PhenomNSBH, PhenomD, PhenomDNRT, SEOBNRv4T, SEOBNRv4NRT, and LEA+. Two sets of matches are computed. The first uses the Advanced LIGO zero-detuning, high-power noise curve and second, in parentheses, uses a flat noise curve. The frequency range used to compute the matches cover the entire bandwidth of the NR data.

is between 300–400 Hz and covers between 10 and 16 orbits before merger. Currently Advanced LIGO and Virgo are sensitive to signals starting around 20 Hz, which for a true signal will include on the order of 10^3 orbits prior to merger, and therefore the NR waveforms used here are missing a large portion of the inspiral signal [208]. This issue is addressed by constructing hybrid waveforms for comparison against the model; the results of a comparison against hybrid waveforms can be found in Sec. 2.3.2. First, a comparison is made against the NR data directly in order to assess the accuracy of the model during the late-inspiral and merger.

The results from comparing directly with the NR waveforms are given in Table 2.3, and the faithfulness is computed over the frequency range covered by each NR waveform. Results from using the AZDHP (design) noise curve are provided, as well as a flat noise curve (in parentheses). The faithfulness of several other waveform models is also computed to gauge the systematic uncertainty that is incurred by using them. Specifically, comparisons are also made against the NSBH model LEA+ [172], an inspiral NSBH model SEOBNRv4T [154, 257], a BBH model PhenomD [159, 164] and two inspiral BNS models PhenomDNRT [104, 105, 159, 164] and SEOBNRv4NRT [104, 105, 71] [1].

In Ref. [131] the authors analyse the same NR waveforms and the same models. Similar results are also found in this chapter and are plotted in Fig. 2.2. Although that work focuses on the agreement between the model and NR by studying the de-phasing, here the focus is on computing the faithfulness, which is directly related to the loss in signal-to-noise ratio in matched-filter based searches, and takes into account both phase and amplitude differences.

Of the seven NR simulations considered in this chapter, five are binary systems without any spin on either body (see Table 2.2 for a list of the non-spinning waveforms and their parameters). The two cases including spin, q1a2 and q2a2, are simulations where the NS

[1]The approximant names in the LALSuite code for LEA+, PhenomD, PhenomDNRT, SEOBNRv4T and SEOBNRv4NRT are Lackey_Tidal_2013_SEOBNRv2_ROM, IMRPhenomD, IMRPhenomD_NRTidalv2, SEOBNRv4T and SEOBNRv4_ROM_NRTidalv2, respectively.

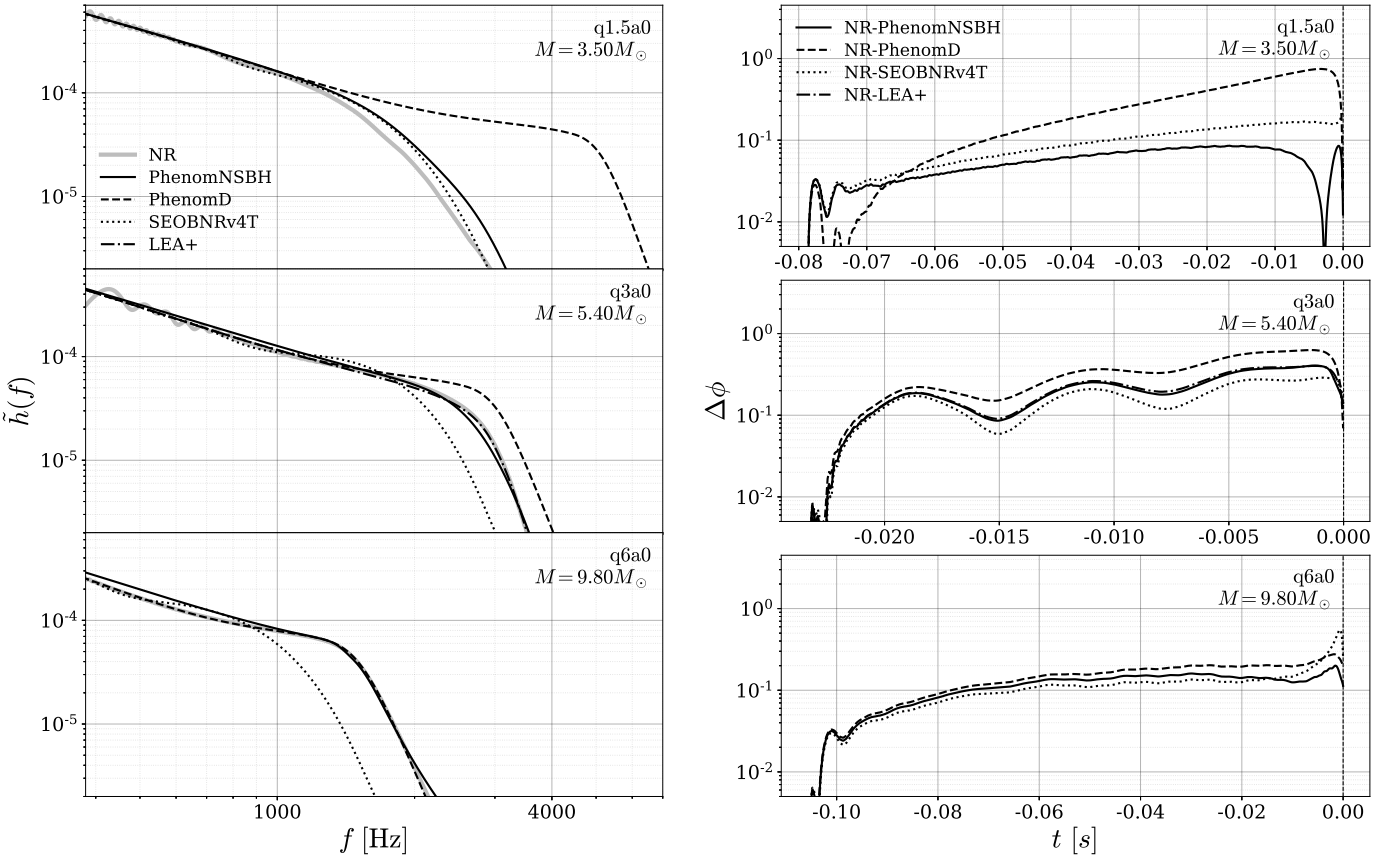

Figure 2.2: Comparisons between NR waveforms and various models. The left-most plots show $\tilde{h}(f)$ for each NR case over the last few orbits before merger, along with frequency-domain representations of the signal using various approximants. The right-most plots display the accumulated time-domain phase error between the NR phase and each approximant over the length of the NR data, and the approximant signals are aligned by time- and phase-shifts to the NR data over a few GW cycles near the start of each NR simulation. Only the `q3a0` case falls within the parameter space coverage of the `LEA+` model.

is spinning with a dimensionless spin magnitude of 0.2 in a direction anti-parallel to the orbital angular momentum. The amplitude model used for the `PhenomNSBH` is not calibrated for spinning NSs, and so these two NR waveforms allow for an exploration of the viability of the model when the NS is spinning. No direct comparisons are made to NR where the BH is spinning as no such simulations are currently publicly available. The amplitude model used in this chapter was calibrated against NSBH NR waveforms with a spinning BH. Furthermore, based on the faithfulness comparisons with `LEA+`, which is also calibrated to and validated against NSBH NR waveforms with a spinning BH, it is expected for the model to also perform well where the BH is spinning.

For q1a2, when compared against the BBH model `PhenomD` the match is 0.809 (0.701) for the AZDHP (flat) noise curve. Including tidal effects in the model does improve the match where a match of ~ 0.89 (~ 0.84) is found for the AZDHP (flat) noise curve. For q2a2, the match is not as bad as q1a2 but the results are, in general, worse than the non-

Sim Name	PhenomNSBH	PhenomD	PhenomDNRT	SEOBNRv4NRT	SEOBNRv4T	LEA+
q1a0	0.9996 (0.9996)	0.9906 (0.9936)	0.9985 (0.9989)	0.9992 (0.9994)	0.9968 (0.9982)	-
q1.5a0	0.9994 (0.9997)	0.9930 (0.9952)	0.9991 (0.9993)	0.9979 (0.9984)	0.9973 (0.9981)	-
q2a0	0.9987 (0.9990)	0.9954 (0.9966)	0.9989 (0.9993)	0.9969 (0.9978)	0.9970 (0.9976)	0.9997 (0.9998)
q3a0	0.9995 (0.9997)	0.9956 (0.9975)	0.9990 (0.9993)	0.9975 (0.9984)	0.9993 (0.9995)	0.9990 (0.9990)
q6a0	0.9974 (0.9981)	0.9964 (0.9972)	0.9946 (0.9974)	0.9957 (0.9972)	0.9977 (0.9988)	-
q1a2	0.9969 (0.9978)	0.9405 (0.9508)	0.9949 (0.9967)	0.9962 (0.9972)	0.9965 (0.9975)	-
q2a2	0.9991 (0.9992)	0.9806 (0.9837)	0.9985 (0.9992)	0.9988 (0.9990)	0.9982 (0.9989)	0.4515 (0.6070)

Table 2.4: The computed faithfulness between the seven SXS NSBH numerical relativity hybrid waveforms. These have been hybridized with the `TEOBResumS` model with a start frequency of 20 Hz. Comparisons are made against the waveform approximants `PhenomNSBH`, `PhenomD`, `PhenomDNRT`, `SEOBNRv4T`, `SEOBNRv4NRT`, and `LEA+`. Two sets of matches are computed. The first uses the Advanced LIGO zero-detuning, high-power noise curve and second, in parentheses, uses a flat noise curve. The frequency range used to compute the matches cover the entire bandwidth of the hybrid waveforms, down to a lower frequency bound of 20 Hz.

spinning cases. Interestingly, `PhenomD` and `LEA+` are found to perform comparably for this case with matches of ~ 0.95 (~ 0.90) and ~ 0.96 (~ 0.94) for the AZDHP (flat) noise curve, respectively.

Reference [131] showed that the NR phase error is smaller than the systematic modelling error in the original `NRTidal` phase approximant model. Similarly, the analysis in this chapter finds a noticeable phase difference between the phase description employed in `PhenomNSBH` and the NR data. These results suggest that further improvements such as a new phase calibration to NSBH NR simulations or the inclusion of spin-dependent f-mode resonance shifts near merger [154] may be important to include. In the next Section, however, is it shown that the measured dephasing is not an issue for Advanced LIGO at design sensitivity.

2.3.2 Comparison to hybrid numerical-relativity waveforms

The comparisons performed above are now repeated, but now hybridized NR waveforms are used to test the accuracy of the models for realistic signals including the thousands of inspiral cycles prior to merger. To do this, hybrid waveforms are produced, attaching the SXS NSBH waveforms listed in Table 2.2 to the tidal inspiral approximant `TEOBResumS` [201], following the hybridization procedure outlined in [155, 104]. These hybrids have a starting frequency below 20 Hz and allow us to test the models in a realistic observational scenario where a current-generation ground-based detector would also be sensitive to the full inspiral from 20 Hz; for the faithfulness integrals low frequency cutoff of 20 Hz is used. The accuracy of the hybrid construction method has been verified and it is found that the mismatch of a given hybrid with respect to itself subject to varying the hybridization parameters is $\mathcal{O}(10^{-4})$.

The results of the faithfulness calculations are listed in Table 2.4. In general it is found that the matches are very high, even when comparing the NSBH hybrids against BBH models, with the exception of the spinning NSBH waveform `q1a2`. At the total masses considered here, the signal-to-noise ratio (SNR) detectable in Advanced LIGO is dominated

by the long inspiral, and as a result inaccuracies in the waveform model during merger contribute much less to the total SNR. Note also that, as the hybrids were constructed with the `TEOBResumS` model as the inspiral approximant, it is encouraging that strong agreement is found between models with different tidal inspiral approximants.

2.3.3 Importance of NSBH-specific contributions

The distinguishing difference in the model of an NSBH waveform from a BBH waveform is its behaviour close to merger, where strong tidal effects lead to de-phasing of the binary from the standard BBH phase and may lead to disruption of the NS, thereby greatly tapering the amplitude. As the total mass of the NSBH system for this model is expected to be relatively low (not exceeding $\sim 45M_\odot$), these effects will occur at high frequencies where current ground-based detectors are not highly sensitive. One must then ask how important these effects are to the overall model of the waveform for current and future detectors, and how distinguishable the NSBH-specific effects are from BBH or BNS systems.

To estimate the importance of tidal effects and disruption for the detectability of an NSBH signal, the SNR is computed at which the NSBH waveform deviates from other waveform approximants covering the parameter space for these merger types; in particular, comparisons are made against both `PhenomNSBH` with $\Lambda = 0$ to simulate a purely BBH waveform and `PhenomDNRT`, which contains the same phase model as `PhenomNSBH` but has a taper applied to the high-frequency merger content of the waveform.

Given an NSBH signal with four internal degrees-of-freedom (M, q, χ, Λ), the SNR ρ associated with a 90% confidence region in parameter space for detection is related to the faithfulness $\mathcal{F}$ between the NSBH signal (here produced by `PhenomNSBH`) and another waveform approximant via [59]

$$\mathcal{F} = 1 - \frac{3.89}{\rho^2}\,. \tag{2.32}$$

Initially a series of NSBH waveforms are computed using fixed intrinsic parameters, $M_{\rm NS} = 1.35M_\odot$, $\chi = 0$, $\Lambda = 400$, and the mass ratio is allowed to vary between 1 and 8. This ensures that all merger types captured by the amplitude model are evaluated in the comparison.

The SNR resulting from these comparisons is plotted in Fig. 2.3. Focusing first on the distinguishability SNR between `PhenomNSBH` and `PhenomDNRT`, it is seen that the two models will be easier to distinguish with a modestly loud signal in an Advanced LIGO-type detector as the mass ratio of the system increases. In the NSBH system, the mass scale is fixed by the NS mass and therefore as q increases, so too does the total mass M. This increase in M will push the merger regime of the system into a lower (and more sensitive) frequency band in the detector, making the high-frequency taper applied to the `NRTidal` model more apparent in the faithfulness calculation. At lower q in the disruptive regime of the NSBH system, the taper applied to the `NRTidal` model mimics the disruption at high frequency in the NSBH waveform. Furthermore, these differences between the two models occur at such high frequency that the lack of sensitivity in the detector makes them hard to

distinguish.

When looking at the comparison between PhenomNSBH with and without tidal effects (*i.e.*, comparing against a BBH waveform), the inverse behaviour with changing q is observed. Even though the disruptive mergers of comparable-mass NSBH binaries lie outside the most sensitive frequency ranges of ground-based detectors, the differences in the waveforms due to tidal effects in the inspiral still allow us to distinguish between BBH and NSBH systems above SNR of 28. This observation is consistent with GW170817 [20] that had an SNR of 32.4 and allowed us to bound the mass-weighted tidal deformability $\tilde{\Lambda}$ away from zero. As the mass ratio increases, tidal effects scale away as q^{-4} in the phase and the NSBH signal becomes hard to differentiate from a BBH signal in the non-disruptive regime; the only differences between the two models are the properties of the remnant quantities after merger.

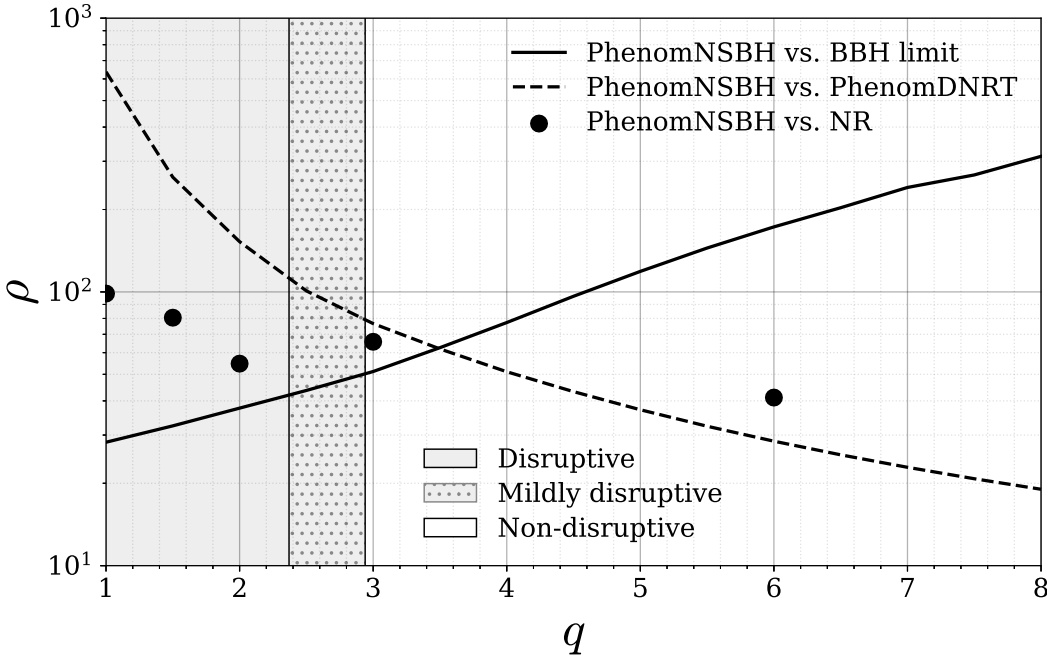

Figure 2.3: The approximate SNR at which the waveforms PhenomDNRT and the BBH-limit of PhenomNSBH become distinguishable from PhenomNSBH is plotted as a function of mass-ratio for a non-spinning NSBH system with tidal deformability $\Lambda = 400$ and NS mass $1.35M_\odot$. The shaded regions of the plot indicate different merger types calculated from PhenomNSBH. The solid dots show the SNR computed from mismatches between PhenomNSBH and the NR-hybrid data listed in Table 2.4. The trends continue to higher mass ratios, where an NSBH signal becomes effectively indistinguishable from a BBH signal in any realistic detection. The matches between models are computed over the range $[f_1, f_2] = [25, 8192]$Hz assuming a AZDHP noise curve.

This comparison is expanded to include the broader parameter space covered by PhenomNSBH. Specifically, a AZDHP noise curve is assumed and the distinguishability SNR is calculated between PhenomNSBH and its BBH limit, and between PhenomNSBH and PhenomDNRT for $\sim 5 \times 10^3$ NSBH systems with randomly chosen properties. $M_{\rm NS}$ is uniformly sampled between $1.0\,M_\odot$ and $2.3\,M_\odot$, $M_{\rm BH}$ between $1.0\,M_\odot$ and $27\,M_\odot$ (and $M_{\rm NS} \leq M_{\rm BH}$ is

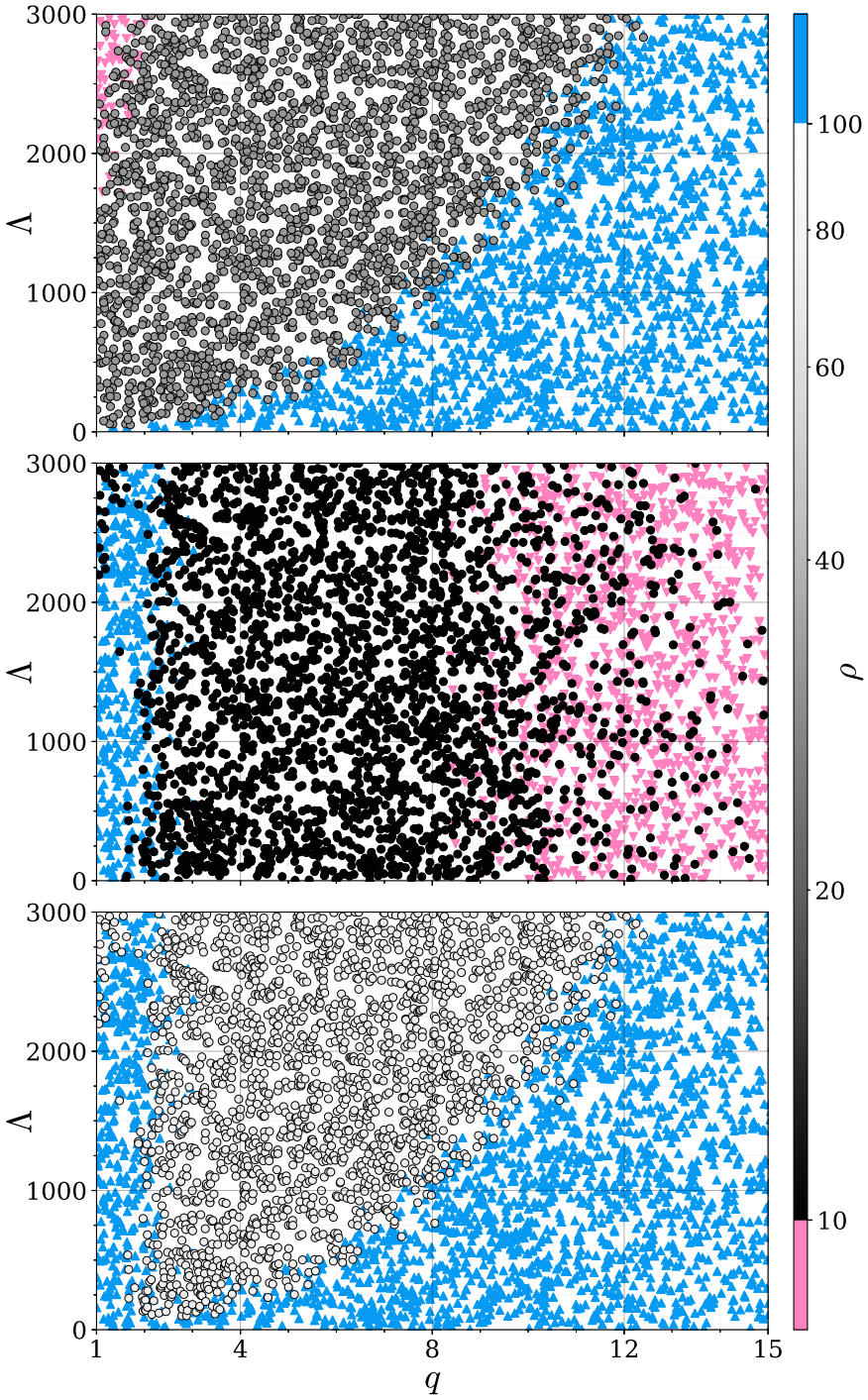

Figure 2.4: The approximate SNR at which the waveforms for BNS (`PhenomDNRT`) and BBH (the BBH-limit of `PhenomNSBH`) become distinguishable from NSBH (`PhenomNSBH`), considered over the entire parameter space of `PhenomNSBH` and projected onto the q-Λ plane. The top panel displays the distinguishability of `PhenomNSBH` from its BBH-limit, the middle panel the distinguishability of `PhenomNSBH` from `PhenomDNRT`, and the bottom panel the maximum distinguishable SNR between `PhenomNSBH` and the two other models. Distinguishable SNRs below 10 are displayed as pink upside-down triangles and as blue triangles for SNRs above 100. The AZDHP noise curve is used to compute these results.

required), while the NS and BH (aligned) spins are uniformly sampled in the intervals $[-0.05, 0.05]$ and $[-0.5, 0.5]$, respectively. Finally, the NS dimensionless tidal deformability parameter Λ is uniformly sampled in $[0, 3000]$. The results are collected in Fig. 2.4. The top (middle) panel shows the distinguishability SNR values yielded by `PhenomNSBH` and its BBH limit (`PhenomDNRT`), while the bottom panel displays the maximum distinguishable SNR between `PhenomNSBH` and the two other models. It can be seen that the general trend described by Fig. 2.3 holds. In particular the characteristic SNR minimum at which the most distinguishable waveform model transitions between `PhenomDNRT` and the BBH limit persists across parameter space, widening and deepening as tidal deformability increases.

When considering this transition over the entire parameter space for the model, a minimum distinguishable SNR of 12 is found. Constraining $1.35M_\odot < M_{\rm NS} < 1.4M_\odot$, a minimum distinguishable SNR of 22 is found, and similarly constraining $\Lambda < 1000$ produces a minimum distinguishable SNR of 19. However, applying both cuts in NS mass and Λ increases the minimum distinguishable SNR to 48, indicating that the best chance of distinguishing an NSBH signal with current models is from a system with an exceptionally heavy NS or a particularly stiff EOS. It is in this region of relatively low distinguishable SNR that the NSBH model could be most useful. Assuming a single-detector SNR detection threshold of 10, a minimum distinguishable SNR of ~ 20 for an optimally-oriented binary system with fixed intrinsic parameters corresponds to a decrease in the distinguishable volume by a factor of ~ 8 compared to the detectable volume, and thus roughly one in every eight NSBH detections of this type could be distinguished from either a BBH or BNS signal.

If a signal were to be detected with $\mathrm{SNR} > 60$, comparisons with available NR waveforms suggest that systematic errors in the modelling would enter the waveform and would potentially bias any results inferred from using these models. While there is no anticipation of signals with such a high SNR to be seen until third-generation detectors [224, 152, 11] begin operation, should such a signal be detected, more accurate NSBH models will be required and potentially more accurate NR simulations of NSBH systems [131]. However, it has been shown in this chapter that for typical observations either BNS or BBH waveform models are expected to be sufficient.

2.4 Discussion

In this chapter the construction of `PhenomNSBH` has been outlined, an updated waveform model specific to signals from NSBH systems. This model uses an improved amplitude model that identifies distinct merger morphologies and a new tidal phase model, both of which have been calibrated using NR data. The model is valid for systems with mass-ratios ranging from $q \in [1, 15]$ with NS masses between $M_{\rm NS} \in [1, 3]M_\odot$, BH spins aligned with the orbital angular momentum ranging between $\chi \leq |0.5|$, and NS tidal deformabilities between $\Lambda \in [0, 5000]$. In addition, the model described here performs well when compared against available NSBH NR waveforms with spinning neutron stars, despite the amplitude model lacking such systems in its calibration.

It has been shown in Figs. 2.3 and 2.4 that the NSBH-specific characteristics of `PhenomNSBH` are distinguishable from other waveform models in different regions of parameter space. As the merger transitions to the non-disruptive regime, the amplitude of the waveform deviates further from a BBH waveform amplitude, which will be distinguishable in ground-based detectors for moderately loud signals. As the merger type becomes less disruptive, the NSBH waveform will easily be distinguishable from a BNS waveform model (*e.g.*, `PhenomDNRT`) due to the taper at high frequency applied to the latter and lack of ringdown in the signal. The important conclusion to draw from these results is that for signals below an SNR of 50, there is only a small region of parameter space where it may be possible to unambiguously identify an NSBH system. This statement is limited to single observations, and to aligned-spin models that include only the dominant waveform harmonic.

The waveform model `PhenomNSBH` described in this chapter is an improvement/extension of current NSBH waveform models, but there is certainly room for future advances. While recent cosmological simulations predict that the majority of NSBH systems will have relatively low mass-ratios ($q \sim [3, 5]$) [192], even at these low mass-ratios the effects of higher modes [272, 162] and precession [52, 51, 167] are vital to capture the essential physics from the waveform and should be a primary focus of future NSBH waveform modelling efforts. Another avenue for improvement lies in calibrating the phase model against NSBH NR waveforms. These tasks will require a large catalog of new NR simulations at high resolution and spanning a large range of mass-ratios, spins, and tidal deformability.

Chapter 3

Systematic coverage of a precessing space with numerical relativity simulations

3.1 Introduction

Many decades of research to solve the problem of solving Einstein's equations for the inspiral, merger and ringdown of two black holes was summarised in Sec. 1.5. Data generated by numerical relativity simulations has been critical to the development of gravitational waveform models that have enabled the direct detection and parameter estimation of gravitational waves over the last four years [19].

The families of models used to analyse data collected during the first and second observing runs of the advanced gravitational-wave detector network were the Phenom and EOB model families discussed in Sec. 1.6. The non-precessing model `PhenomD` [159, 164] directly benefited from better quality numerical relativity data that covered a larger parameter space than previously explored. As a result of `PhenomD` many other phenomenological models have indirectly benefited from numerical relativity data [186, 163, 165]. This also includes `PhenomNSBH` that was developed in Chapter 2. The spinning effective one body family of waveforms [100, 211] have also benefited from improved data sets as they are a carefully crafted synthesis of theory and calibration to numerical relativity. To complement the phenomenological approach to waveform modelling data driven strategies have enabled the first precessing waveform models that are calibrated to precessing waveforms [273]. These methods completely depend on the quantity and quality of numerical relativity data. Fits have also been made to the remnant properties of final mass and spin [161, 282].

Numerical relativity has been useful beyond modelling. NR waveform injections have been used in several studies, including to assess the presence of systematic bias in waveform models [10, 227], and to estimate intermediate mass black hole binary merger rates [22]. NR waveforms have also been used for direct comparisons and parameter estimation of GW observations [7, 175].

Phenomenological modelling has always benefited from NR simulations that systematically cover the desired parameter space domain. `IMRPhenomD` was supported by a nearly uniform covering of the $(\eta, \hat{\chi})$ aligned spin parameter space with 19 NR simulations. Several large catalogues of BBH NR simulations have been released [160, 147, 78]. While these do include some precessing configurations, the majority of these have mass ratios $q \leqslant 4$ and dimensionless spin magnitudes $\chi \leqslant 0.4$. There exists no broad systematic covering of the precessing parameter space with NR simulations.

In this chapter the first public catalogue of numerical relativity simulations for BBH systems from The Cardiff University Gravity Exploration Institute is introduced. This catalogue contains data sets from 40 different configurations of precessing black-hole binary systems. This catalogue contains data sets for four mass ratios $q = m_2/m_1 \in \{1, 2, 4, 8\}$ at two different spin magnitudes $a_2 = |\vec{S}_2|/m_2^2 \in \{0.4, 0.8\}$ each at five different spin vectors such that the angle between the newtonian orbital angular momentum and spin vector of the larger black hole is one of $\{30^\circ, 60^\circ, 90^\circ, 120^\circ, 150^\circ\}$. The material presented in this chapter is planned to be included as part of a larger publication that is currently in preparation [120] and will include further details and analysis of this catalogue.

The primary objective of this catalogue is to support the development of new precessing phenomenological models that are calibrated to numerical relativity waveforms. Secondary objectives are to contribute data that is useful to the waveform modelling community and to provide processed data sets that are appropriate for parameter estimation studies [10, 22].

In the following section is a description of the methods used by the BAM code [84, 157] to perform numerical simulations of BBH systems and the workflow that is used to produce low eccentricity initial data. In Sec. 3.3 an analysis of the data sets within the catalogue will be presented, including a summary of the different configurations of BBH systems for which data sets were produced, and a description of accuracy tests performed to validate the catalogue. Sec. 3.4 will conclude with a discussion of how this catalogue can be used to contribute to the continuing advance of gravitational wave data analysis and what regions of parameter space are still to be explored beyond this catalogue.

3.2 Summary of Methods

The simulations in this catalogue were produced using BAM [83, 84, 157], an adaptive mesh refinement numerical relativity code, evolving initial data via the moving-puncture method. A summary of the initial value problem, methods, and algorithms used by BAM were presented in Sec. 1.5. In this section the particular strategies for initial data construction and grid configurations for BAM used to produce the simulations in this catalogue will be presented.

3.2.1 Initial data construction

The aim for this catalogue was to generate single-spin precessing NR waveforms. These are required to start at a user set reference orbital frequency $M\omega_{\rm orb}$ and a user specified spin vector $\boldsymbol{S} \equiv \boldsymbol{S}_2$ at $M\omega_{\rm orb}$ on the larger secondary component black hole. The orientation of $\boldsymbol{S}_2$ can be defined by the angle $\theta = \arccos(\hat{\boldsymbol{L}}_{\rm N} \cdot \hat{\boldsymbol{S}}_2)$ between the spin vector $\boldsymbol{S}_2$ and Newtonian orbital angular momentum vector $\boldsymbol{L}_{\rm N}$, and the angle $\phi = \arccos(\hat{\boldsymbol{r}} \cdot \hat{\boldsymbol{S}}_{2\perp})$ between the projection of the spin vector on to the orbital plane $\boldsymbol{S}_{2\perp}$ and the separation vector $\boldsymbol{r}$ from the larger component black hole to the smaller component black hole.

The initial data generated for NR simulations in previous studies [141, 240, 159] specify the physical parameters of the system $(q, \boldsymbol{S}_1, \boldsymbol{S}_2)$ at a much larger separation $D_{\rm start}$ than the NR simulations will start at. EOB equations of motion are then evolved up to $M\omega_{\rm orb}$ and the parameters of the system are then read off at this frequency. These parameters are then used as input for an initial data solver to generate the initial data required for a BAM simulation as described in Sec. 1.5. The initial EOB simulation is performed to find parameters at $M\omega_{\rm orb}$ that describe a BBH system with as low an eccentricity as possible.

The EOB equations of motion used by [159] are also used in this work. However the method of [159] does not allow the user to specify the exact system configuration $(q, \boldsymbol{S}_1, \boldsymbol{S}_2)$ at $M\omega_{\rm orb}$. For precessing systems during inspiral, the spin vectors oscillate about a mean value θ and the rate of precession of the spin vectors increases as the system nears merger (see Fig. 3 and Fig. 4 in [242]). Due to this behaviour, an iterative brute force algorithm is used for this work. A sequence of input parameter sets

$$\boldsymbol{\theta}_i \equiv \left(q_i^D, \boldsymbol{S}_{1,i}^D, \boldsymbol{S}_{2,i}^D\right) = \left(q, \boldsymbol{0}, S_2\hat{\boldsymbol{t}}\right), \tag{3.1}$$

specified at $D_{\rm start}$ are used as initial conditions for the EOB solver. Each successive set of parameters are chosen based on the EOB evolution of previous parameter sets in the sequence. This is repeated until the EOB evolution results in the required parameters $(q, \boldsymbol{S}_1, \boldsymbol{S}_2)$ at $M\omega_{\rm orb}$ using the following algorithm.

The EOB simulations are started with both component black holes placed on the x-axis and the orbital angular momentum parallel to the z-axis. Further during the course of inspiral from $D_{\rm start}$ to $M\omega_{\rm orb}$ for the single-spin precessing systems in this catalogue, the angle θ can be seen to vary no more than $\sim 1^\circ$. As such for the brute force algorithm used in this work, once θ is specified, it is not iterated over. This means that the expression for $\hat{\boldsymbol{t}}$ may be written simply as,

$$\hat{\boldsymbol{t}} = \big(\cos(\phi)\cos(\theta), \sin(\phi)\cos(\theta), \cos(\theta)\big) \tag{3.2}$$

reducing the algorithm to an iteration only on the azimuthal spin angle ϕ. The initial separation $D_{\rm start}$ between the black holes at the start of the EOB evolution is user specified. For this work the black holes are placed $\sim 40M$ apart. The algorithm works according to the following steps,

(1) Initial candidate parameters at D_{start} ($n = 0$)
ϕ_0 is chosen to be the target azimuthal spin angle ϕ. The EOB solver is then run until $M\omega_{\rm orb}$ is reached and the azimuthal spin angle at that time is recorded as $\phi_{\omega,0}$. The EOB spin dynamics are explored in the region around $M\omega_{\rm orb}$ to find the closest time when the spin angle is equal to ϕ. The difference in frequency $\Delta M\omega_0$ between this time and $M\omega_{\rm orb}$ is recorded. If $|\Delta M\omega_0| \leqslant M\omega_{\rm tol}$ where $M\omega_{\rm tol}$ is a user specified tolerance then the algorithm stops. For the initial data generated in this work the percentage error tolerance of the orbital frequency is specified to be $M\omega_{\rm tol} = 1\%$. If $|\Delta M\omega_0| > M\omega_{\rm tol}$ then proceed to the next step.

(2) Second candidate parameters at D_{start} ($n = 1$)
ϕ_1 is chosen to be the difference between the target azimuthal spin angle and the azimuthal spin angle of the EOB spin dynamics at $M\omega_{\rm orb}$, given by $\phi_c \equiv \phi - \phi_{\omega,0}$. The EOB spin dynamics are explored again, recording $\phi_{\omega,1}$ at $M\omega_{\rm orb}$, and calculating $|\Delta M\omega_1|$ as in the same way as $|\Delta M\omega_0|$ in the previous step. If $|\Delta M\omega_1| \leqslant M\omega_{\rm tol}$ the algorithm stops otherwise proceed to the next step.

(3) Third candidate parameters at D_{start} ($n = 2$)
Let $\Delta\phi$ be 10° if $||\Delta M\omega_1| - M\omega_{\rm tol}| > M\omega_{\rm tol}/2$ otherwise let $\Delta\phi$ be 5°. ϕ_2 is chosen to be the target azimuthal spin angle $\phi_c + \Delta\phi$. $\phi_{\omega,2}$ and $|\Delta M\omega_2|$ are calculated in the same way as previous steps. If $|\Delta M\omega_2| \leqslant M\omega_{\rm tol}$ the algorithm stops otherwise proceed to the next step.

(4) Further candidate parameters at D_{start} ($n > 2$)
Let $\Delta\phi$ be 10° if $||\Delta M\omega_{n-1}| - M\omega_{\rm tol}| > M\omega_{\rm tol}/2$ otherwise let $\Delta\phi$ be 5°. If $\phi_{\omega,2} > \phi_{\omega,1}$ this indicates that the azimuthal spin angle is being rotated in the wrong direction. As such if $\phi_{\omega,2} > \phi_{\omega,1}$ then let $\phi_n = \phi_c + (2-n)\Delta\phi$ otherwise let $\phi_n = \phi_c + (n-1)\Delta\phi$. $|\Delta M\omega_n|$ is calculated in the same way as previous steps. If $|\Delta M\omega_n| \leqslant M\omega_{\rm tol}$ the algorithm stops otherwise repeat this step until this inequality is satisfied.

Once the required tolerance is met and the algorithm stops, the position, linear momentum and spin of each black hole are taken from the EOB dynamics at $M\omega_{\rm orb}$ and used as input for the NR initial data solver. For all the NR configurations described in this work the azimuthal angle for the spin vector $\mathbf{S}_2$ placed on the larger secondary component black hole was chosen to be $\phi = 0^\circ$.

3.2.2 Finite difference grid configurations

The finite difference scheme that BAM uses to evolve the initial data was described in Sec. 1.5 and requires an initial set of nested cartesian grids to be defined. For the NR simulations presented in this work there are several requirements that have been chosen to impose on the initial grid configurations. These are heuristic rules based on experience with the accuracy requirements of previous simulations.

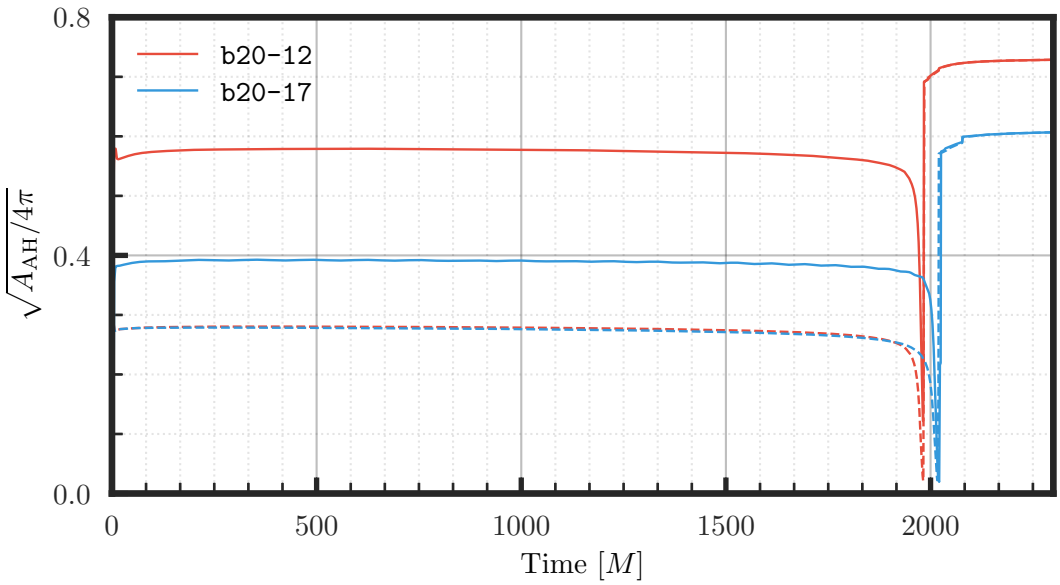

Figure 3.1: Visualization of the evolution of the *effective radius* of the apparent horizon for each black hole for two BAM simulations. The red lines are for simulation `b20-12` with initial parameters $(q, \chi_2, \theta) = (2, 0.4, 60°)$ and the blue lines are for simulation `b20-17` with initial parameters $(q, \chi_2, \theta) = (2, 0.8, 60°)$. The solid lines are for the higher mass BHs and the dashed lines are for the lower mass BHs. The variation in the effective radius are small during inspiral. The effective radius for the heavier BH peaks at $613.92M$ for `b20-12` with a radius of 0.58 and peaks at $350.90M$ for `b20-17` with a radius of 0.39.

The first requirement is that the smallest moving box following each component black hole should be 1.2 to 1.5 times the maximum effective radius of the apparent horizon of their respective black hole before merger. The apparent horizon radius of each black hole varies by a small amount before merger. Examples of how this radius evolves over time are presented in Fig. 3.1. Typically the maximum apparent horizon radius before merger is estimated from apparent horizon time series for a lower resolution simulation of the same configuration. However if no simulation has ever been performed with the same configuration then data from a simulation with a similar configuration is used. Following the notation from Sec. 1.5.2, this requirement is approached by changing the values of the grid spacing h_L on the finest level, and the level M at which the grids are created for the larger black hole. While the number of grid points N_L on the finest level also affects the size of the smallest moving boxes following each black hole, this is typically pre-determined and as such is not varied to meet this requirements.

The second requirement is to have at least ten grid points per wavelength of the $(4, 4)$ strain moment on the level that GWs are extracted on as described in Sec. 1.5.4, which is typically the first non-moving box level N. It is not normally possible to know the smallest GW wavelength or equivalently the maximum GW frequency of a simulation before the simulation is started. Instead the maximum frequency is estimated from the ringdown frequency model used by `PhenomD` [159, 164]. For `PhenomD`, models for the final mass and spin were constructed from which the ringdown frequency can be calculated using results from BH

perturbation theory. This PhenomD ringdown model is for aligned spin systems and takes as input mass ratio q and dimensionless aligned spin parameters χ_i which means that it is only an approximation to the ringdown frequency of the precessing configurations in this work. The ringdown frequency $f_{\rm RD}$ is approximated using the parameters $(q, 0, S_2\cos(\theta)/m_2^2)$. The required grid spacing on level n where GW are extracted is then approximated with $h_n = 1/(20 f_{\rm RD})$. This method could be improved by adding the in-plane spin component to the final spin as is done for PhenomP [143, 242]. However conservative choices were made for all grid configurations and so this was not necessary for these simulations. This requirement is approached by changing the values of the finest grid spacing h_L. If this requirement cannot be satisfied on level n and level n is not the last fixed box level, then the number of grid points N_{n+1} on level $n+1$ is increased until the box size $N_{n+1} \times h_{n+1}$ is large enough to support GW extraction at the radius required.

For most configurations both of these requirements can be satisfied. However it is not always possible to satisfy both requirements, and for such cases the smallest box sizes and extraction level grid spacing are balanced to achieve the best possible result.

3.2.3 Manual momentum perturbation

While the parameters derived from the EOB evolution described in Sec. 3.2.1 will lead to low eccentricity simulations, in general this will not be low enough to meet the requirements of the simulations in this work. A standard method to further reduce eccentricity is to make small perturbations to the momenta of the component black holes [141, 225]. For most of the simulations in this work a perturbation of 0.1-0.8% is applied to the magnitude of the momenta. This is normally sufficient to reduce the eccentricity below the desired threshold. However in cases where this is not sufficient the radial component of the momenta is also reduced by 25-75%.

For each candidate set of parameters $(q, \boldsymbol{S}_1, \boldsymbol{S}_2, \boldsymbol{p}_1, \boldsymbol{p}_2)$ a low resolution exploratory *eccentricity reduction* simulation with $N_L = 80$ is performed for $\sim 1000M$ of simulation time. When the eccentricity is low enough then these parameters are used for a *production* simulation, increasing N_L to 96 or higher. For the eccentricity reduction runs the grid requirements described in Sec. 3.2.2 try to be satisfied but it is not strictly enforced. For production simulations it is typically easier to satisfy grid requirements as the grid spacing h_L is reduced while effectively keeping the same moving box sizes on the finest grid levels.

There are two different ways that eccentricity is estimated for the simulations in this work. For eccentricity reduction runs where the merger time is not known the moving puncture separation D is fitted using a quadratic function with data in the range $[200, 700]M$ similar to the method described in [158]. The eccentricity is then estimated by the maximum absolute relative error between the fit and the data. For the production simulations the eccentricity is also estimated using the full method described in [158] which incorporates the merger time of the simulation.

Even when the production simulation's eccentricity is estimated using the same method

and same length of data as a lower resolution eccentricity run with the same configuration, there is no guarantee that the eccentricities will be the same. The eccentricity of a production simulation can go up or down due to changes in numerical accuracy, and for a few of the cases in this work the eccentricity of the production simulation does exceed the desired threshold. While not ideal the level of eccentricity in all production simulations is considered to be sufficiently low and eccentricity estimates using merger and non-merger methods are presented in Table 3.1.

3.3 Analysis of simulations

3.3.1 Description of simulation configurations

The catalogue consists of 40 simulations performed using BAM. For each simulation two mass parameters M_1, M_2 are provided, one for each black hole, the sum of these is chosen to equal 1. The initial data are iteratively constructed from these parameters such that the ADM mass of each puncture equals its respective mass parameter to within 0.02% [84]. At subsequent times the masses of each black hole are recorded as the apparent-horizon masses $M_{\rm AH,1}, M_{\rm AH,2}$ of each puncture which are related to the black hole hole masses M_1, M_2 through the Christodoulou formula [96, 97] as described in Sec. 1.5. 10 simulations at each mass ratio $q = M_2/M_1 \in \{1, 2, 4, 8\}$ are performed.

For each simulation a dimensional spin vector $\boldsymbol{S}_2$ is specified for the larger black hole, with the smaller black hole given a spin of zero $\vec{S}_1 \equiv \vec{0}$. Following the methods described in Sec. 3.2 10 different spin configurations are simulated at each mass ratio, $|\boldsymbol{S}_2| \in \{0.4, 0.8\}$ and $\theta = \arccos(\hat{\boldsymbol{L}}_{\rm N} \cdot \hat{\boldsymbol{S}}_2) \in \{30^\circ, 60^\circ, 90^\circ, 120^\circ, 150^\circ\}$ which are are achieved to within 1°.

The numerical phase error accumulates as the simulation is evolved. This can be reduced by increasing the resolution of a simulation at the cost of simulation speed. For this catalogue a soft requirement is imposed that a simulation should merge by $\sim 2000M$ in code time. Based on previous experience with simulations up to mass ratios $q = 18$, many of which were used in the development of the `PhenomD`, it is expected that 96-point simulations will have an acceptable level of accuracy if the merger time is less than $\sim 2000\,M$. It was originally intended to start all simulations at the same frequency, such that they would all have the same starting point in the frequency domain, where models are constructed. However, for some high mass ratio cases with a large aligned spin component, the spin-orbit hang-up effect causes the merger time to be well in excess of 2000M, and so a higher starting frequency has to be chosen.

To meet the soft requirement of simulation merger by $2000M$ the merger time is estimated using the LALSimulation [180] implementation of `PhenomD` [164]. This provides a utility function `XLALSimIMRPhenomDChirpTime` that calculates the time until the peak in the (2,2)-strain of a specific system configuration given a starting gravitational wave frequency which is used as a proxy for twice the orbital frequency. The starting frequency is optimized

Name	q	S_2/m_2^2	$\arccos(\hat{\boldsymbol{L}}_{\rm N}\cdot\hat{\boldsymbol{S}}_2)$	$\chi_{\rm eff}$	χ_p	D/M	$e\ (\times 10^{-3})$	$M\omega_{\rm orb}$	$N_{\rm orb}$
b20-1	1	0.400 (0.400)	30.004 (29.924)	0.173 (0.174)	0.200 (0.200)	11.573 (11.338)	1.547	0.023	10.001
b20-2	1	0.400 (0.400)	60.007 (59.851)	0.100 (0.101)	0.346 (0.346)	11.569 (11.340)	2.318	0.023	9.706
b20-3	1	0.400 (0.400)	90.041 (89.832)	-0.000 (0.001)	0.400 (0.400)	11.510 (11.285)	4.034	0.023	9.091
b20-4	1	0.400 (0.400)	120.039 (119.837)	-0.100 (-0.099)	0.346 (0.347)	11.572 (11.330)	2.971	0.023	8.714
b20-5	1	0.400 (0.400)	150.013 (149.888)	-0.173 (-0.173)	0.200 (0.201)	11.619 (11.366)	2.356	0.023	8.451
b20-6	1	0.800 (0.801)	30.029 (29.845)	0.346 (0.347)	0.400 (0.399)	11.560 (11.311)	2.145	0.023	10.947
b20-7	1	0.800 (0.801)	60.041 (59.736)	0.200 (0.202)	0.693 (0.692)	11.617 (11.371)	2.041	0.023	10.281
b20-8	1	0.800 (0.801)	90.071 (89.690)	-0.000 (0.002)	0.800 (0.801)	11.571 (11.308)	2.070	0.023	9.098
b20-9	1	0.800 (0.801)	120.059 (119.668)	-0.200 (-0.198)	0.692 (0.696)	11.585 (11.309)	1.734	0.023	8.285
b20-10	1	0.800 (0.801)	150.049 (149.801)	-0.347 (-0.346)	0.399 (0.403)	11.566 (11.269)	1.148	0.023	7.596
b20-11	2	0.400 (0.400)	30.040 (29.921)	0.231 (0.231)	0.200 (0.200)	11.551 (11.381)	1.396	0.023	11.136
b20-12	2	0.400 (0.400)	60.089 (59.833)	0.133 (0.134)	0.347 (0.346)	11.632 (11.469)	1.832	0.023	10.783
b20-13	2	0.400 (0.400)	90.117 (89.809)	-0.001 (0.001)	0.400 (0.400)	11.630 (11.436)	1.298	0.023	9.922
b20-14	2	0.400 (0.400)	120.086 (119.815)	-0.134 (-0.133)	0.346 (0.347)	11.579 (11.395)	1.930	0.023	8.947
b20-15	2	0.400 (0.400)	150.063 (149.903)	-0.231 (-0.231)	0.200 (0.201)	11.634 (11.431)	1.501	0.023	8.501
b20-16	2	0.800 (0.802)	30.096 (29.880)	0.461 (0.463)	0.401 (0.399)	11.453 (11.223)	2.761	0.023	12.454
b20-17	2	0.800 (0.802)	60.149 (59.726)	0.265 (0.269)	0.694 (0.692)	11.472 (11.261)	1.989	0.023	11.433
b20-18	2	0.800 (0.802)	90.235 (89.712)	-0.002 (0.003)	0.800 (0.802)	11.571 (11.369)	2.798	0.023	10.093
b20-19	2	0.800 (0.802)	120.188 (119.676)	-0.268 (-0.264)	0.691 (0.696)	11.544 (11.288)	1.680	0.023	8.312
b20-20	2	0.800 (0.802)	150.135 (149.836)	-0.462 (-0.462)	0.398 (0.403)	11.626 (11.339)	1.369	0.023	7.227
b20-21	4	0.400 (0.400)	30.102 (30.069)	0.277 (0.277)	0.201 (0.201)	10.582 (10.553)	1.404	0.026	11.963
b20-22	4	0.400 (0.400)	60.179 (60.115)	0.159 (0.160)	0.347 (0.347)	10.742 (10.712)	1.239	0.025	11.204
b20-23	4	0.400 (0.400)	90.196 (90.057)	-0.001 (-0.000)	0.400 (0.400)	11.552 (11.545)	1.443	0.023	12.353
b20-24	4	0.400 (0.400)	120.176 (120.063)	-0.161 (-0.160)	0.346 (0.346)	11.570 (11.519)	1.439	0.023	10.958
b20-25	4	0.400 (0.400)	150.104 (150.049)	-0.277 (-0.277)	0.199 (0.200)	11.544 (11.463)	2.033	0.023	9.810
b20-26	4	0.800 (0.801)	30.192 (30.144)	0.553 (0.554)	0.402 (0.402)	10.104 (10.027)	1.350	0.027	13.245
b20-27	4	0.800 (0.802)	60.354 (60.256)	0.317 (0.318)	0.695 (0.696)	10.482 (10.376)	0.749	0.026	12.121
b20-28	4	0.800 (0.802)	90.397 (90.195)	-0.004 (-0.002)	0.800 (0.802)	11.487 (11.365)	1.755	0.023	12.329
b20-29	4	0.800 (0.802)	120.363 (120.185)	-0.324 (-0.323)	0.690 (0.693)	11.579 (11.461)	2.013	0.023	9.987
b20-30	4	0.800 (0.801)	150.213 (150.120)	-0.555 (-0.556)	0.397 (0.399)	11.640 (11.478)	1.162	0.023	8.153
b20-31	8	0.400 (0.400)	30.153 (29.866)	0.307 (0.309)	0.201 (0.199)	9.542 (9.670)	1.252	0.030	13.206
b20-32	8	0.400 (0.400)	60.266 (59.911)	0.176 (0.178)	0.347 (0.346)	9.689 (9.840)	2.109	0.029	12.265
b20-33	8	0.400 (0.400)	90.305 (90.026)	-0.002 (-0.000)	0.400 (0.400)	10.107 (10.210)	1.079	0.028	11.785
b20-34	8	0.400 (0.400)	120.261 (120.093)	-0.179 (-0.178)	0.345 (0.346)	10.476 (10.567)	1.342	0.026	11.143
b20-35	8	0.400 (0.400)	150.148 (150.074)	-0.308 (-0.308)	0.199 (0.200)	10.766 (10.847)	1.492	0.026	10.659
b20-36	8	0.800 (0.802)	30.305 (29.666)	0.614 (0.619)	0.404 (0.397)	8.964 (8.970)	1.010	0.032	15.870
b20-37	8	0.800 (0.801)	60.538 (59.418)	0.350 (0.362)	0.697 (0.690)	9.372 (9.362)	1.364	0.030	14.223
b20-38	8	0.800 (0.801)	90.620 (89.777)	-0.008 (0.003)	0.800 (0.801)	10.021 (10.005)	2.143	0.028	11.924
b20-39	8	0.800 (0.802)	120.513 (120.255)	-0.361 (-0.359)	0.689 (0.693)	10.879 (10.907)	2.753	0.025	11.113
b20-40	8	0.800 (0.802)	150.286 (150.199)	-0.618 (-0.618)	0.397 (0.398)	11.453 (11.426)	0.915	0.024	10.181

Table 3.1: Initial data parameters and relaxed properties of the precessing BBH configurations in this catalogue. The smaller black hole has no initial spin. The associated properties of the larger black hole are identified with a subscript 2. The spin magnitude S_2/m_2^2, the spin tilt angle $\arccos(\hat{\boldsymbol{L}}_{\rm N}\cdot\hat{\boldsymbol{S}}_2)$, the effective spins $\chi_{\rm eff}$ and χ_p and the separation D/M are derived from the initial conditions of the simulations and relaxed times given in brackets. The eccentricity e is estimated over the region $[200, 1000]M$ using the method described in [158]. The orbital frequency $M\omega_{\rm orb}$ is derived from the dynamics at relaxed times. The number of orbits $N_{\rm orb}$ is from calculated from the relaxed time that $M\omega_{\rm orb}$ is reported at until the peak in the $(2, 2)$ multipole moment of Ψ_4.

using a simple interval bisection procedure until the peak time is $\sim 2000M$. A lower bound on the orbital frequency is set at 0.0225. The average merger time for the simulations that required a higher starting orbital frequency was $2055.11M$, with a minimum of 1958.94, and a maximum of $2181.16M$. These were calculated based on the retarded times for when the moving punctures merged. While `XLALSimIMRPhenomDChirpTime` performed sufficiently well, overall it slightly under estimated the merger time.

The properties of each simulation are presented in Table 3.1. The dimensionless spin magnitude S_2/m_2^2, the spin angle $\arccos(\hat{\boldsymbol{L}}_{\rm N}\cdot\hat{\boldsymbol{S}}_2)$, the effective spin $\chi_{\rm eff}$ given by Eq. (1.52), the precession spin χ_p given by Eq. (1.53) which reduces to the magnitude of the dimensionless spin perpendicular to the orbital angular momentum $S_{2\perp}/m_2^2$ for the single spin cases presented in this chapter, and the separation D/M are given from the initial conditions of the simulations and at a *relaxed time* in brackets. The relaxed time is defined as

$$t_{\rm rel} = t_{\rm peak} + 2t_{\rm damp}, \tag{3.3}$$

$$t_{\rm damp} = \frac{2\pi m_2}{0.08215626528}, \tag{3.4}$$

where $t_{\rm peak}$ is the peak in the $(2,2)$ strain moment before $500M$, and $t_{\rm damp}$ is the damping period of the $(2,2,0)$ QNM of a black hole [68] with mass equal to the larger black hole and a dimensionless spin of 0.8. The eccentricity e is estimated over the region $[200,1000]M$ using the method described in [158]. The orbital frequency $M\omega_{\rm orb}$ is derived from the dynamics at a relaxed time. The number of orbits $N_{\rm orb}$ is from calculated from the relaxed time that $M\omega_{\rm orb}$ is reported at until the peak in the $(2,2)$ multipole moment of Ψ_4.

3.3.2 Waveform accuracy

In order to assess the accuracy of the data which comprise this catalogue a subset of three of the configurations described in Table 3.1 were studied. These three configurations are $\left(q, \boldsymbol{S}_2/m_2^2, \theta\right) \in \{(4, 0.4, 60), (4, 0.8, 120), (8, 0.4, 30)\}$. The set of simulations produced for the $(4, 0.4, 60)$ case were performed with a lower starting frequency to provide an assessment of the accumulation of the error throughout the simulation.

The two main sources of error in the waveforms are the finite resolution of the simulation and the finite radius at which the waveform is extracted. In order to assess the effect of the finite resolution, a set of simulations with low, medium and high resolution were performed. These simulations had a resolution of $d = 0.0125$ (low resolution, 80-point run), $d = 0.0104$ (medium resolution, 96-point run) and $d = 0.00833$ (high resolution, 120-point run). The GW data were extracted at radii of $R_{\rm ext} \in \{50, 60, 70, 80, 90\}M$ which were all on the same refinement level for each simulation.

To test accuracy, in Sec. 3.3.2.1 power-weighted mismatches between waveforms with different resolutions and at different extraction radii are calculated to assess the magnitude of each of the two main sources of error. Mismatch accuracy is an important measure of waveform accuracy that is used in GW modelling and is a figure of merit used in Chapter 4

to explore NR accuracy requirements for third generation detectors.

3.3.2.1 Mismatches

For non-precessing (2,2)-mode only waveforms $h(\iota^h, \phi^h, t_c^h, \psi^h)$ and $g(\iota^g, \phi^g, t_c^g, \psi^g)$ there are many exact degeneracies between extrinsic parameters which leads to a simple definition of the match in Eq. (1.86) to quantify the agreement between them. However for precessing waveforms, like the ones produced in this catalogue, most of these degeneracies no longer exist and it is necessary to optimise and average over a larger set of extrinsic parameters to quantify the agreement between waveforms in a meaningful way. It is useful to identify the waveform h as the *template waveform* and the waveform g as the *signal waveform* however in the context of accessing NR accuracy both will be simulated waveforms.

For precessing waveforms the match is now defined as the maximisation of the noise-weighted inner product over the template extrinsic parameters (ϕ^h, t_c^h, ψ^h),

$$M(h,g)(\iota,\phi^g,\psi^g) = \max_{\phi^h,t_c^h,\psi^h} \left\langle \hat{h}(\iota,\phi^h,t_c^h,\psi^h) \,\middle|\, \hat{g}(\iota,\phi^g,\psi^g) \right\rangle . \tag{3.5}$$

The precessing match is then averaged over a discrete set of the signal phase and polarization (ϕ^g, ψ^g) weighted by the *optimal SNR* of the signal $\rho(\iota, \phi^g, \psi^g) = \|g(\iota, \phi^g, \psi^g)\|$ for each case called the *orientation-averaged-match*,

$$\overline{M}(h,g)(\iota) = \left(\frac{\sum_i \rho\left(\iota,\phi_i^g,\psi_i^g\right)^3 M(h,g)\left(\iota,\phi_i^g,\psi_i^g\right)^3}{\sum_i \rho\left(\iota,\phi_i^g,\psi_i^g\right)^3} \right)^{1/3} . \tag{3.6}$$

with an associated mismatch defined as $1 - \overline{M}$. For full details of the orientation-averaged-match please see [163]. This can then be evaluated for a set of inclination values ι.

The NR waveforms' lengths are constrained to prevent dephasing as described in Sec. 3.3.1. However this means that the lowest physical frequency that a simulation can reach for a low mass system is higher than 10Hz, which is the standard lowest frequency used for data analysis with current ground based detectors. While the match integral could be performed using a higher starting frequency, the full integral from 10Hz to the maximum NR frequency can be approximated using a *power-weighted mismatch* using the method described in [208]. This method takes into account the missing inspiral part of the waveform between 10Hz and the start of the NR waveform, and provides a more realistic measure of how accurate the NR waveforms are with respect to GW detectors.

To perform a power-weighted mismatch the constituent waveforms are first split up into contributions from NR defined over the frequency range $f \in [f_{\rm NR}, f_1]$ and the contributions from the inspiral below the lowest NR frequency defined over the frequency range $f \in [f_0, f_{\rm NR})$,

$$h(f) = \begin{cases} h_{\rm ins}, & f \in [f_0, f_{\rm NR}) \\ h_{\rm NR}, & f \in [f_{\rm NR}, f_1], \end{cases} \tag{3.7}$$

The power-weighted mismatch is then the mismatch in each region weighted by the fraction of power in each region,

$$\mathcal{M}_{\rm pow} \equiv \frac{\|h\|^2_{(f_0,f_{\rm NR})}}{\|h\|^2}\mathcal{M}_{\rm ins} + \frac{\|h\|^2_{(f_{\rm NR},f_1)}}{\|h\|^2}\mathcal{M}_{\rm NR}, \tag{3.8}$$

$$\|h\|^2 = \|h\|^2_{(f_0,f_{\rm NR})} + \|h\|^2_{(f_{\rm NR},f_1)}, \tag{3.9}$$

$$\mathcal{M}_{\rm ins} \equiv \mathcal{M}_{(f_0,f_{\rm NR})}(h_{\rm ins}, g_{\rm ins}), \tag{3.10}$$

$$\mathcal{M}_{\rm NR} \equiv \mathcal{M}_{(f_{\rm NR},f_1)}(h_{\rm NR}, g_{\rm NR}). \tag{3.11}$$

The inspiral parts are assumed to perfectly agree which means that $\mathcal{M}_{\rm ins}$ can be set to 0. This reduces the power-weighted mismatch to,

$$\mathcal{M}_{\rm pow} = \frac{\|h\|^2_{(f_{\rm NR},f_1)}}{\|h\|^2}\mathcal{M}_{\rm NR}. \tag{3.12}$$

It is important to make clear as described in [208] that $\mathcal{M}_{\rm pow}$ will be a lower bound to the mismatch $\mathcal{M} \geqslant \mathcal{M}_{\rm pow}$, however it is a sufficiently accurate approximation for NR accuracy assessment in this context.

Power-weighted mismatches were then performed for a range of total masses $M_{\rm total} \in [5, 200]M_\odot$ of the binary systems for a set of inclinations $\iota \in \{n\pi/6 \,|\, n \in [0, ..., 6]\}$. For these matches the inclination angle is equivalent to the polar angle θ provided to the spherical harmonics in composing a waveform from its modes. All waveforms are placed in a frame where the initial angular momentum $\boldsymbol{J}$ is aligned with the z-axis from which the polar angle extends. All noise-weighted inner products are evaluated over a frequency range starting from 10Hz up to a maximum frequency that includes all physical frequency content from the NR waveform. These were all performed using the Advanced LIGO, Zero Det, High Power simulated sensitivity curve [249]. `PhenomPv3` [163] is used as the inspiral approximant in the calculation for the optimal SNR $h_{\rm ins}$.

Fig. 3.2 presents the mismatch error between different finite resolution simulations of the same configuration at three different inclinations and also averaged over all inclinations. As can be seen from these figures, the mismatch increases for a system of lower total mass as more NR content appears between the match frequency bounds. However the mismatch also falls off rapidly at very low mass as most of the contribution to the mismatch here comes from the inspiral contribution by PhenomPv3. This mismatch is greater for waveforms at more extreme parts of the parameter space, $(8, 0.4, 30)$, and for longer simulations, $(4, 0.4, 60)$. The mismatch percentage error never exceeds 0.1% for any cases.

Fig. 3.3 presents the mismatch error between waveforms extracted and different radii of the same configuration again at an inclination of zero and also averaged over all inclinations. These exhibit similar trends over the total mass range as the results between different resolutions. Like the matches between different resolutions, the mismatch percentage error never exceeds 0.1%.

The sequences of increasing resolution and increasing extraction radius do not show the

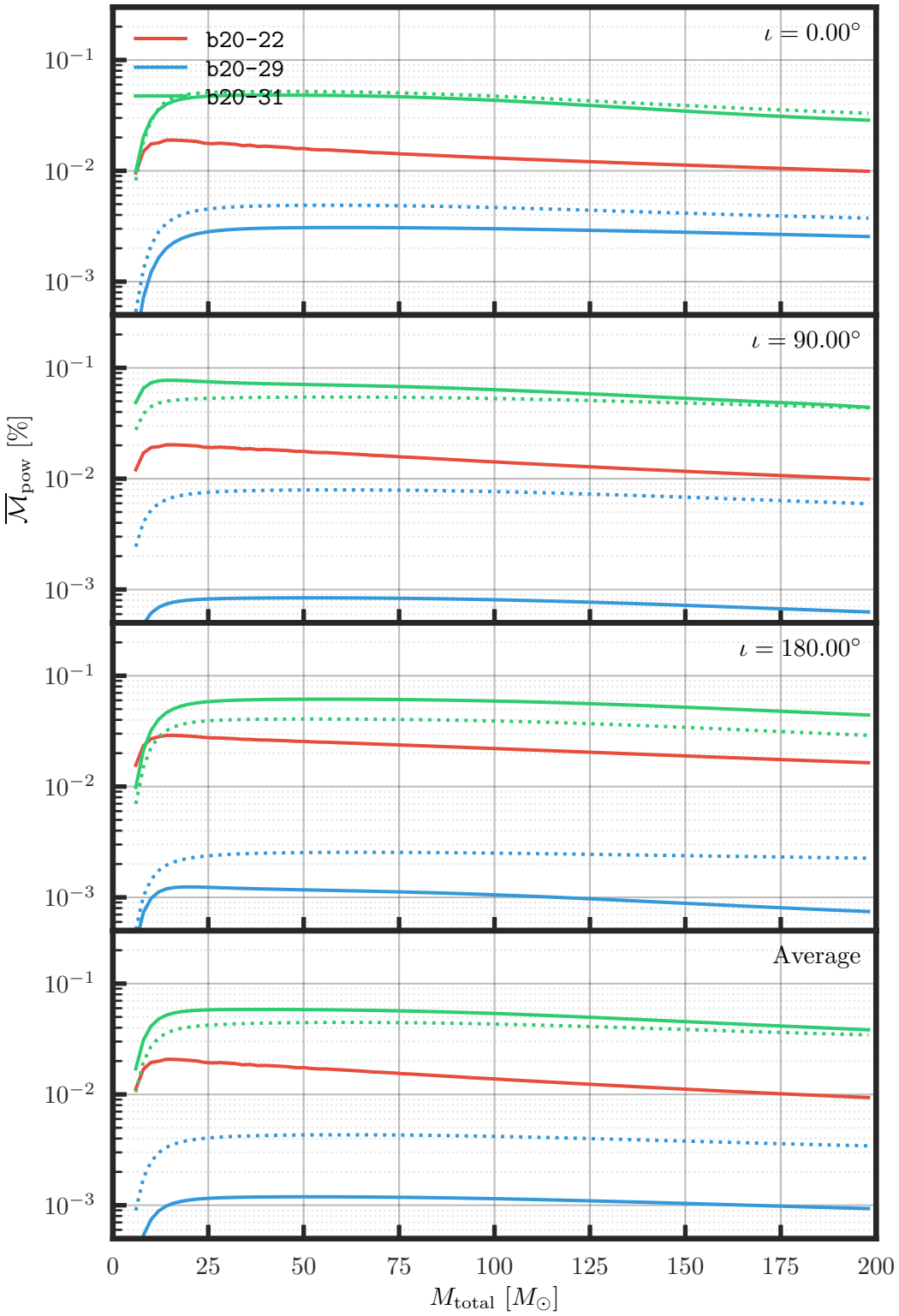

Figure 3.2: Comparison of the mismatch between simulations performed at different resolutions for 3 different configurations. The solid lines show the comparison between the high resolution 120-point simulations and the medium resolution 96-point simulations. The dashed lines show the comparison between the high resolution and low resolutions 80-point simulations. These simulations use data extracted at 90M on level $n = 7$.

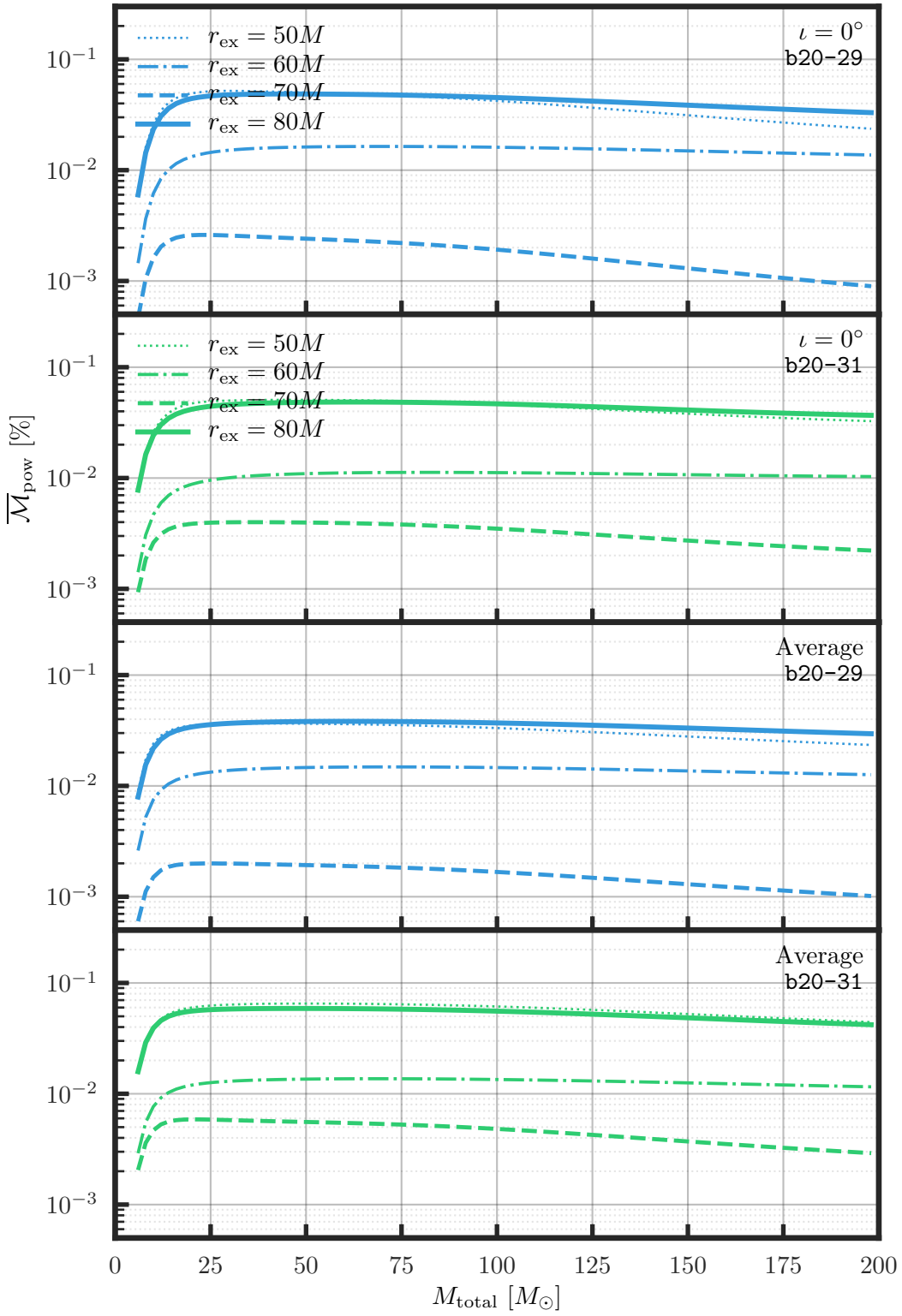

Figure 3.3: Comparison of the mismatch between waveforms extracted at different extraction radii $R_{\rm ext} \in \{50, 60, 70, 80\}M$ all on level $n = 7$. Each of the waveforms are compared against data extracted at an extraction radius of $R_{\rm ext} = 90M$. The waveforms compared were all extracted from the medium resolution 96-point simulations.

expected convergence relationships, which suggests that at least the lower resolution cases and data extracted at smaller extraction radii are not in the convergence regime. However a 1% mismatch percentage error is considered sufficient for applications within the advanced gravitational-wave detector network. As was the case for the BAM simulations performed for `PhenomD`, all cases have matches better than 99.9%, and as such the accuracy of these waveforms is considered more than sufficient for use with current generation detectors.

3.3.3 Catalogue comparison

Large and comprehensive catalogues of NR simulations of BBH systems have been produced by several research groups that span a growing region of the parameter space. The largest catalogue to date has been produced by the SXS collaboration with a total of 2018 numerical relativity waveforms [78] generated using the SpEC code [166]. The Georgia Tech group have released a single catalogue with 452 unique BBH waveforms from more than 600 BBH simulations [160] and the RIT group have released several catalogues amounting to a total of 320 simulations [147]. The properties of each of these catalogues are summarised in Table 3.2.

In Figs. 3.4 and 3.5, the parameter space coverage of the BAM and SXS catalogues is compared. Fig. 3.4 compares the distribution of configurations in each catalogue over the symmetric mass ratio η and the polar angle θ_2 of the spin vector on the larger black hole. This is done for two spin magnitudes $\chi_2 \geq 0.4$ and $\chi_2 \geq 0.8$. The SXS catalogue has good coverage for $\eta < 0.15$ and $\chi_2 < 0.8$ but is sparse in regions of the parameter space where $\chi_2 \geq 0.8$ and for low spin ($0.4 \leq \chi_2 < 0.8$) high mass ratio waveforms ($0.15 \leq \eta \leq 0.08$). Fig. 3.5 compares configuration distributions over the precessing effective-spin parameter χ_p and mass ratio q. The 90% credible contours of the marginalised two dimensional posterior distributions for the first three gravitational wave detections GW150914 [9], GW151012 [5], and GW151226 [8] are also shown. In all cases the BAM catalogue is able fill in the gaps where the SXS catalogue is sparse and in particular able to cover a large part of the parameter space that is consistent with the LIGO gravitational wave detections represented by the 90% credible contours.

The simulations in this catalogue probe high mass ratio, high spin regions of the parameter space that have previously been unexplored by existing numerical relativity codes. The 90% credible intervals of the current detections made with the advanced gravitational-wave detector network observatory extend up to $q = 8$ despite having most support at equal mass (see Fig. 4 in [19]) which motivates the continued exploration of a broad parameter space with NR. Given the support for high mass ratio events from current BBH population estimates and the expected ~ 50 gravitational wave detections in the third observing run, high mass ratio simulations are needed to build more reliable waveforms used in the parameter estimation analysis.

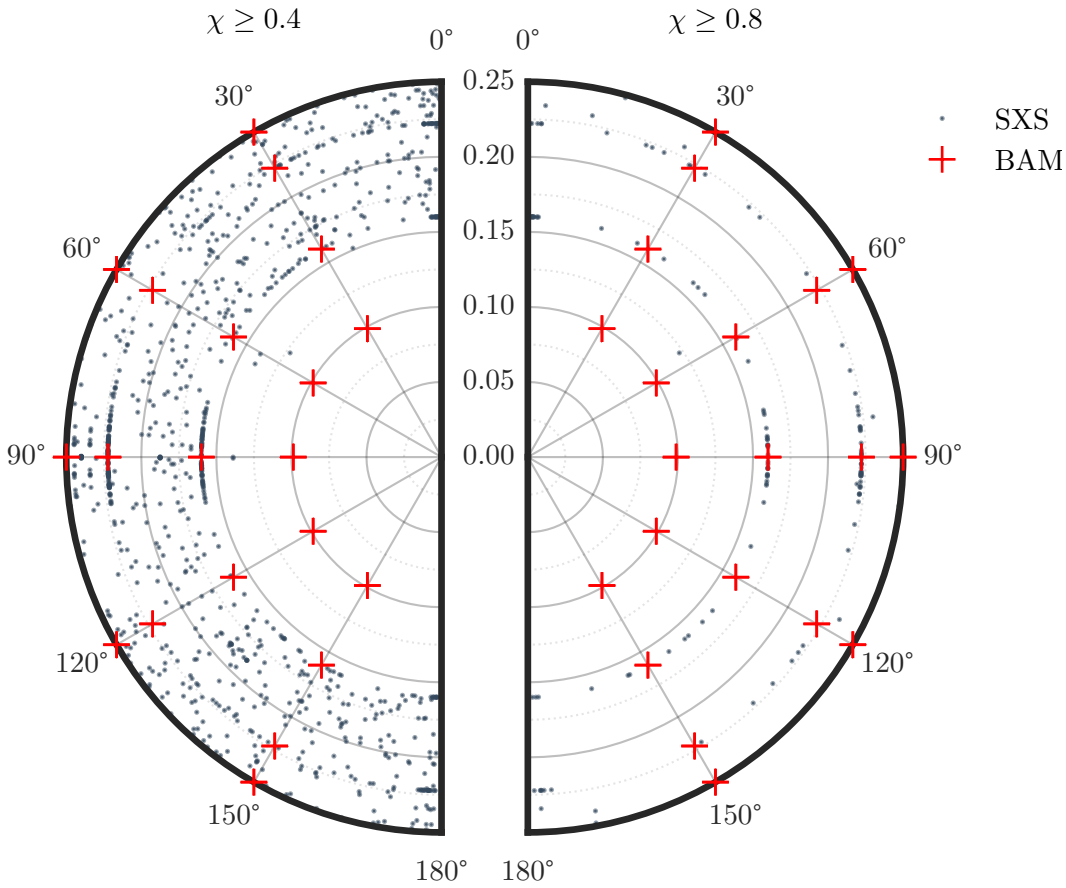

Figure 3.4: Comparison between the parameter space coverage of the SXS catalogue and the BAM catalogue. Polar plot with radius of the symmetric mass ratio, η, and orientation as the angle between $\boldsymbol{L}$ and $\boldsymbol{S}_2$, θ, for two different spin magnitudes, $\chi_2 \geq 0.4$ and $\chi_2 \geq 0.8$. The grey scatter plots represent the SXS catalogue and the red $+$ represents the BAM catalogue.

Catalog	Simulations	q range	χ_p range	χ_{eff} range
BAM	40	[1,8]	[0.2,0.8]	[-0.62,0.62]
Georgia Tech [160]	452	[1,15]	[0,0.8]	[-0.8, 0.8]
RIT (2019) [147]	320	[1,7]	[0,0.42]	[-0.95, 0.95]
SXS (2019) [78]	2018	[1,10]	[0,0.89]	[-0.97, 0.99]

Table 3.2: Table showing a comparison between 4 different numerical relativity catalogs. The effective precession parameter is defined as χ_p and the effective spin parameter is defined as χ_{eff}. The mass ratio, q, is defined $m_1/m_2 \geq 1 \forall m_1, m_2$ where m_1 is the primary mass and m_2 is the secondary mass of the BBH. The SXS (2019) and RIT (2019) rows correspond to the SXS and RIT waveforms made available in 2019.

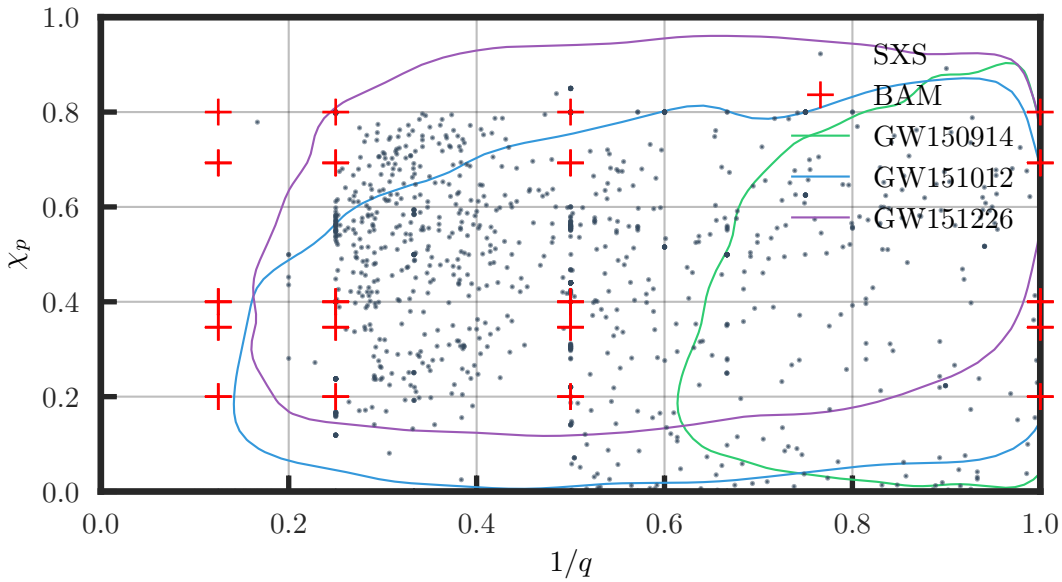

Figure 3.5: Comparison between the parameter space coverage of the SXS catalogue and the BAM catalogue. Plot with axes mass ratio and effective precession. The curves are the 90% contours for the 2 dimensional posterior probability for GW150914 (green), GW151012 (blue) and GW151226 (black) [9, 5, 8]. In both plots the grey scatter plots represent the SXS catalogue and the red + represents the BAM catalogue.

3.4 Discussion

In this chapter a new set of 40 NR simulations covering a very broad region of the precessing parameter space were presented. These are already being used in the development of the next generation of precessing phenomenological models, which will be calibrated to precessing NR simulations for the first time. This catalogue will be made available to the wider GW community where it will not just benefit GW models but also injection studies.

Most of the simulations contain a sufficient number of orbits for detection purposes [140, 208] with the average number of orbits across all simulations being 10.64 orbits. However several cases with nearly anti-aligned spin which complete somewhat fewer than 10 orbits and are good candidates for future simulations starting at larger separation. The high mass ratio cases with large aligned spin components, for which higher starting frequencies were used as described in Sec. 3.3.1, are *short* in their frequency range, and producing longer, accurate simulations for these cases may also be useful in the future.

The amount of effective spin in all configurations is constrained because only one black hole has spin. This is especially visible in the $q = 1$ and $q = 2$ simulations. Adding spin to the secondary black hole is another good candidate for future simulations, however it presents a great challenge of generating low eccentricity initial data with a systematic placement of simulations across the full two-spin parameter space. An important precursor question to this is to understand if certain regions of the two-spin parameter space are excluded by traditional formation channels of BBH systems.

The accuracy of these simulations is consistent with NR accuracy for previous GW

models [164, 186] and this catalogue will be a valuable resource for many years. However as will be discussed in Chapter 4, third generation ground based detectors will require significantly more accurate NR data. Advances in CPU power alone will not be sufficient and will require more innovation to meet these future demands.

Chapter 4

Distinguishability of PhenomD in future detectors

4.1 Introduction

Four years of operation of the advanced gravitational wave detector network [47, 3, 30, 31] has resulted in a wealth of data with 11 confirmed detections during the first (O1) and second (O2) observing runs. Over this time the detectors have been continually improved. The LIGO Hanford observatory (LHO) started O1 with an angle averaged BNS inspiral range of $\sim 80\,\mathrm{Mpc}$ and LIGO Livingston observatory (LLO) starting with $\sim 60\,\mathrm{Mpc}$. Now LHO operates at $\sim 110\,\mathrm{Mpc}$ and LLO $\sim 135\,\mathrm{Mpc}$, resulting in nearly an order of magnitude increase in sensitive volume [13].

In parallel to the improvements in the advanced detector network, great advances in GW models have also been made. Models available at the beginning of O1 included the $(2,2)$-mode only aligned spin models [164, 261], and quadrupole order precessing spin models [143, 242, 211] that were not calibrated to precessing NR data. Now waveform models include many more features such as higher order and sub-dominant modes [186, 100], advanced precession dynamics [163, 165], and even models that accurately represent smaller subsets of the full seven dimensional precessing parameter space [273].

Accurate waveform models have helped ensure the maximum amount of information could be extracted from the data generated by this generation of gravitational wave detectors. This new data has been an important addition to the data streams that contribute to inferred populations of BBHs [18], cosmology [14], and tests of fundamental physics [24]. Crucially, accurate waveform models are required for unbiased parameter estimation of candidate signals. Model accuracy in the context of parameter estimation (PE) will be the focus of this chapter.

There are two classes of error that contribute to PE, statistical errors and systematics errors. Statistical errors manifest because no signal is infinitely loud, which means that in the Bayesian framework of GW PE there are regions rather than single point of a model's parameter space that have a non-zero probability of being the true signal parameters. The

loudness of a signal is the SNR discussed in Sec. 1.7 and is related to the amount of statistical uncertainty. For sufficiently loud signals the SNR has a direct inversely proportional relationship with statistical error. Systematic errors are non-linear shifts in the statistical distributions. The main source of statistical error comes from a detectors sensitivity. Primary sources of systematic error are inaccuracies in waveform models, degeneracies between parameters, and observational biases. Systematic errors can also come from inaccuracies in detector modelling, however this source of error will not be considered in this chapter. Focusing on waveform models, when statistical errors are larger than systematic errors a waveform model is considered accurate enough.

It is important to understand what is a sufficient accuracy for a model given a particular detector. Improving the accuracy of models can come from improving the accuracy of input NR waveforms, and improving the accuracy or number of physical effects that a model includes. NR simulations are computationally expensive and may even require new numerical techniques. Improving or adding physical effects to a model is also never trivial. Knowing what is a sufficient accuracy for any given detector will help to best manage limited resources towards reaching accuracy goals.

Third generation (3G) detectors will provide a significant jump in detector sensitivity. This chapter will focus on BBH CBC events and consider the requirements that are needed for BBH GW models to ensure the same success with extracting results from 2G observational data continues for 3G observational data. As a consequence, requirements on numerical relativity data to satisfy the GW model requirements will also be explored.

Early work [127, 181, 195] helped established the form of an *indistinguishability criteria* that provided tools to answer the question of how accurate do waveform models need to be for detection and subsequent parameter estimation. For the purpose of parameter estimation these relate mismatches between two GW waveforms to expected SNRs beyond which these two waveforms can be *distinguished*. More recent work [59, 94] provided more complete criteria depending on parameter space dimensions. Several recent studies [139, 145] have used a form of the indistinguishability criteria to continue the analysis of this criteria and of waveform model accuracy requirements.

The indistinguishability criteria described in [59] typically underestimates the required SNR at which waveforms will become distinguishable. A naive application of this form of an indistinguishability criteria for the first detected GW event GW150914 [9] suggests that biased results might have been expected from parameter estimation using current GW models. However no evidence for systematic bias for this event has been found [10]. In general the different forms of indistinguishability criteria provide conservative lower bounds for distinguishable SNRs.

There are several reasons why this is the case. When considering one dimensional posteriors from parameter estimation the true parameters of a signal can appear within the 90% confidence interval of parameters of interest such as the component masses m_1 and m_2 but still lie outside of the 90% confidence region of the multidimensional posterior. Only by considering the posterior under appropriate transformations and 1D projection would this

be revealed.

Another issue is a result of incompatible function spaces of GW models. The function space of a GW model will in general not be the same as the true space of GW signals. This can manifest in different ways, but typically this will mean the effectual match or fitting factor is less than one. This means that there is a component of the true signal that cannot be reproduced by a model.

A recent study [227] considered the NR and GW modelling communities preparedness for 3G ground-based detectors and aimed to answer the same questions as this chapter. Their study was based on analysing two *golden binary* signals generated from two hybridized NR waveforms. Using current GW models including a precessing model they concluded that GW models will be needed that are at least three orders of magnitude more accurate, and NR waveforms that are one order of magnitude more accurate.

The complementary work of this chapter will aim to answer these same questions using a different approach. Instead of considering a waveform model that includes many features like precession that can result in mismatch calculations that are highly sensitive to parameter changes the (2,2)-only multipole moment model `IMRPhenomD` [164] will be considered. This will mean some of the extrinsic parameters such as inclination can be ignored that were noted to have a strong influence on their results. The analysis will also be performed using 16 NR datasets, each of which were used in the calibration of `IMRPhenomD`, and 2 NR datasets that were not used in calibration. This will ensure that the results depend on the best achievable accuracy of a GW model for particular configurations rather than highlighting regions of parameter space at which a GW model has not yet achieved its optimal accuracy due to lack of NR calibration.

Sec. 4.2 will review the current understanding of the indistinguishability criteria, present a method to address the question of accuracy requirements for waveforms in the 3G era through an injection study, and how the method will aim to mitigate as many sources of underestimation as possible. Sec. 4.3 will present the results of the injection study and provide a candidate strategy to meet the requirements for 3G. Finally Sec. 4.4 will address limitations of the method when applied to more complete waveform models that incorporate additional features such as higher modes and precession and candidate strategies to handle these effects.

4.2 Method

Given an SNR accuracy target, by how much does a GW model mismatch error need to improve to ensure they are indistinguishable from NR? By how much does NR mismatch error need to improve to facilitate this? These are the motivating questions for this chapter. Waveform model accuracy will be assessed using two methods. The first method will create NR injections and recover them with the waveform model and identify the SNR at which no parameter bias is observed, in other words the SNR at which the waveform model is indistinguishable from NR in parameter estimation. The second method will evaluate a

modified form of the indistinguishability criteria from [59] between the NR used for the injections and the waveform model.

The answer to the waveform accuracy question will depend at least partially on the waveform model used. For the analysis in this chapter the aligned spin, $(l, |m|) = (2, 2)$ model `PhenomD` is used. This has been the most accurate aligned spin Phenomenological model for many years, and a keystone in the Phenom family.

Several of the parameters required to describe a BBH, as previously introduced in Sec. 1.4, are partially degenerate with one another. This makes it impractical to infer general results about waveform accuracy from parameter estimation, and makes for an unfair comparison to other accuracy methods. The phenomenological and EOB model families are still making progress towards models that fully capture the waveform morphology induced by precessing CBC systems. Current approximate precessing models are effective for 2G detectors but make internal dimension reduction simplifications. It has only been recently in the surrogate models where fully precessing waveforms have been modelled. However the parameter space coverage is still smaller than the phenomenological and EOB families. By choosing to use an aligned spin analysis the effect of many partial degeneracies can be mitigated and those that remain are well understood in the aligned spin subspace. The expectation would then be that phenomenological models as accurate as `PhenomD` for aligned spin BBH systems can be developed for precessing systems, and the results for this work can be scaled to higher dimensions.

More recent waveform models have introduced features of multipole moments that are not $(l, |m|) = (2, 2)$. Similar to precession modelling these new multipole moments have not yet been modelled as completely as the $(l, |m|) = (2, 2)$ moments for broad parameter space models of aligned spin systems. By choosing to just analyse the $(l, |m|) = (2, 2)$ moments there is much more control over this study, and the results are less sensitive to small variations in model parameters.

The answers to both the waveform and NR accuracy questions will also depend on detector networks, individual detector locations and their sensitivity curves. To simplify this problem only single detector injections are performed. In combination with the choice of $(l, |m|) = (2, 2)$ aligned spin systems many of the parameters become completely degenerate with one another [237], for example the sky location and distance both parameterize waveform amplitude. This means that the parameter space can be reduced to just 7 non-degenerate parameters, two mass parameters m_1, m_2, two dimensionless aligned spins χ_1, χ_2, and three extrinsic parameters, luminosity distance $D_{\rm L}$, coalescence phase ϕ_c, and coalescence time t_c.

In the rest of Sec. 4.2 each of the components that composed this analysis will be described.

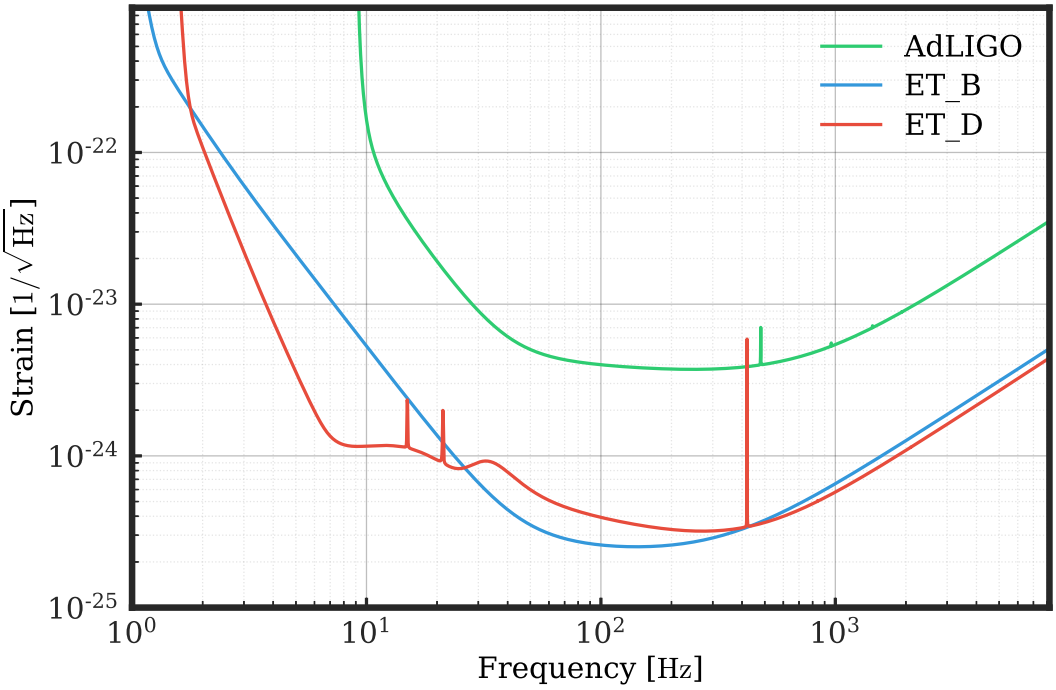

Figure 4.1: Sensitivity curves for Advanced LIGO at design sensitivity in green and Einstein Telescope with sensitivity option ET-B in blue and sensitivity option ET-D in red.

4.2.1 Third generation detectors

The main analysis is based on the sensitivity projections for the proposed 3G detector Einstein Telescope. Several candidate sensitivity options exist for Einstein Telescope. The analysis uses the ET-D sensitivity option [152] that is presented in Fig. 4.1. The Advanced LIGO design sensitivity curve [1] and ET-B sensitivity option [151] are also plotted for reference. The injection and parameter estimation analysis is performed using a single detector. As such the injections and recovery will be made with only a single pair of arms of the three proposed pairs in the ET triangle design.

The SNR distribution for high SNR events is proportional to $1/\rho^4$ [243]. Recent BBH merger event projections for Einstein Telescope with the ET-B sensitivity option suggest a point rate density of $R'_c = 10$ events at SNR $\rho_c = 100$ [58]. Using this information, given a maximum number of detected BBH merger events T that are permitted parameter estimation biases due to waveform accuracy, the SNR ρ_0 can be estimated such that the expected number of events with SNRs $[\rho_0, \infty]$ is equal to T using the follow expression

$$\rho_0 = \sqrt[3]{\frac{\rho_c^4 R'_c}{3T}}. \tag{4.1}$$

As an example, for maximum numbers of biased parameter estimations $T \in \{1, 10, 100\}$ gives critical SNRs of $(693, 321, 149)$ respectively. With expected detection rates of $\sim 10^5$ events per year these are equivalent to 0.0001%, 0.001%, and 0.01% of all detections per year will have biased estimations. The accuracy requirements placed on waveform models

and NR will depend on the choice of acceptable numbers of biased parameter estimations.

4.2.2 Review of PhenomD

In this work the aligned spin BBH frequency domain waveform model `PhenomD` [159, 164] will be used that models the $(l, |m|) = (2, 2)$ moments. `PhenomD` depends on four intrinsic parameters, the component masses m_1 and m_2 of each black hole, and the black holes' dimensionless aligned spins χ_1 and χ_2

$$\chi_i = \frac{\mathbf{S_i} \cdot \hat{\mathbf{L}}}{m_i^2}. \tag{4.2}$$

The various components of PhenomD depend on different combinations of dimensionless spin parameters,

$$\chi_{\rm eff} = \frac{m_1\chi_1 + m_2\chi_2}{m_1 + m_2}, \tag{4.3}$$

$$\chi_{\rm PN} = \chi_{\rm eff} - \frac{38\eta}{113}\left(\chi_1 + \chi_2\right), \tag{4.4}$$

$$\hat{\chi} = \frac{113\chi_{\rm PN}}{113 - 76\eta}. \tag{4.5}$$

Choosing an appropriate representation of the four dimensional parameter space in which to view the parameter estimation results is important and does affect the outcome of the analysis. Different representations of the 4D posterior data can be related by non-linear transformations. While under certain representations the posterior data is approximately gaussian, in others the posterior data are not. Approximately gaussian distributions are necessary for this analysis. For the spin subspace the dimensionless spins χ_1 and χ_2 are not recovered as Gaussian distributions. Any two of the dimensionless spin transformations Eqs. (4.3-4.5) solve this issue and so the posterior data is represented using spins $\chi_{\rm eff}$ and $\chi_{\rm PN}$.

4.2.3 Numerical relativity data

For this chapter the BBH configurations that correspond to the BAM NR simulations used to calibrate and test PhenomD [159, 164] are used. The black hole spins of all configurations are aligned with the orbital angular momentum of their binary system. The 16 NR simulations cover mass ratios $q \in \{2, 3, 4, 8, 10, 18\}$ and the component BHs have aligned spins within $\chi_i \in [-0.85, 0.8]$. 2 NR simulations that were not used in the calibration or testing of `PhenomD` are also used, $q \in \{8, 18\}$, $\chi_1 = 0.8$, and $\chi_2 = 0$. The analysis for these cases are separated by a horizontal line at the bottom of Tables 4.1 and 4.2.

NR accuracy is typically calculated as the mismatch error

$$\mathcal{M}(h_1, h_2) = 1 - M(h_1, h_2), \tag{4.6}$$

q	η	χ_1	χ_2	$\chi_{\rm eff}$	$\chi_{\rm PN}$	$\hat{\chi}$	$Mf_{\rm win,0}$	$Mf_{\rm win,1}$	$N_{\rm NR}$	$N_{\rm hyb}$
2	0.222	0.50	0.50	0.50	0.43	0.50	0.00706	0.00761	27.62	2231.14
2	0.222	0.75	0.75	0.75	0.64	0.75	0.00819	0.00909	24.34	2248.45
3	0.188	-0.50	-0.50	-0.50	-0.44	-0.50	0.00677	0.00737	20.76	2547.91
4	0.160	-0.75	-0.75	-0.75	-0.67	-0.75	0.00735	0.00812	16.50	2949.33
4	0.160	-0.50	-0.50	-0.50	-0.45	-0.50	0.00744	0.00811	18.94	2978.23
4	0.160	-0.25	-0.25	-0.25	-0.22	-0.25	0.00778	0.00851	19.72	3006.41
4	0.160	0.00	0.00	0.00	0.00	0.00	0.00802	0.00870	21.79	3034.10
4	0.160	0.25	0.25	0.25	0.22	0.25	0.00825	0.00900	23.70	3061.02
4	0.160	0.50	0.50	0.50	0.45	0.50	0.00841	0.00909	26.75	3087.47
4	0.160	0.75	0.75	0.75	0.67	0.75	0.00839	0.00902	30.61	3113.25
8	0.099	-0.85	-0.85	-0.85	-0.79	-0.85	0.01034	0.01466	8.13	4729.19
10	0.083	0.00	0.00	0.00	0.00	0.00	0.01231	0.01405	13.07	5837.92
18	0.050	-0.80	0.00	-0.76	-0.74	-0.77	0.00949	0.01025	14.52	9352.37
18	0.050	-0.40	0.00	-0.38	-0.37	-0.39	0.01089	0.01184	14.97	9505.41
18	0.050	0.00	0.00	0.00	0.00	0.00	0.01394	0.01567	12.50	9654.38
18	0.050	0.40	0.00	0.38	0.37	0.39	0.01368	0.01465	22.77	9801.50
8	0.099	0.80	0.00	0.71	0.68	0.73	0.01288	0.01419	23.03	5026.81
18	0.050	0.80	0.00	0.76	0.74	0.77	0.01814	0.01971	22.83	9944.96

Table 4.1: Metadata for all NR and hybrid waveforms used in this paper. $q = m_1/m_2$ and $\eta = q/(1+q)^2$ are the mass ratio and symmetric mass ratio. The spin parameters $(\chi_1, \chi_2, \chi_{\rm eff}, \chi_{\rm PN}, \hat{\chi})$ are the dimensionless spins defined by (4.3-4.5). The simulation frequencies $Mf_{\rm win,0}$ and $Mf_{\rm win,1}$ are the start and end frequencies used for the hybridization window. The cycle count $N_{\rm NR}$ is the number of gravitational wave cycles from the start of the NR component of the hybrid and $N_{\rm hyb}$ are the total number of gravitational wave cycles in the full hybrid waveform.

where the match M is given by Eq. 4.7 and h_1, h_2 are two NR simulations at different quality levels. For BAM different quality levels of simulation are distinguished by the number of points used for each dimension of the smallest nested simulation grid.

For the set of NR simulations used in this study, NR mismatch errors are calculated by [164] using the `AdLIGO` sensitivity curve. As only the cases $q = 4$, $\chi_1 = \chi_2 = 0.75$ and $q = 18$, $\chi_1 = \chi_2 = 0.0$ have mismatch error estimates, these are used as estimates for the mismatch error for all NR cases used in this study. For the 96^3 grid size simulations that are used here, the mismatch error for both simulations is bounded above by 10^{-3}. However this is for low total mass and does include non-trivial contributions from the inspiral part of the hybrid waveforms used to develop `PhenomD`. For a total mass of $200M$ that is less dependant on the non-NR inspiral the mismatch error drops to 10^{-4} for the $q = 4$ case and 5×10^{-4} for the $q = 8$ case. As such, for the total mass of $300M$ that is used for the injections in this chapter a reference average NR mismatch error of 10^{-4} will be used.

The attributes for all the cases used including derived spins given by Eqs. (4.3-4.5) and NR gravitational wave cycles are presented in Table 4.1.

4.2.4 Hybrid waveforms

In order to reduce the effect of the Gibbs-Wilbraham phenomenon [150] and to allow analysis at low total mass the NR waveforms used in this work are hybridized. The time domain waveform model `SEOBNRv4` [72] is used for the inspiral component of the hybrids. This model also depends on four intrinsic parameters $(m_1, m_2, \chi_1, \chi_2)$ like PhenomD. The hybridization procedure described in [87] and previously discussed in Sec. 1.6.4 is used in this chapter. The frequency range over which the inspiral `SEOBNRv4` waveform transitions to the NR waveform is bounded by the frequencies $Mf_{\rm win,0}$ and $Mf_{\rm win,1}$ given in Table 4.1. $Mf_{\rm win,0}$ was chosen for each waveform such that no residual noise was present at the start of the NR waveform, and $Mf_{\rm win,1}$ was chosen to be 3 GW cycles after $Mf_{\rm win,0}$.

4.2.5 Waveform match comparison

To compare waveforms the standard *match* $M(h_1, h_2)$ is defined, as previously introduced in Sec. 1.7.1, between two waveforms $h_1(t)$ and $h_2(t)$ given by [236]

$$M(h_1, h_2) = \max_{\Delta t, \Delta\phi} \left\langle \hat{h}_1(t - \Delta t) e^{i\Delta\phi} \middle| \hat{h}_2(t) \right\rangle, \tag{4.7}$$

$$\langle h_1 | h_2 \rangle = 4\mathrm{Re} \int_{f_{\rm min}}^{f_{\rm max}} \frac{\tilde{h}_1(f)\tilde{h}_2^*(f)}{S(f)} \mathrm{d}f, \tag{4.8}$$

$$\hat{h} = \frac{h}{\sqrt{\langle h | h \rangle}}, \tag{4.9}$$

where the standard *inner product* $\langle h_1 | h_2 \rangle$ given by [102] is expressed in terms of the Fourier transforms $\tilde{h}_1$ and $\tilde{h}_2$ of h_1 and h_2 and a chosen power spectral using the `ET-D` sensitivity option $f_{\rm min}$ is always chosen to be 5Hz and $f_{\rm max}$ is chosen to be 2048.

4.2.6 Parameter estimation strategy

For each NR configuration an injection is made using the associated hybrid waveform into zero noise. Each injection is made with a total mass of $M_{\rm total} = 300 M_\odot$ and at an SNR of $\rho = 250$. All injections are made into a single detector network composed of Einstein Telescope using the `ET-D` sensitivity option. The injections are made directly above the single detector with zero polarization. The binary systems are with zero inclination. While these extrinsic parameters do change the detector response, as described in Sec. 4.2 these are completely degenerate with luminosity and coalescence phase. As such they do not affect the results of the analysis.

The parameter estimation results produced for this chapter have been performed using the `dynesty` dynamic nested sampling package [256] as the engine for the Bayesian inference library Bilby [55]. For more details on Bayesian inference please see Sec. 1.7.

4.2.7 Indistinguishability criteria

To analyse waveform accuracy an *indistinguishability criteria* can be used which relates the match between waveforms to a signal-to-noise ratio (SNR) at which the waveforms will become distinguishable in a process of interest such as gravitational wave searches or parameter estimation. The general form for this criteria was established by [127, 181, 195] that relate differences in waveform amplitude and phase instead of the match. A commonly used form of the criteria was established by [59] that depends on the number of intrinsic parameters and more recently has been reconsidered by [94].

Two waveforms h_1 and h_2 are said to be indistinguishable as defined by [59] if they satisfy the condition

$$M(h_1, h_2) \geq 1 - \frac{(\chi^2_k)^{-1}(p)}{2\rho^2}. \tag{4.10}$$

$(\chi^2_k)^{-1}(p)$ is the inverse of the cumulative distribution function of the chi-square distribution. p is the confidence level of an associated confidence region which is considered to represent an unbiased region of a posterior distribution. For the analysis in this chapter the number of degrees of freedom k of the χ^2 distribution is four, and the 90% confidence region is considered to represent unbiased results. As such the inequality Eq. 4.10 may be equivalently written as

$$M(h_1, h_2) \geq 1 - \frac{3.89}{\rho^2}, \tag{4.11}$$

$$\rho \leq \sqrt{\frac{3.89}{1 - M(h_1, h_2)}}. \tag{4.12}$$

The form of the indistinguishability criteria given by Eq. 4.10 derived by considering a signal $s(t)$ containing a waveform $h(t)$ plus noise $n(t)$ and a waveform model that can perfectly reproduce $h(t)$. A non-zero mismatch is then purely the result of the added noise and consequently the criteria Eq. (4.10) is violated only because of noise. Recently it has become common for this criteria also to be used to compare two waveforms with no additive noise. This has been found to give reasonable albeit often very strict specifications on distinguishably.

There are two main assumptions that are violated that lead to the overly strict result. The *effectual* match or *fitting factor* is not equal to 1 and the effectual parameters are which the effectual match is achieved are not the same for both waveforms.

For the analysis there are three classes of waveform that are of interest. $h_{\rm NR}$ are the NR hybrid waveforms, $h_{\rm Phen}$ are PhenomD waveforms evaluated at the parameters of the associated NR and $h_{\rm opt}$ which are PhenomD waveforms evaluated at the effectual parameters between PhenomD and $h_{\rm NR}$. It will be demonstrated that in general the appropriate match to use for the indistinguishability criteria is $M(h_{\rm NR}, h_{\rm opt})$.

4.3 Results

4.3.1 Parameter estimation for NR injections

The PE results for the $(\rho, M_{\rm total}) = (250, 300M_{\odot})$ injections of sixteen NR cases used to calibrate and validate `PhenomD` are presented in the posterior plots in Figs. 4.2 and 4.3. The posterior plots visualise the one-dimensional posterior distributions for the four system parameters $(m_1, m_2, \chi_{\rm eff}, \chi_{\rm PN})$. For most configurations there is a clear bias in at least one of the posteriors, with the injected value lying outside the 90% confidence interval. Note however that there are two cases, $(q, \chi_1, \chi_2) = (18, -0.8, 0)$ and $(q, \chi_1, \chi_2) = (18, -0.4, 0)$ where the injected values lie within the 90% confidence interval for all 4 parameters.

For each case the SNR at which the hybrid injection would be indistinguishable is estimated from the waveform generated with `PhenomD` when evaluated at the same parameters of the injection. The following method is used to achieve this.

1. **Calculate covariance information**
   The covariance information for the four dimensional posterior data in $(m_1, m_2, \chi_{\rm eff}, \chi_{\rm PN})$. The three extrinsic parameters $(D_{\rm L}, \phi_c, t_c)$ are not included in the covariance calculation as these parameters are optimised over for match calculations which are the basis for the indistinguishability criteria that will be compared to in Sec. 4.3.2.

2. **Whiten posteriors and injection parameters**
   The marginalised 4D posteriors and injections parameters are translated by the mean value of the posteriors and transformed by the calculated covariance matrix to whiten the relevant data.

3. **Scale whitened posteriors to injection parameters**
   The whitened posterior data is scaled until the 4D 90% confidence region covers the whitened injection parameters. A radius of 2.79 is used which is the radius of the 90% confidence region for data distributed according to a 4D gaussian distribution. Based on the approximate scaling of high SNR PE posteriors the scaling factor is applied to the injection SNR of 250 to calculate the SNR at which the injection parameter is covered.

When the 90% confidence region of the posterior covers the injection parameters the case is considered to be indistinguishable. The calculated indistinguishable SNRs for each injection are presented in Table.4.1 as $\rho_{\rm post}$.

Two examples of this transformation method are presented in Figs. 4.5 and 4.6. These figures present the whitened posterior data projected onto each of the six two-dimensional planes of the principal component space of the posterior distribution. The projections are annotated with the 90% confidence region of the PE results and the inferred 90% confidence region calculated by scaling the recovered 90% confidence region as described in step 3.

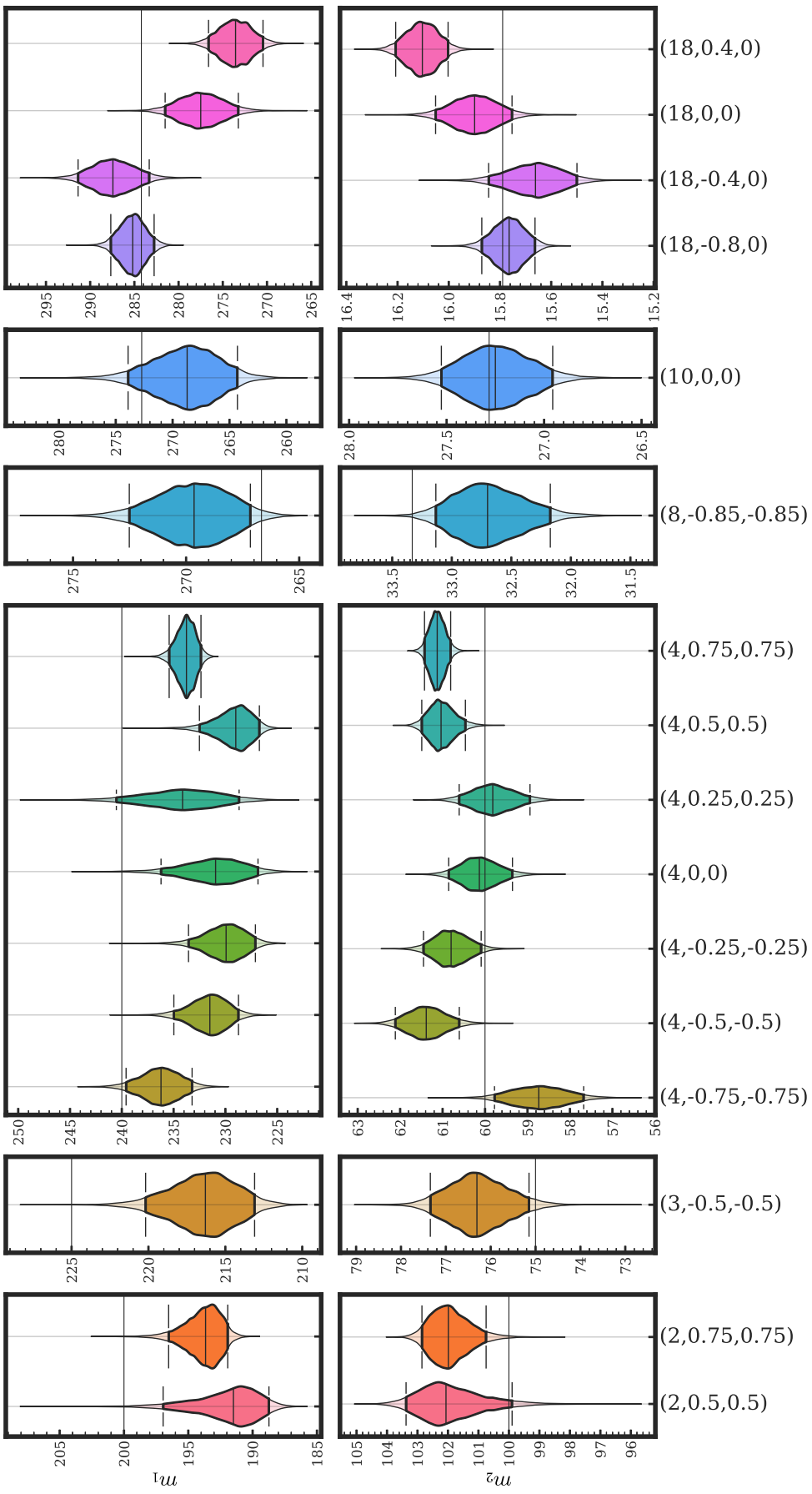

Figure 4.2: Marginalised one dimension posterior data for the two component masses m_1 and m_2. The bright central coloured region of each distribution are 90% confidence regions bounded by thick black lines. The solid black line that is runs horizontally inside the posterior distribution violins is the median value. The solid black line the runs horizontally across the entire width of each axis is the injected component mass value.

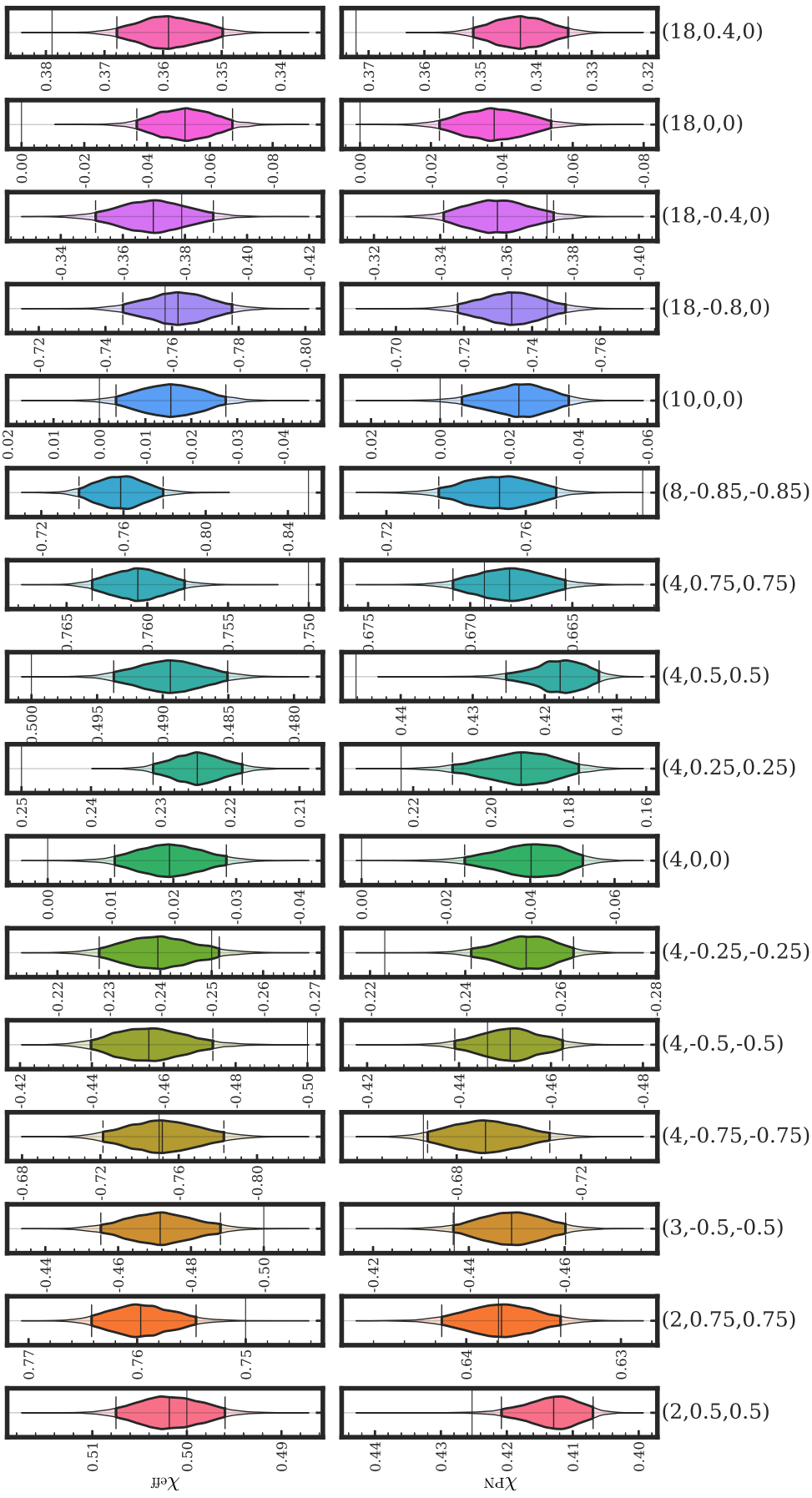

Figure 4.3: Marginalised one dimension posterior data for the derived spin values $\chi_{\rm eff}$ and $\chi_{\rm PN}$. The bright central coloured region of each distribution are 90% confidence regions bounded by thick black lines. The solid black line that is runs horizontally inside the posterior distribution violins is the median value. The solid black line the runs horizontally across the entire width of each axis is the injected component mass value.

4.3.2 Comparison with indistinguishability criteria

The original form of the indistinguishability criteria Eq. 4.10 typically uses the match between two different waveforms that are supposed to represent the same physical system, otherwise known as the faithfulness. However as already discussed in Secs. 4.1 and 4.2.7 this is likely to lead to results that are overly conservative. To address this issue the indistinguishability criteria is considered using three different matches between three different waveforms, the hybrid waveforms $h_{\rm hyb}$, $h_{\rm inj}$ which are `PhenomD` waveforms evaluated at the hybrid waveforms parameters, and $h_{\rm opt}$ which are `PhenomD` waveforms evaluated at parameters that maximise the match with the hybrid waveforms. The results for these three matches, $M(h_{\rm inj}, h_{\rm hyb})$, $M(h_{\rm inj}, h_{\rm opt})$, and $M(h_{\rm hyb}, h_{\rm opt})$ for each injection are presented in Table 4.2. The indistinguishable SNRs given by Eq. 4.12 are calculated for $M(h_{\rm inj}, h_{\rm hyb})$ and $M(h_{\rm inj}, h_{\rm opt})$, also presented in Table 4.1 as $\rho_{\rm inj,hyb}$ and $\rho_{\rm inj,opt}$ respectively. The results of the three distinguishable SNRs $\rho_{\rm post}$, $\rho_{\rm inj,hyb}$, and $\rho_{\rm inj,opt}$ are also visualized in Fig. 4.4. Figs. 4.5 and 4.6 are also annotated with the inferred 90% confidence regions for SNRs given by $\rho_{\rm inj,opt}$ by scaling the 90% confidence region of the posterior data.

Fig. 4.5 visualizes the case $(q, \chi_1, \chi_2) = (4, 0.25, 0.25)$ where $\rho_{\rm inj,opt}$ best agrees with $\rho_{\rm post}$. Fig. 4.6 visualizes the case $(q, \chi_1, \chi_2) = (18, -0.8, 0.0)$. It can be see from Figs. 4.2 and 4.3 that there is no bias in any of the mass or spin parameters in the marginalised one-dimensional posteriors. However Fig. 4.6 clearly shows that the posterior distribution is recovered far away from the injected parameters. This demonstrates that in general you have to consider more than just one-dimensional posteriors in order to identify parameter estimation biases.

Before comparing the different calculations of indistinguishable SNR in greater detail across the parameter space of cases, a few important assumptions will be highlighted. $\rho_{\rm post}$ is considered the *correct* result, as it is the most robust value that is derived from the marginalised posterior data. However it is still subject to several approximations. It is assumed that the posterior distributions can be well approximated by normal distributions in order to calculate ellipsoidal confidence regions. It can be seen in Figs. 4.5 and 4.6 that the projections of the whitened posterior distribution are not perfectly gaussian. As a corollary of assuming Gaussian distributions it will also be assumed that the mean of the posterior distributions coincide with the optimized match parameters. In practice this does not happen both due to normality being partially violated and posterior results that may not have completely converged. However the optimized match parameters always lie within the 20% confidence region of all cases and do not have a qualitative impact on the results of the analysis.

For every case the original indistinguishability criteria underestimates the distinguishable SNR. For the sixteen cases the modified criteria using $M(h_{\rm inj}, h_{\rm opt})$ to calculate $\rho_{\rm inj,opt}$ gives a better prediction for 14 of the cases. Overall it is found that the original criteria has a root-mean-squared relative percentage error of 39% and the modified criteria 29%. If the two cases where the original criteria performs better are excluded, then the root-mean-

q	χ_1	χ_2	$M(h_{\rm inj}, h_{\rm NR})$	$M(h_{\rm inj}, h_{\rm opt})$	$M(h_{\rm NR}, h_{\rm opt})$	$\rho_{\rm post}$	$\rho_{\rm inj,NR}$	$\rho_{\rm inj,opt}$
2	0.50	0.50	0.9954	0.9975	0.9978	41.15	30.67	41.75
2	0.75	0.75	0.9961	0.9977	0.9984	39.51	33.51	43.61
3	-0.50	-0.50	0.9950	0.9979	0.9970	42.26	29.38	45.11
4	-0.75	-0.75	0.9944	0.9980	0.9962	45.73	27.84	46.15
4	-0.50	-0.50	0.9939	0.9982	0.9957	45.16	26.69	48.71
4	-0.25	-0.25	0.9957	0.9992	0.9965	59.95	31.73	72.54
4	0.00	0.00	0.9964	0.9993	0.9970	69.42	34.56	78.06
4	0.25	0.25	0.9968	0.9993	0.9975	75.85	37.08	76.66
4	0.50	0.50	0.9972	0.9992	0.9980	51.66	39.27	74.01
4	0.75	0.75	0.9977	0.9996	0.9983	52.64	43.79	99.28
8	-0.85	-0.85	0.9927	0.9984	0.9942	46.69	24.40	52.42
10	0.00	0.00	0.9972	0.9989	0.9984	65.34	39.60	61.75
18	-0.80	0.00	0.9854	0.9901	0.9952	18.98	17.20	20.96
18	-0.40	0.00	0.9956	0.9986	0.9970	61.62	31.49	55.43
18	0.00	0.00	0.9971	0.9986	0.9985	54.57	38.73	56.19
18	0.40	0.00	0.9956	0.9969	0.9987	79.72	31.26	37.21
8	0.80	0.00	0.9665	0.9745	0.9929	5.25	11.37	13.04
18	0.80	0.00	0.8986	0.9169	0.9840	1.90	6.54	7.22

Table 4.2: Results from NR injections at SNR $\rho = 250$ and total mass $M_{\rm total} = 300M_{\odot}$. The first three columns describe the configuration of the system. $M(h_{\rm inj}, h_{\rm NR})$ is the match between the hybrid injection and PhenomD at the hybrid parameters. $M(h_{\rm inj}, h_{\rm opt})$ is the match between PhenomD evaluated at the hybrid parameters and PhenomD evaluated at the hybrid-PhenomD effectual parameters. $M(h_{\rm NR}, h_{\rm opt})$ is the match between the hybrid injection and PhenomD evaluated at the hybrid-PhenomD effectual parameters. $\rho_{\rm post}$ is the SNR at which the hybrid injection will be indistinguishable from PhenomD evaluated at the injection parameters derived from scaling the SNR 250 posterior. $\rho_{\rm inj,NR}$ is the SNR at which the hybrid injection and PhenomD at the hybrid parameters will be indistinguishable according to Eq. (4.10). $\rho_{\rm inj,opt}$ is the SNR at which the hybrid injection and PhenomD at the effectual parameters will be indistinguishable according to Eq. (4.10).

squared relative percentage error increases to 41% for the original criteria but drops to 17% for the modified criteria.

Across the parameter space the original criteria predicts on average a distinguishable SNR of 32.32, the modified criteria an average SNR of 56.87, and PE results an average SNR of 53.14. While these results again indicate that in general the original criteria will significantly underestimate the distinguishable SNR, there is still a broad spread of distinguishable SNRs across the parameter space. This spread is fairly random with no clear trend along any parameter space direction such as mass ratio or component spins.

While acknowledging these caveats, an SNR of 55 is used as a proxy for the SNR at which `PhenomD` becomes distinguishable from NR. Based on this the indistinguishable SNR will need to be improved by a factor of 2.71 in order to ensure less than 0.01% of detections lead to unbiased parameter estimations and improve the SNR by a factor of 12.6 to reduce this to less than 0.00001% of detections. These translate to reductions in

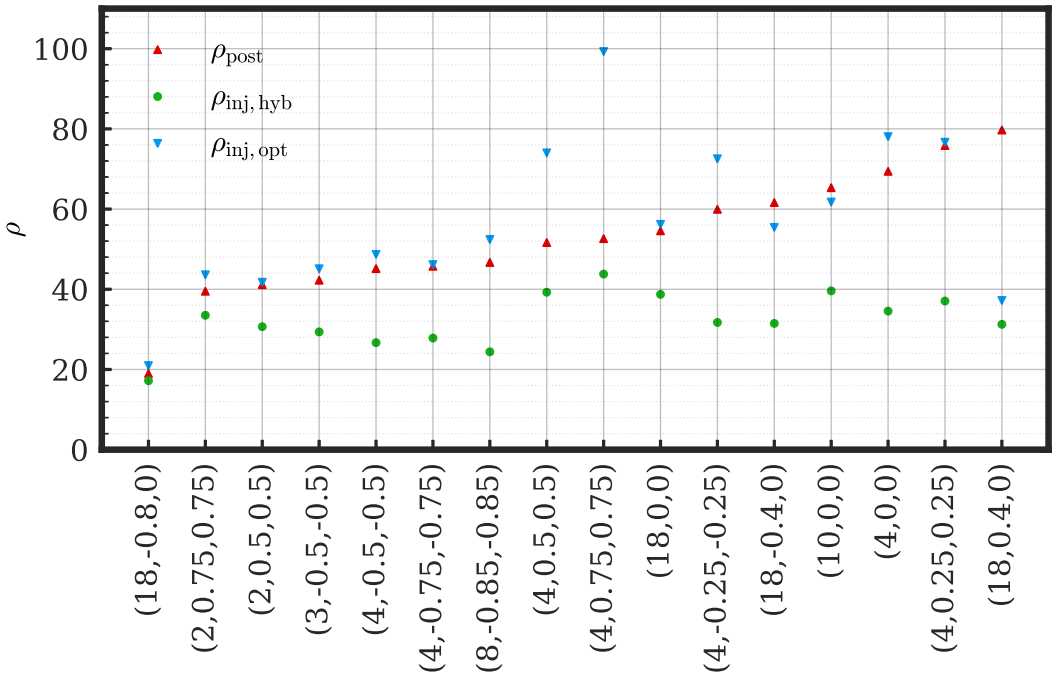

Figure 4.4: The three indistinguishable SNRs ordered by the indistinguishable SNR $p_{\rm post}$ inferred from the parameter estimation results. For numerical values for each SNR please see Table 4.1.

mismatch by a factor of 7.34 and a factor of 158.76 respectively. Because in general the modified criteria gives more accurate predictions, this mismatch improvement applies to the optimized match or effectualness. As such the improvements in faithfulness with NR will need to be greater. While the effectualness can be expected to decrease approximately linearly with the faithfulness, there is no fixed constant of proportionality between the two when surveying the parameter space based on the results. A minimum mismatch ratio $M(h_{\rm inj}, h_{\rm hyb})/M(h_{\rm inj}, h_{\rm opt})$ is found of 1.42 and maximum of 5.23. The conclusion is that an order of magnitude is the minimum necessary improvement in faithfulness between GW waveform model and NR to prepare for the 3G era, however three orders of magnitude in improvement would be the recommendation in order to ensure reliable scientific output from observations. This level of improvement requires faithfulness better than the mismatch error in current NR waveforms. In order to facilitate this recommendation at least one order of magnitude improvement in NR mismatch error will be required.

4.4 Discussion

The driving objectives of this study has been to understand what improvements need to be made to GW models in order to prepare for 3G ground based detectors, and as a result what improvement in NR are needed to facilitate this. The main body of this study has addressed this first objective, which concluded that three orders of magnitude improvement in faithfulness with NR is desirable. How can this be achieved, and is it all dependant on

improving NR and related to the second objective of how much does NR need to improve?

For simple linear regression models to approximate GWs it would be expected that as a result of the central limit theorem that the error in regression parameters and root-mean-square model error would decrease proportional to $\sqrt{\epsilon/N}$ where ϵ is the average NR mismatch error [206] and N is the number of NR simulations used in the calibration of such a model. It would be expected for model faithfulness mismatch to decrease proportional to $\sqrt[4]{\epsilon/N}$. While the computational cost of NR simulations increases as you move to higher mass ratios, the number and quality of simulations needs to improve approximately uniformly across the parameters space. For BAM the error ϵ decreases linearly with computational cost. Similarly the computational cost increases linearly with the number of simulations. This means that decreasing model error does not favour reducing data error or data quantity. However in practice larger quantities of smaller NR simulations are easier to manage than a small number of large simulations. As such it would be recommended to meet the NR accuracy requirements but not seek to exceed them and from that point focus on NR quantity over improved accuracy.

However most GW models are non-linear models. When considering the data driven surrogate models an exponential rate of convergence with number of calibration waveforms is observed [124], which suggests that only a reasonably sized collection of NR waveforms will be needed to achieve the recommended waveform accuracy. As a result general asymptotic convergence results may cease to be relevant. In general exponential convergence might not be expected for other modelling strategies such as the multilevel regression used by the phenomenological family, however better convergence rates than linear models might be expected. This will very much depend on each modelling strategy and ansatz.

3G ground based detectors are still several years away from beginning construction and even further away from operation. While this is not a recommendation to be complacent with GW modelling, the rate of improvement in aligned spin GW models is continued such as the `IMRPhenomX` family of models [221] using data of comparable accuracy used to calibrate `PhenomD`, then it would be expected that the accuracy recommendations for waveform models to be achieved before first detections are made with 3G detectors.

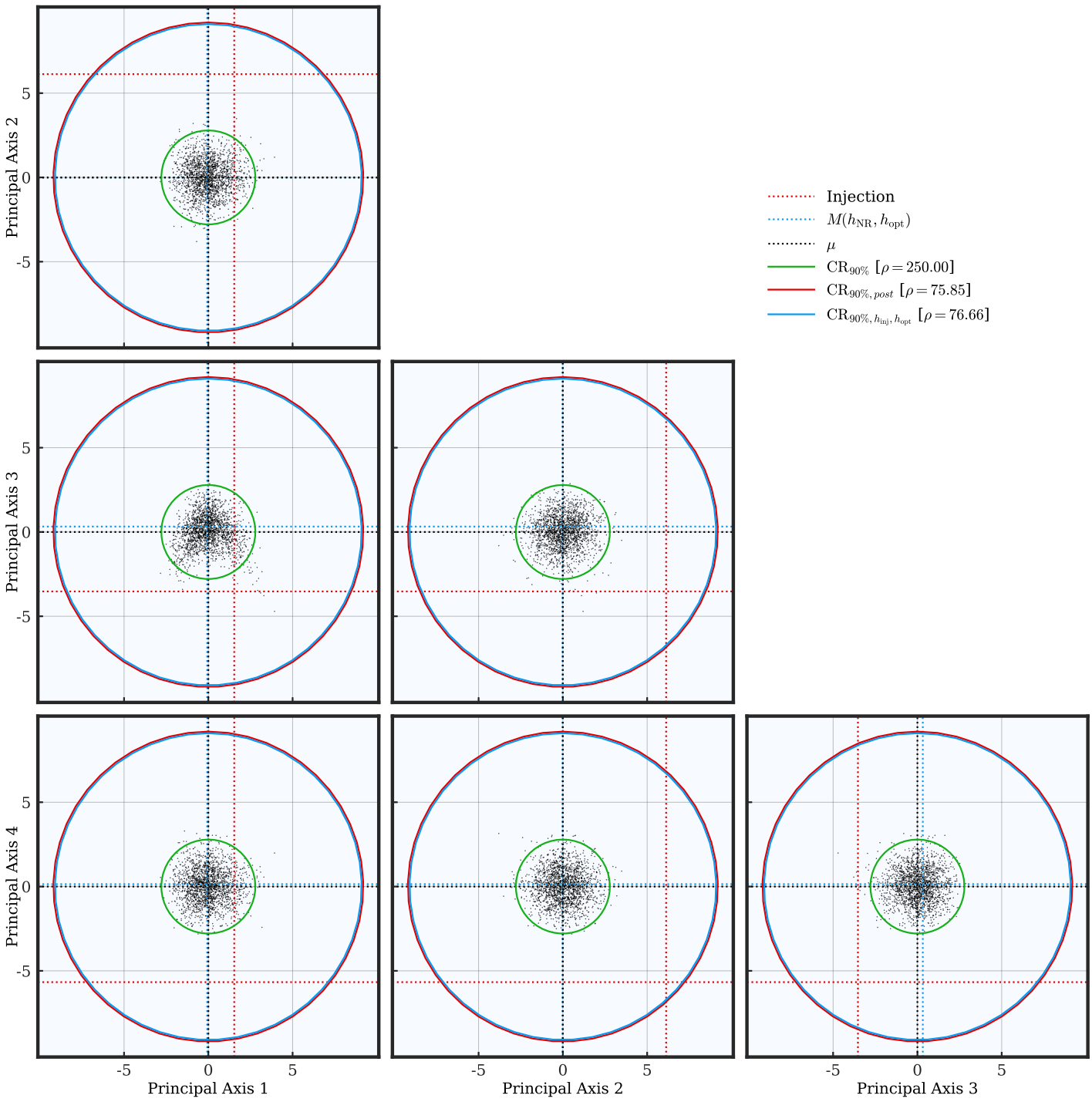

Figure 4.5: Two dimensional projections of the whitened $(m_1, m_2, \chi_{\rm eff}, \chi_{\rm PN})$ posterior data for the case $(q, \chi_1, \chi_2) = (4, 0.25, 0.25)$. The red dashed lines are the projections of the injection parameters under the covariance transformation of the whitening matrix. The blue dashed lines are the transformed effectual parameters. The solid green rings are the projections of the 90% confidence region of a 4D multivariate normal distribution. The solid red ring is the projection of the 90% confidence scaled such that it now contains the transformed injection parameters. The solid blue ring is the expected 90% confidence in the whitened space inferred from the indistinguishability criteria Eq. (4.10) using the match $M(h_{\rm inj}, h_{\rm opt})$.

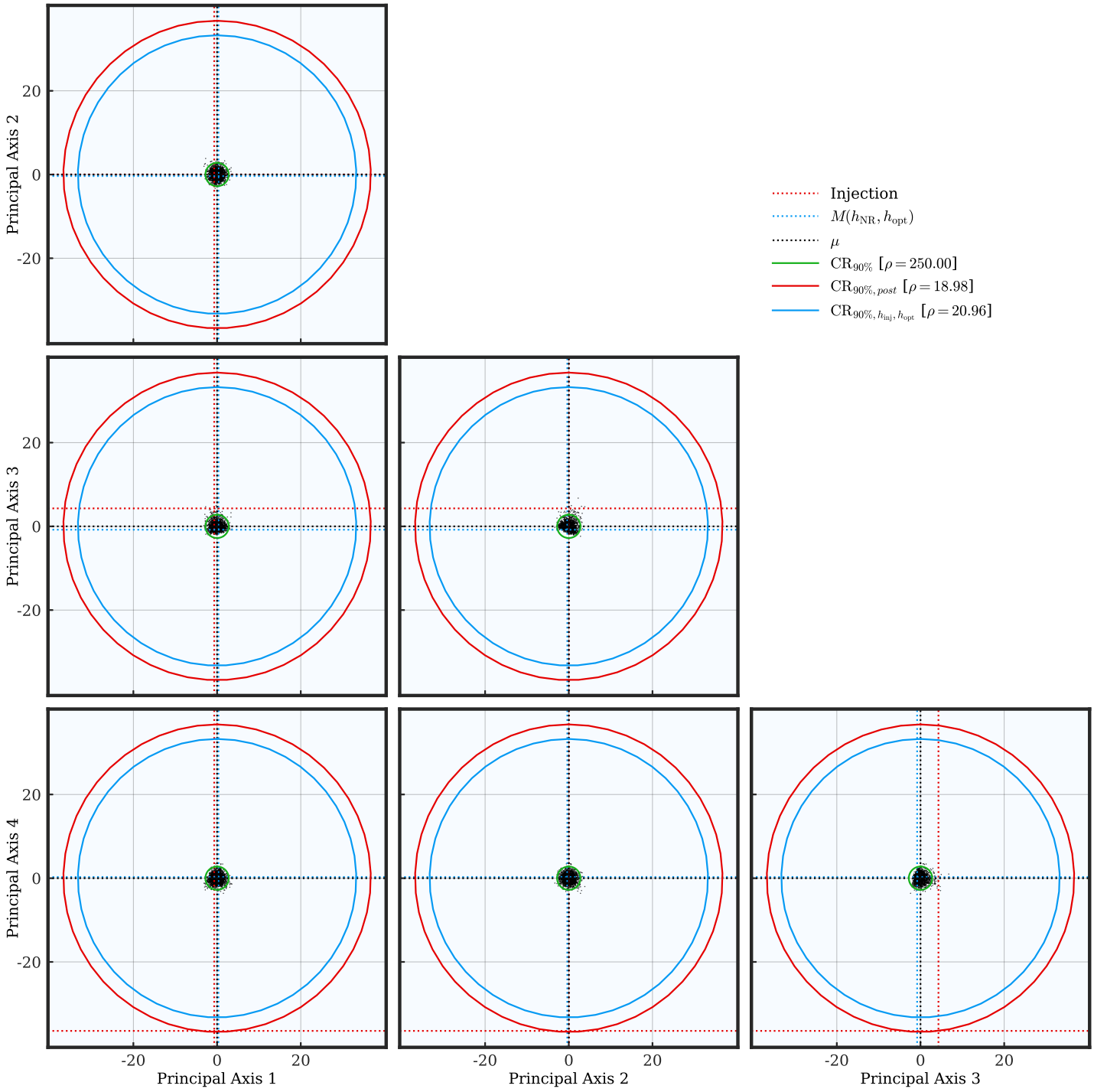

Figure 4.6: Two dimensional projections of the whitened $(m_1, m_2, \chi_{\rm eff}, \chi_{\rm PN})$ posterior data for the case $(q, \chi_1, \chi_2) = (18, -0.8, 0.0)$. The red dashed lines are the projections of the injection parameters under the covariance transformation of the whitening matrix. The blue dashed lines are the transformed effectual parameters. The solid green rings are the projections of the 90% confidence region of a 4D multivariate normal distribution. The solid red ring is the projection of the 90% confidence scaled such that it now contains the transformed injection parameters. The solid blue ring is the expected 90% confidence in the whitened space inferred from the indistinguishability criteria Eq. (4.10) using the match $M(h_{\rm inj}, h_{\rm opt})$.

Part II

Numerical methods and software development

Chapter 5

Adaptive multivariate rational fitting

In this chapter linear modelling techniques are presented, namely the greedy-multivariate-polynomial (GMVP) and greedy-multivariate-rational (GMVR) algorithms, in which model terms are iteratively learned with no initial guess. The description of GMVP given here is complementary to similar algorithms used to model QNM excitation amplitudes, $A_{\ell mn}$, as present in reference [91, 183, 187]. As will be discussed, the GMVR algorithm is an iterative approach to the (pseudo) linear modelling of multivariate rational functions, wherein iterations of linear inversions are used to refine the ultimately non-linear model. The GMVP and GMVR algorithms were originally presented along side fits for QNM frequencies and mixing coefficients in [184]. The QNM data and associated fits will not be presented. Instead the focus of this chapter will be the on greedy algorithms. However applications of these algorithms will be discussed in Sec. 5.3.

In the rudimentary form presented here, both GMVP and GMVR are intended for use with low noise data (e.g. the results of analytic calculations), and each employs a reverse (or negative) greedy algorithm to counter over modelling [123, 92]. As the underlying process for GMVP and GMVR is stepwise regression, highly correlated basis vectors (i.e. polynomial terms) are handled via an approach given the name *degree tempering*. Results suggest that the versions of GMVP and GMVR presented here may apply in instances where training data are approximately noiseless, and an initial guess is difficult to obtain. Both algorithms are publicly available in Python via [185].

The plan of this chapter is as follows. In Sec. 5.1, the GMVP and GMVR algorithms will be described. In Sec. 5.2 the GMVR algorithm will be applied to a toy model to elucidate the benefits of the algorithm. Finally in Sec. 5.3 the effectiveness of GMVP and GMVR will be reviewed, and current and potential applications for these methods will be discussed.

5.1 Methods

Within the topic of regression, linear regression has particular advantages. Its matrix based formulation can be computationally efficient, and it does not require initial guesses for model parameters. Perhaps most intriguingly, the formal series expansions of smooth functions

support linear and rational models (e.g. Padé approximants) that have application to many datasets. With this in mind, algorithms for the linear (polynomial and rational) modelling of scalar functions (real or complex) of many variables will be developed.

Consider a scalar function, f, of $N+1$ variables sampled in j, $\boldsymbol{x}_j = \{x_{\alpha j}\}_{\alpha=0}^{N}$, then $f(\boldsymbol{x}_j)$ can be represented (possibly inaccurately) as a sum over $K+1$ linearly independent basis functions, $\phi_k(\boldsymbol{x}_j)$:

$$f(\boldsymbol{x}_j) \;=\; \sum_{k=0}^{K} \mu_k \, \phi_k(\boldsymbol{x}_j) \; . \tag{5.1}$$

The central player in Eq. (5.1) is the set of basis coefficients μ_k. Typically, $\phi_k(\boldsymbol{x}_j)$ are chosen or derived to capture inherent features of $f(\boldsymbol{x}_j)$. With $\phi_k(\boldsymbol{x}_j)$ assumed to be known, the linear representation (namely Eq. (5.1)) is lastly defined the set of μ_k.

From here it is useful to note that Eq. (5.1) has a linear homogeneous matrix form. In particular, defining $U_{jk} = \phi_k(\boldsymbol{x}_j)$, $f_j = f(\boldsymbol{x}_j)$ and $\boldsymbol{f} = \boldsymbol{U}\ \boldsymbol{\mu}$, implies that

$$\boldsymbol{\mu} = \boldsymbol{P}\ \boldsymbol{f} \; , \tag{5.2}$$

where

$$\boldsymbol{P} = (\boldsymbol{U}^{*}\boldsymbol{U})^{-1}\,\boldsymbol{U}^{*} \tag{5.3}$$

is the *pseudo-inverse* [200, 217] of $\boldsymbol{U}$, which exists if $\boldsymbol{U}^{*}\boldsymbol{U}$ is non-singular. Here "$*$" denotes the conjugate transpose.

Eq. (5.1), and related discussion through Eq. (5.3) illustrate the most rudimentary solution to the linear modelling problem. However, there are many ways to expand upon and refine the solution presented thus far. In the following subsections two such approaches will be considered. First to be considered will be the general polynomial modelling of multivariate scalar functions. This will encompass the `GMVP` algorithm. Second, the `GMVP` approach will be built upon by considering models of rational functions (polynomials divided by polynomials). To consider these two approaches in a largely automated way (i.e. where the set of possible basis functions is known, but the select basis functions ultimately used are *learned*), they will make use of the *greedy* algorithm approach [123, 107, 245, 212].

5.1.1 A Generic Greedy Algorithm

While often only a single model is wanted for a given dataset (e.g. some approximation of $\boldsymbol{f}$ from numerical calculation or experiment), there are often many more modelling choices than desired. In particular, consider the set of all possible basis functions, which will be called the *symbol space*. Then the problem of determining how many, and which basis vectors (i.e. symbols) to use is a problem of combinatoric complexity.

A well known method for finding an approximate solution to this problem is the so-called *greedy* algorithm (e.g. [123, 107]), where models are iteratively construct with increasing

number of symbols. The process begins by finding the single symbol (basis vector) that yields the most accurate model in the sense of minimizing the least-squares error. That encompasses the first iteration of a process in which symbols will be greedily added to the model. In each subsequent iteration, remaining symbols are added to the model one at a time, resulting in many trial models, each with its own representation error. The trial model with smallest representation error is kept for the next greedy iteration. In this way, a list of optimal model symbols is learned. This *forward greedy* process ends when the model accuracy, and/or changes thereof, passes a previously specified threshold. This rough algorithmic picture is encapsulated by Alg. 1. The very similar *negative* greedy algorithm removes model symbols until representation error increases beyond a specified threshold.

Algorithm 1 A positive (forward) greedy algorithm, `PGREEDY`. Note that a required input, $\mathcal{A}$, is a function that takes in a list of basis symbols, and outputs an estimator of fit error (e.g. L^2 norm). In this setting, $\mathcal{A}$ is assumed to have access to peripheral information, such as the training data.

Input: $\{\boldsymbol{\lambda}_{bulk} = \text{basis symbols}, \mathcal{A} = \text{action}, tol = \text{greedy tolerance}\}$

Define empty list of kept symbols: $\boldsymbol{\lambda}_{kept} = \{\}$
Initialize estimator value and loop boolean: $\epsilon_{last} = \inf$, $done =$ False
while not $done$ **do**
  $\epsilon_{min} = \epsilon_{last}$
  for $\boldsymbol{\lambda}$ in $\boldsymbol{\lambda}^{bulk}$ **do**
    $\boldsymbol{\lambda}_{trial} = \boldsymbol{\lambda}_{kept} \cup \{\boldsymbol{\lambda}\}$ (add $\boldsymbol{\lambda}$ to $\boldsymbol{\lambda}_{kept}$)
    $\epsilon = \mathcal{A}(\boldsymbol{\lambda}_{trial})$ (action returns fit error)
    if $\epsilon < \epsilon_{min}$ **then**
      $\epsilon_{min} = \epsilon$ (store trial min)
      $\boldsymbol{\lambda}_{min} = \boldsymbol{\lambda}_{trial}$
    end if
  end for
  $done = |\epsilon_{min} - \epsilon_{last}| < tol$
  if not $done$ **then**
    $\epsilon_{last} = \epsilon_{min}$
    $\boldsymbol{\lambda}_{kept} = \boldsymbol{\lambda}_{kept} \cup \boldsymbol{\lambda}_{min}$ (update kept symbols)
  end if
end while

Output: $\boldsymbol{\lambda}_{kept}$ (the Greedy Basis)

5.1.2 Greedy Multivariate Polynomial Fitting

The study of continuous scalar functions often centers about their Taylor series expansion. In that instance, it is clear that any infinitely differentiable scalar function of many variables

can be represented in terms of its derivatives by

$$f(\boldsymbol{x}+\boldsymbol{h}) = e^{\boldsymbol{x}\cdot\boldsymbol{\nabla}'} f(\boldsymbol{x}')|_{\boldsymbol{x}'=\boldsymbol{h}} \approx \sum_{k=0}^{K} \frac{1}{k!} (\boldsymbol{x}\cdot\boldsymbol{\nabla}')^k f(\boldsymbol{x}')|_{\boldsymbol{x}'=\boldsymbol{h}} \tag{5.4}$$

The implication of the second line from the first of Eq. (5.4) uses the definition of the exponential function (i.e. its series expansion). In the second line, the equality has been replaced by an approximation as the linear representation has been limited to $K+1$ terms. Formally, the applicability of the truncated expansion over a local region is made rigorous by the Generalised Stone-Weierstrass Theorem [144].

These ideas are key to the perspective of `GMVP`. Given training data thought to be related to a smooth multivariate function, it may, particularly on small scales, be well approximated by a truncated series expansion in an appropriate coordinate basis.

In this setting, the uncertainty of which and how many basis terms to include makes this a problem ripe for the application of linear modelling driven by a greedy process, namely Eq. (5.2) and Alg. (1) .

Here, the basis symbols required by Alg. (1) are the multinomial terms in Eq. (5.4). Each term is an element of the tensor-product of the sets of powers of each coordinate of a chosen representation of the models domain. That is $\boldsymbol{\lambda}_{bulk} = \{x_0^{d_0} x_1^{d_1} \dots x_N^{d_N} \mid d_i \in \{0,\dots,K\}, i \in \{0,\dots,N\}\}$. Note that in practice it may be useful to encode elements of $\boldsymbol{\lambda}_{bulk}$ with strings representing their constituents (e.g. $x_0x_0x_1x_2x_2x_4$ could be represented by the string "001224"). This provides a way of bijectively mapping between symbols and numerical basis vectors.

The action, $\mathcal{A}(\boldsymbol{\lambda}_{trial})$, required by Alg. (1) encompasses the evaluation of Eq. (5.2) to solve for the basis coefficients, μ_k, and the calculation of the modelling error. An explicit sketch of this is given by Alg. (2).

Algorithm 2 $\mathcal{A}_{\texttt{GMVP}}$, the action for `GMVP`. Model calculation given basis symbols, and output of model error estimate.

1: **Input:** $\boldsymbol{\lambda}_{trial}$

2: Calculate μ_k via Eq. (5.2).

3: Calculate the model representation error, e.g.: $\epsilon = \|\boldsymbol{U}\boldsymbol{\mu} - \boldsymbol{f}\|/\|\boldsymbol{f}\|$, where $\|a\|$ is the L^2 norm of a.

4: **Output:** ϵ

The combination of these two ideas alone results in an algorithm prone to a deficit of stepwise methods, the algorithm may confuse correlated basis vectors (e.g. x^2 may be confused with x^4). To counter this, the algorithm can incrementally increase, or *temper*, the maximum allowed multinomial degree. For example, when iterating through allowed degrees, if the current maximum degree is 3, then degree 4 terms, such as $x_0x_1x_3^2$, will not be considered within the space of model symbols. The degree tempering process halts when

increasing the maximum allowed degree has no significant effect on model representation error. The combination of degree tempering with the greedy approach results in the GMVP algorithm as presented in Alg. (3).

Algorithm 3 GMVP, a degree tempered stepwise algorithm for multivariate polynomial modelling of scalar data.

Input: $\{x, f$,max_degree = 6, $tol\}$

Define, $\boldsymbol{\lambda}_{bulk}$, the bulk symbol space, to be the set of all multinomial combinations of basis vectors up to a predefined maximum order.
Define $\mathcal{A}_{\texttt{GMVP}}$ according to Alg. (2).
Given max_degree, define, D, a list of allowed polynomial degrees (e.g. $\{0, 1, 2, 3, 4, 5, 6\}$)
for d **in** D **do**
    Define $\boldsymbol{\lambda}_{bulk}^{(d)}$ as all symbols from $\boldsymbol{\lambda}_{bulk}$ with degree less than or equal to current degree: $\boldsymbol{\lambda}_{bulk}^{(d)}$
    Using $\boldsymbol{\lambda}_{bulk}^{(d)}$, apply Alg. (1), PGREEDY, with $\mathcal{A}_{\texttt{GMVP}}$ to get symbol subset, $\boldsymbol{\lambda}_{opt}^{(d)}$ and estimator val, $\epsilon_{opt}^{(d)}$
    if $|\epsilon_{opt}^{(d)} - \epsilon_{opt}^{(d-1)}| < tol$ **then**
        break
    end if
end for

Output: $\boldsymbol{\lambda}_{opt}^{(d)}$

5.1.3 Greedy Multivariate Rational Fitting

Despite the apparent universality of Eq. (5.4), there are many cases where K must be orders of magnitude greater than 1 in order for $\boldsymbol{f}$ to be accurately represented by a polynomial. In general, the optimal polynomial basis may not be clear, and so a more general set of ansatzes may be of use.

Of the simplest of such ansatzes are rational functions of the form

$$f(\boldsymbol{x}) = \bar{\mu} + \bar{\sigma}_f \, \frac{\sum_{r=0}^{R} a_r \, \phi_r(\boldsymbol{x})}{1 - \sum_{v=1}^{V} b_v \, \phi_v(\boldsymbol{x})} \, , \tag{5.5}$$

where $\bar{\mu}$ is the additive mean of $f(\boldsymbol{x})$, and $\bar{\sigma}_f$ is the standard deviation of $f(\boldsymbol{x})$, and ϕ_k are the multinomial's basis functions considered in the previous section. Note that, in Eq. (5.5), the sum over v does not include the constant term associated with ϕ_0.

While it is tempting to embrace $f(\boldsymbol{x})$ in Eq. (5.5) as a non-linear function and so resort to non-linear modelling methods, a reformulation reveals an underlying linear structure [222]. Let,

$$g = (f - \bar{\mu})/\bar{\sigma}_f, \tag{5.6}$$

then algebraic manipulation of Eq. (5.5) allows

$$g = \sum_{r=0}^{R} a_r \, \phi_r(\boldsymbol{x}) + g \sum_{v=1}^{V} b_v \, \phi_v(\boldsymbol{x}) \ . \tag{5.7}$$

The indices are free to be relabelled such that Eq. (5.7) is manifestly linear in a single index. At this stage, the j^{th} samples of the domain will be explicitly considered, for example $\boldsymbol{x}$ will be referred to as $\boldsymbol{x}_j$. These adjustments of perspective result in

$$g_j = \sum_{k=0}^{R+V} z_k \, \psi_k(\boldsymbol{x}_j) \ , \tag{5.8}$$

where

$$z_k \equiv \begin{cases} a_k, & 0 \leqslant k \leqslant R \\ b_k, & R+1 \leqslant k \leqslant R+V \end{cases} \tag{5.9}$$

$$\psi_k(\boldsymbol{x}_j) \equiv \begin{cases} \phi_k(\boldsymbol{x}_j), & 0 \leqslant k \leqslant R \\ \phi_k(\boldsymbol{x}_j) \, g_j, & R+1 \leqslant k \leqslant R+V \end{cases} \tag{5.10}$$

Recalling Eqs. (5.2) and (5.3), it follows that the coefficients of interest, a_k and b_k, may be estimated according to

$$\boldsymbol{\alpha} = \boldsymbol{P} \, \boldsymbol{g} \ , \tag{5.11}$$

where $\boldsymbol{g} \equiv (g_j)$, $\boldsymbol{P}$ is the pseudo-inverse of the matrix whose elements are $\psi_k(\boldsymbol{x}_j)$, and $\boldsymbol{\alpha} = (z_0, z_1, ...z_{R+V-1}, z_{R+V})$.

However, note that $\boldsymbol{P}$ depends non-trivially on g, and is therefore susceptible to noise in the training data. Briefly consider the effect of zero-mean noise on g, e.g. $g \to g + n$. In this, it may be that shown that n may be entirely relegated to $\boldsymbol{P}$. It is in this sense that Eq. (5.11) is insufficient to generally solve for $\boldsymbol{\alpha}$, as $\boldsymbol{P}$ may be adversely affected by noise.

The key to robustly solving for $\boldsymbol{\alpha}$ lies in iterative refinement [222]. Specifically, note that Eq. (5.7) may be modified to iteratively minimize the impact of numerical noise on $\boldsymbol{P}$. That is, to reduce the impact of noise on $\boldsymbol{P}$, it can be calculated using model evaluations of g rather than the original (noisy) training data. Define $g^{(0)} = g$ (i.e. g is the training data), with $\boldsymbol{P} = \boldsymbol{P}(\boldsymbol{g}^{(n)})$, then Eq. (5.11) generalizes to

$$\boldsymbol{\alpha}^{(n+1)} = \boldsymbol{P}(\boldsymbol{g}^{(n)}) \, \boldsymbol{g}^{(0)} \ . \tag{5.12}$$

In practice, Eq. (5.12) is solved for $\boldsymbol{\alpha}^{(n+1)}$, and then related $a_r^{(n+1)}$ and $b_v^{(n+1)}$ are used to

calculate $g_j^{(n+1)}$ via

$$g_j^{(n+1)} = \frac{\sum_{r=0}^{R} a_r^{(n+1)}\, \phi_r(\boldsymbol{x_j})}{1 \;-\; \sum_{v=1}^{V} b_v^{(n+1)}\, \phi_v(\boldsymbol{x_j})} \;. \tag{5.13}$$

Subsequently, $g_j^{(n+1)}$ is then fed back into Eq. (5.12) for further refinement. The refinement process is to terminate when a measure of model error (e.g. the L^2 norm $\|\boldsymbol{g}^{(0)} - \boldsymbol{g}^{(n)}\|$) passes a predetermined threshold. For the results presented in Sec. 5.2 the following model representation error was used

$$\epsilon^{(n)} = \left| \frac{\mathrm{Var}\left(\boldsymbol{g}^{(n)} - \boldsymbol{g}^{(0)}\right)}{\mathrm{Var}\left(\boldsymbol{g}^{(0)}\right)} \right| \tag{5.14}$$

where Var is the variance. This model representation error is similar to the square of the root-mean-squared-deviation normalized by the variance of the data set.

Much as in the case of multivariate polynomial fitting, an unknown number and content of basis symbols are left. In principle, the existence of a_r and b_v makes the problem more complicated, as one might imagine optimizing over each symbol space independently. To broach this complications, a greedy algorithm with degree tempering is again used. However, rather than independent greedy optimizations for the numerator and denominator bases symbols, Eq. (5.8) suggests that the appropriate labelling of symbols (e.g. *numerator* or *denominator*) may yield an effective flattening of the supposed 2D symbol selection problem. Put another way, rather than two simultaneous greedy optimizations over $R+1$ and V symbols (with $(R+1)V$ iterations), a single greedy process over $V+R+1$ symbols is performed, where each symbol is additionally labelled as being in the numerator or denominator.

With these conceptual tools in hand, constructing `GMVR` may proceed by first defining its action, $\mathcal{A}_{\texttt{GMVR}}$. This is done in Alg. (4). The combination of Eq. (5.12) and Eq. (5.13), along with `PGREEDY` and degree tempering, results in the `GMVR` algorithm as presented in Alg. (5). Both `GMVP` and `GMVR` are publicly available on Github through the `positive` repository (Ref. [185]), and may be imported in python via `positive.learning.gmvpfit` and `positive.learning.gmvrfit`.

5.2 GMVR Toy Problem

The goal for this section is to very briefly overview the functionality of the `GMVR` algorithm as implemented in [185]. While it is possible to investigate the output of `GMVR` with varying hyper-parameters (such as the tolerance input to Alg. 5), this section will focus only on a simple usage case. Similarly, `GMVR` as implemented in [185] involves a negative greedy phase to counter over-modelling in cases where the aforementioned tol is too low. This example will be restricted to a case where numerical noise is low, and the negative greedy step does not alter the output of Alg. 5.

Algorithm 4 $\mathcal{A}_{\texttt{GMVR}}$, the action for GMVR. Model calculation given basis symbols, and output of model error estimate.

Input: $\{\ \boldsymbol{\lambda}_{trial}, tol = 10^{-3}\ \}$

Let $n = 0$
Calculate $\boldsymbol{\alpha}^{(1)}$ via Eq. (5.12).
Calculate the model prediction $\boldsymbol{g}^{(1)}$ via Eq. (5.13).
Calculate the model representation error $\epsilon^{(1)}$.
Let $done = False$
while not $done$ **do**
    $n = n + 1$
    Calculate $\boldsymbol{\alpha}^{(n+1)}$ via Eq. (5.12).
    Calculate the model prediction $\boldsymbol{g}^{(n+1)}$ via Eq. (5.13).
    Calculate the model representation error $\epsilon^{(n+1)}$.
    $done = |\epsilon^{(n)} - \epsilon^{(n+1)}| < tol$
end while

Output: $\epsilon^{(n)}$

Algorithm 5 GMVR, a degree tempered stepwise algorithm for multivariate rational modelling of scalar data.

Input: $\{x, f$,max_degree = 6, $tol\}$

Define, $\boldsymbol{\lambda}_{bulk}$, the bulk symbol space, to be the set of all multinomial combinations of basis vectors up to a predefined maximum order. This is the combined symbol space for numerator and denominator symbols.
Define $\mathcal{A}_{\texttt{GMVR}}$ according to Alg. (4).
Given max_degree, define, D, a list of allowed polynomial degrees (e.g. $\{0, 1, 2, 3, 4, 5, 6\}$)
for d **in** D **do**
    Define $\boldsymbol{\lambda}_{bulk}^{(d)}$ as all symbols from $\boldsymbol{\lambda}_{bulk}$ with degree less than or equal to current degree: $\boldsymbol{\lambda}_{bulk}^{(d)}$
    Using $\boldsymbol{\lambda}_{bulk}^{(d)}$, apply Alg. (1), PGREEDY, with $\mathcal{A}_{\texttt{GMVP}}$ to get symbol subset, $\boldsymbol{\lambda}_{opt}^{(d)}$ and estimator val, $\epsilon_{opt}^{(d)}$
    if $|\epsilon_{opt}^{(d)} - \epsilon_{opt}^{(d-1)}| < tol$ **then**
        break
    end if
end for

Output: $\boldsymbol{\lambda}_{opt}^{(d)}$

Now consider the application of GMVR to a fiducial scalar function of the form,

$$f(x_0, x_1) = \mu + \sigma \left(\frac{a_0 + a_1 x_0 + a_2 x_1 + a_3 x_0 x_1}{1 + b_1\, x_0^2 + b_2 x_1^2} \right) + 0.05\, n \ , \tag{5.15}$$

where n is a uniform random variable on $[-1, 1]$. Towards easily identifying test values for a_j and b_k with those recovered, it is more straightforward to distribute σ to the denominator, yielding

$$f(x_0, x_1) = \mu + \frac{a_0 + a_1 x_0 + a_2 x_1 + a_3 x_0 x_1}{1/\sigma + (b_1/\sigma)\, x_0^2 + (b_2/\sigma) x_1^2} + 0.05\, n \ . \tag{5.16}$$

Under this perspective test data generated with the parameters listed in Table 5.1 will be considered.

To generate the test data, Eq. (5.16) is evaluated with 25 points along x_0 and x_1 (with 25^2 total points), where each is between -3 and 3. Though not a requirement of GMVR, for simplicity of presentation, domain points are equally spaced.

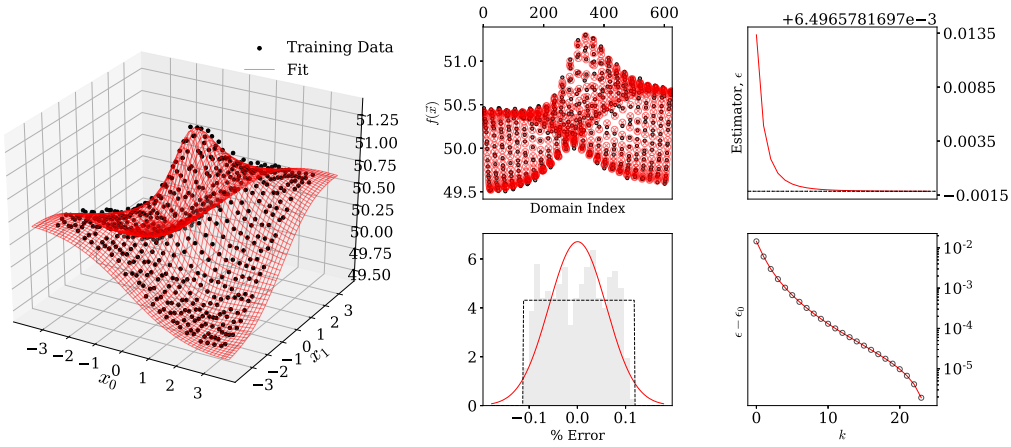

Figure 5.1: Standard summary plot for Greedy Multivariate Rational fitting algorithm (GMVR) as implemented in [185]. (*left*) 3D plot of training data (black dots) and final fit (red mesh). (*center top*) Same as left most panel, but in index space. (*center bottom*) Percent residual error with respect to validation data (grey blocks) along with uniform (black) and gaussian (red) fits to error. The validation data were generated in the same manner as the training data. (*top right*) convergence of the L^2 norm during iterative refinement. (*bottom right*) Same as top right, but on log scale, where ϵ_0 is the value of ϵ at the final k^{th} iteration of refinement.

Fig. 5.1 shows the application of GMVR to this fiducial dataset. The central bottom panel of Fig. 5.1 displays the distribution of percentage residuals with respect to validation data generated in the same manner as training data. A gaussian fit to the fractional residuals is displayed for comparison. In particular, despite the uniform nature of the underlying noise distribution, a biased fit will often have residuals that are approximately gaussian. That is not the case here, and the uniformly random noise distribution is approximately recovered. Moreover, when considering many noise realizations to generate validation data, the sample noise and residuals have an average correlation of 99.46%.

Parameter	Training Value	Modelled Value	Difference
μ	50.0	49.9915	0.0171 %
a_0	1.1	1.1374	3.4002 %
a_1	0.2	0.2000	0.0000 %
a_2	0.5	0.5068	1.36784 %
a_3	1.0	1.0063	0.6300 %
$1/\sigma$	0.9	0.9375	4.1612 %
b_1/σ	1.0	0.9941	0.5906 %
b_2/σ	1.0	1.0000	0.0000 %

Table 5.1: Summary of recovered model parameters for GMVR toy problem.

The right top and bottom panels of Fig. 5.1 show the convergence of the iterative refinement stage of Alg. (4) (i.e. its while-loop). Here it is demonstrated that GMVR converges in a way that is approximately exponential, owing to the underlying analytic nature of the training data. Table 5.1 demonstrates the accurate recovery of the underlying model parameters with GMVR. Note that the initial output of GMVR contains terms in the numerator which correspond to the addition of a constant to the overall model, thus correcting for the difference between the offset parameter, μ, and the true, but arbitrary, mean of the dataset. Table 5.1 presents recovered model parameters after this effect has been accounted for with simple algebraic manipulation.

In this rudimentary example case, GMVR correctly recovers the functional form of the input data, and accurately recovers the correct values of model parameters. But, in general, GMVR and related techniques, having no knowledge of the underlying noise distribution, will attempt to model minor correlations and offsets within the training data's noise. However, the utility of GMVR has been demonstrated in a relatively ideal usage case where the underlying function is rational, and the training data is only weakly contaminated with noise.

5.3 Discussion

New algorithms have been developed upon previous techniques for the linear and pseudo-linear modelling of low noise data. In particular, the GMVP algorithm performs multivariate polynomial modelling of real and complex valued scalar functions with no inherent limitation on the number of domain parameters. The GMVR algorithm does the same with multivariate rational functions. When applied to the modelling of analytically computed quantities, both algorithms perform extremely well in producing accurate and precise representations of training data, suggesting extended applicability of GMVR and GMVP to similar problems.

Treating a toy problem with GMVR demonstrates its ability to faithfully recover underlying model parameters for a plausible dataset. This treatment also demonstrates the convergence of the algorithm's greedy phase with increasing iterations, as well as the convergence of an underlying iterative refinement phase (Eq. (5.13)).

Both GMVP and GMVR may be used to automatically determine the functional form and

model for a given dataset that is expected to be respectively polynomial or rational. An alternative use-strategy is to use either `GMVP` or `GMVR` to determine a fitting ansatz for individual cases (e.g. individual QNMs as in [184]), and then use these results to develop a single ansatz for all cases.

While `GMVR` and `GMVP` show promise in the cases shown here, in their presented rudimentary form, both posses a number of limitations. If given sufficiently dense training data, neither currently performs cross-validation. And perhaps most notably, neither method directly accounts for information about the noise distribution within the training data. As such, the methods presented are recommended primarily for datasets where noise is very small or negligible. Nevertheless, the `GMVR` toy problem demonstrates `GMVR`'s ability to handle moderately noisy training data, suggesting current applicability to a variety of problems where polynomial regression is insufficient. A recent study [246] has also demonstrated that these methods remain very competitive with more complex approaches such as Gaussian process regression and artificial neural networks.

Of relevance to current and future GW science, the `GMVP` has been used to model QNM frequencies and `GMVR` has been used to model the Spherical-spheroidal harmonic mixing coefficients [184]. In particular the new model for QNM frequencies was used in the construction of `PhenomNSBH` in Chapter. 2. Beyond this thesis these QNM models have aided (e.g. Refs.[91, 183, 186]), and are expected to continue aiding the development and implementation of GW signal models.

Chapter 6

Continuous integration of the LIGO numerical relativity repository

6.1 Introduction

NR has been shown to be very useful in different areas of GW research. It has been essential to the tuning of all the GW models used for parameter estimation of observations in the first and second observing runs of the advanced gravitational-wave detector network (see Sec. V in [19]). In Chapter 2 NR was used in the construction of the underlying BBH and NSBH models. In Chapter 3 a catalogue of more NR simulations was presented with the primary purpose to support development of future GW models. These demonstrate the significant indirect impact NR has for end users of waveform models. There are also direct applications NR has to the wider GW community, notably in injection studies.

Today most publicly available NR data sets are published in catalogues typically grouped by project or research group that use a specific NR code. A data set for a single simulation also typically contains much more information than is necessary for GW injection studies and the relevant components have to be processed to generate injections, which requires significant effort for GW researchers not working with NR on a day-to-day basis.

The NINJA [57] and NINJA-2 [37] projects were collaborations between many research groups using several different NR codes to study the sensitivity of GW search and parameter estimation algorithms. NR waveforms were contributed from each project member group. As part of this effort, LALSuite, described in Sec. 2.1, had new modules implemented to support the generation of GW injections from these data sets. The format for the NR data sets used by the NINJA-2 project was published separately [82] to help focus the disparate structures of the many NR groups producing simulations to extract GW information.

More recently this data format has been improved in several ways [241]. Improvements have included data compression support for GW modes that was explicitly added using a spline interpolation method [133] to enable smaller file sizes. `hdf5` was also specified as the new container format. An overhaul of the methods used to inject NR waveforms with LALSuite also accompanied the specification. Critically the new implementation handled

the construction of the detector response using LALSuite conventions. These improvements now mean that NR waveforms can be used as a *discrete* GW approximant just like any other GW model implemented in LALSimulation, which is the module of LALSuite where GW models are implemented.

While this infrastructure made injection studies easier there was still a lack of NR data appropriately formatted to be used with this infrastructure. To solve this problem a new LVC Numerical Relativity (LVCNR) repository was established [209] that would be a central location where NR data sets that satisfied the new NR specification [241] could be stored for future use. This chapter provides details of the LVCNR repository.

In Sec. 6.2 several examples of using the LVCNR repository will be described. Issues that arose in these use cases with the original LVCNR will be highlighted. In Sec. 6.3 updates to the LVCNR repository are described that improve the end user experience and add continuous validation of candidate data sets requested to be added to the repository. The focus of these updates is to address the issues of the first implementation of the LVCNR repository. In Sec. 6.4 the current status of the LVCNR repository will be discussed and how future updates to the Git version control system can be incorporated to further improve the user experience of the LVCNR repository.

6.2 Workflow analysis

The first implementation of the LVCNR repository was a Git repository enhanced by `git-annex` [149]. The `git-annex` extension allows for files to be managed by Git without actually checking the files content into Git, which was beneficial for several reasons. NR `hdf5` files following the NR format specification were relativity small (typically less than 20MB) but still larger than typical files managed by Git, and they were also binary files. Committing many such files to Git can dramatically slow down Git operations (for example `clone`, `checkout`, and `status`). `git-annex` solves this problem by only committing checksums and associated metadata of files managed by `git-annex` and then storing copies of the content in a separate remote location for others to access. It also allowed for a subset of files to have their contents checked out such that not all `hdf5` files in the LVCNR repository had to reside on the local storage in the working directory of a clone of the repository which might otherwise be prohibitive to end users dues to space constraints. For reference the current LVCNR repository is over 30GB in size.

While this first implementation of the repository solved the most immediate issues of managing a large set of binary files with Git, issues with this implementation became apparent over time. Some files added to the repository did not actually follow the NR specification which meant they would not work with the injection infrastructure. `git-annex` also required a separate server program along side a standard Git server which was only available on the Cardiff Cluster at the time which was not designed to support large volumes of traffic. This often lead to failed `clone`, `pull` and `push` operations when operating on the repository. `git-annex` also required a new set of commands along side the standard Git commands

to be able to manage files which did cause apprehension to commit files to the LVCNR repository, often with months between new commits from the community.

A second implementation of the LVCNR repository was deployed for the second observing run of the LVC detectors. Considering the benefits that `git-annex` provided and the issues that still had to be addressed the first part of planning a second implementation was to understand typical *use cases* of the repository.

A *use case* is a simple software development template that can be filled in with a common task an end user of a piece of software technology might perform. From use cases software requirements can then be distilled knowing that the requirements enable common usage patterns. Several key use cases of the LVCNR repository are presented in Sec. 6.2.1. Where possible references to specific software technology should be excluded from individual use cases to allow for more flexibility as the software requirements are designed based on all the use cases. However one exception for the LVCNR repository was that Git had already been chosen to be the main technology used for the second implementation as it had become the primary version control system used by the LVC. As such the use cases presented in Sec. 6.2.1 were permitted to make explicit reference to Git and common Git workflow patterns.

6.2.1 Use cases

A primary use case is to allow NR authors to add new resources to the LVCNR repository. Adding new resources should follow the standard fork-branch-merge workflow model already used by many software projects.

Use case name	**I. Add `hdf5` files**	
Goal in Context	Add new LVCNR `hdf5` simulation to the central upstream repository	
Main Success Scenario	**Step**	**Action**
	1	Commit LVCNR data to local repository clone
	2	Push local commits to remote repository fork
	3	Open merge request
	4	Wait for files to be validated
	5	Files merged into central upstream repository

Accessing LVCNR data is also critical for NR consumer end users. Often end users will only need one data set. It should not be necessary to clone the repository to acquire one or a small number of `hdf5` data sets.

Use case name	**II. Get one `hdf5` file**	
Goal in Context	Get a single LVCNR `hdf5` simulation from the central repository	
Main Success Scenario	**Step**	**Action**
	1	Access the LVCNR repository without a clone
	2	Navigate to the target LVCNR `hdf5` file
	3	Download file directly

It is assumed that if you clone the repository without making any additional configuration to a local system that all the data committed to the repository will be downloaded to the local machine. However it should also be possible to clone the repository and restrict which data sets are downloaded to the local system of the end user.

Use case name	**III. Get many `hdf5` files**	
Goal in Context	Get many LVCNR `hdf5` simulations from the central repository without downloading all simulations	
Main Success Scenario	**Step**	**Action**
	1	Prepare system to prevent downloading of repository file
	2	Clone repository without downloading any files
	3	Selectively download files that are required

6.3 Solution

Based on the use cases presented in Sec. 6.2.1 a set of specification can be defined that will satisfy the main success scenarios for all of the uses cases,

- **Software development management web interface to the LVCNR repository**
  This will help satisfy steps 3 and 4 of use case I. Merge requests are typically performed through web interfaces so that several developers can review candidate changes. This will also contribute to steps 1–3 of use case II. All major web interfaces for Git repositories enable files to be downloaded directly without having to clone the repository.

- **Binary file manager for Git beyond the core features**
  This will help satisfy step 1 of use case I. As discussed in Sec. 6.2 standard handling of binary files by Git can lead to poor performance. This will also help satisfy steps 1–3 of use case III. Standard Git features do not provide the necessary functionality to achieve use case III.

- **Program to validate candidate `hdf5` simulations against the specification**
  This will help satisfy step 4 of use case I. Validating simulation needs a consistent method that can be repeated by many people.

- **Automated instancing of computational environments to run validation**
  This will help satisfy step 4 of use case I. Executing validation programs manually will not be sustainable, and should conform with standard practice of automated testing of software programs.

For the rest of Sec. 6.3 the improvements that were made in the second implementation of the LVCNR repository to satisfy these requirements will be discussed.

6.3.1 Migration to LVC GitLab instance

The LVC GitLab instance was the natural choice to use as it had become the primary software development management platform for the LVC. It includes a web interface component that allows for access to the LVCNR repository.

6.3.2 Replace `git-annex` with Git LFS

There was friction for all types of end users when performing operations with `git-annex`. While the appropriate choice at the time of the first implementation it was not appropriate for the second implementation. The LVC GitLab instance also does not support `git-annex`.

Git Large File Support (LFS) [134] was an alternative choice. Similar to `git-annex`, Git LFS replaces large files with text pointers inside Git and stores the files' contents on a remote server. While there is no expectation that all users would have used Git LFS previously, it was a better supported technology than `git-annex` and the set of command line operations that are needed to manage binary files with Git LFS is smaller; once a file is tracked by Git LFS only normal Git operations are needed, for example `push` and `pull` operations. As it was supported by GitLab this also meant that the LVC GitLab instance also had support for Git LFS which made it an ideal replacement for `git-annex`.

6.3.3 Continuous validation using continuous integration infrastructure

Continuous integration (CI) is the software development practice of regularly integrating different distributed working copies of modified software into a shared central copy. CI has become synonymous with the instancing of computational environments to run automated unit and integration tests of code as commits are made to software repositories before changes are integrated. These computational instances have continually been enhanced to make them usable for far more than code tests, for example they have been used by the LVC to automatically compile PDF files of collaboration research papers as changes are made, and automatically deploy builds of LALSuite as release tags are authored.

The LVC GitLab instance has a very well integrated CI framework. As such this framework was used to perform automatic validation as commits were made on branches to any fork of the central LVCNR repository. The python package `lvcnrpy` [121] was created to perform consistent validation of simulations against the specification which could also be used locally. Each CI instance automatically reports if new or updated `hdf5` files meet the specifications and appropriate action can then be taken to accept or reject any candidate merge requests.

6.4 Discussion

Since the introduction of the second implementation of the LVCNR repository the number of `hdf5` data sets has tripled, now with 1047 data sets which all conform to the NR `hdf5`

specification. This repository has been used as a source of data for several projects including for the intermediate mass black hole binaries (IMBHB) NR injection study to estimate the upper limits on IMBHB merger rates in the first and second observing runs of the Advanced LIGO and Virgo network [22].

Fig. 6.1 presents the distribution of the properties of the simulations currently in the repository. Overall the low mass ratio region of parameter space is covered well. However moderate to high mass ratio and spin are still not well covered. There are several clusters of simulations produced for targeted NR projects, in particular for GW150914 [9] and GW170104 [12]. The repository does not yet include the simulations described in Chapter 3, however these will be added when that work is published.

The second implementation of the LVCNR repository has been successful in its purpose to provide easy access to a large collection of NR simulations ready to be used in GW analysis. However there are still ways in which this repository can be improved in future implementations.

When initially planning the second implementation LVCNR repository Git LFS was the technology recommended by GitHub and GitLab to manage large binary files [253, 137]. However the features of the core Git program have improved since then, all uses cases presented in Sec. 6.2.1 can now be satisfied through a combination of partial cloning and spare checkouts which are core Git features [258, 229]. This will reduce friction for end users by no longer requiring the installation of an additional program and not imposing the need to use particular non-standard workflow commands to operate on the repository.

Modular validation should also be implemented. Every CI instance has to clone the entire repository into its working directory. This means the runtime of CI jobs are dependant on the size of the repository and not on the number of files added or modified. This will become prohibitive as the repository grows bigger. This can be solved by decoupling the continuous validation from the repository itself. Instead CI instances in an auxiliary repository can be triggered by new merge requests and commits added to those merge requests, which will provide the necessary control to only download the new or modified `hdf5` files. This will ensure use case I is still satisfied and greatly reduce the required validation time.

The focus on this implementation has been data validation, and not on data quality. One example of data quality issues appeared during testing of the LVCNR repository. Several data sets were manually identified to have mode data scaled incorrectly. The current system assumes that NR authors have checked the quality of the data but future systems could implement basic quality checks to ensure the integrity of the repository without the need to assume data quality.

Finally, while there was a candidate implementation of a web based search interface for the repository, this was not maintained and as such rarely used. A search interface could be added to the repository which would increase its accessibility, however it is critical that this be integrated in the same way as any continuous validation to ensure it remains useful in contrast to the previous candidate search interface. These four improvements will be left for future work.

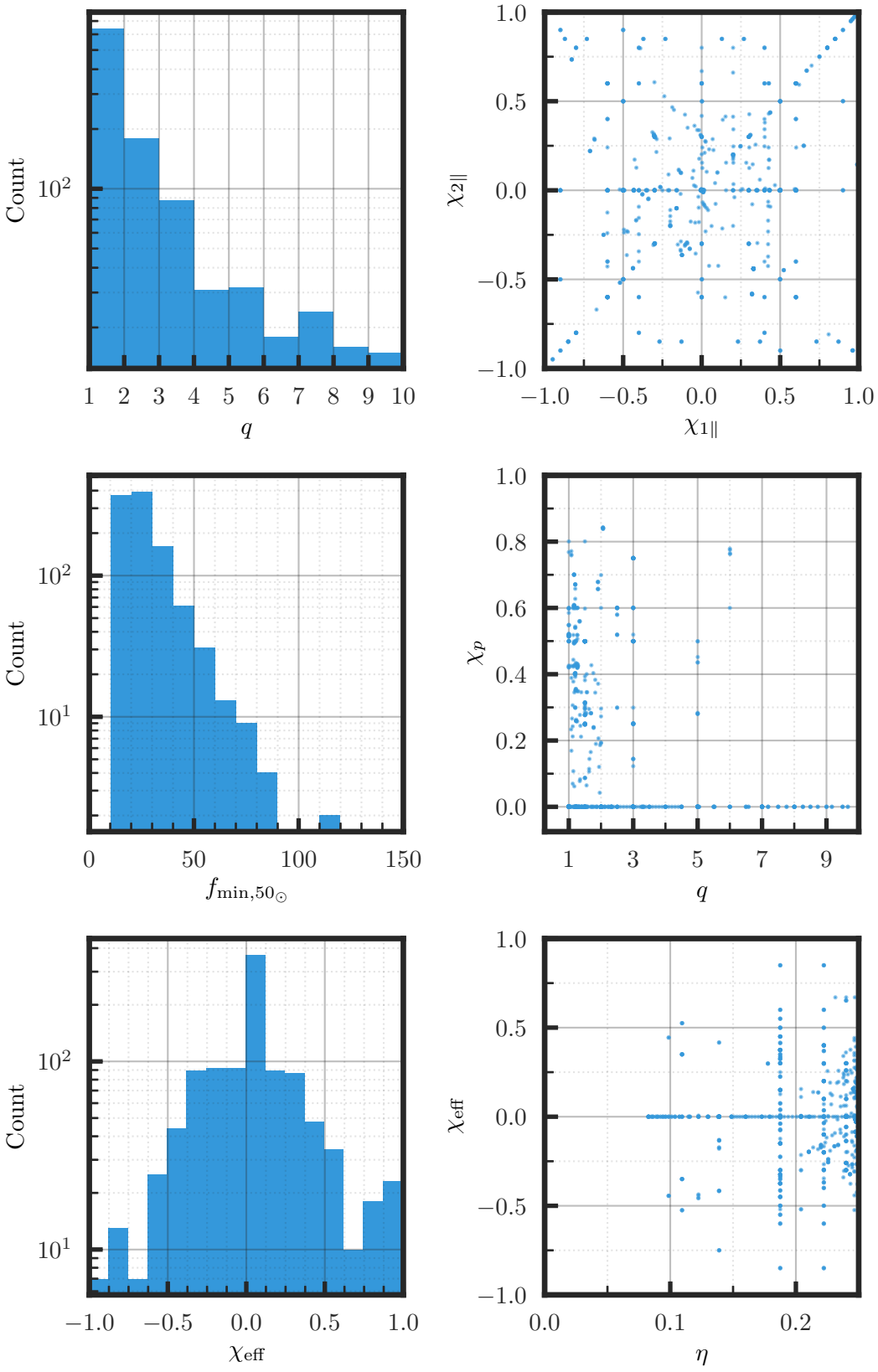

Figure 6.1: Distribution of the properties of the NR data sets currently committed to the LVCNR repository.

Chapter 7

Web-based analysis of numerical relativity simulations

7.1 Introduction

In Chapter 3 a comprehensive new set of NR simulations were introduced that spanned a large portion of the precessing parameter space. This has been the largest systematic campaign to perform BAM simulations currently conducted. Work is still continuing to expand the catalogue of simulations.

Early on in the process of that project it became clear that there were issues around data analysis pipelines. One example was different members of the project using different methods to estimate eccentricity and in some extreme instance eccentricity requirements were exceeded by an order of magnitude. In general new project members did not have the experience to know what types of checks to perform, and experienced users had highly curated methods that were not always compatible with the requirements of the simulation campaign. It is critical that data analysis pipelines for large scale simulation campaigns with multiple project members are consistent and reproducible.

These types of collaboration issues often appear in scientific research. Many systems have been developed to solve issues like these, each with different feature sets adapted for the problems they aim to solve. For example, Aladin Sky Atlas [76, 70] provides direct visualisation of large astronomical datasets stored on servers around the world, Einstein@Home [168, 45] uses the BIONIC system [49] to create a virtual computational grid from hundreds of thousands of volunteered computers to search for signals from spinning neutron stars, and the Astrophysics Simulation Collaboratory Portal [75] provides an integrated framework to manage simulations on computational grids through a web-based interface and includes features to monitor and visualise simulations.

In order to address this current problem a new web-based service was created called `bam-guardian` to perform an analysis of a requested BAM simulation. The intention was to create something simple enough that to repeat an analysis all that would be required is to visit a web app and press a button. In Sec. 7.2.1 a typical workflow for performing a single

BAM simulations will be described. Sec. 7.2.2 will consider several use cases for such a service. In Sec. 7.3 the solution will be presented. In Sec. 7.4 ways in which the web-based analysis service can be improved will be discussed.

7.2 Workflow analysis

7.2.1 Simulation workflow

When performing a single BAM simulation there are several different stages that have to be executed. These include identifying initial momenta, constructing initial data, and generating grid configurations which all have to happen before a simulation is started. Once these resources have been prepared, the simulation is performed on a high performance computing (HPC) system, typically under a scheduler such that the simulation needs to be restarted every few days. If the simulation is an exploratory run to try to identify optimal momenta then this entire process may need to be repeated several times. Several of these component processes have been discussed in detail in Chapter 3.

A schematic representation of the full workflow for a single BAM simulation is presented in Fig. 7.1. This includes moments during a simulation workflow where there is a need for user choices indicated by the blue diamonds. Also indicated on the diagram by $*$ symbols are moments during the workflow where the user may want to generate an analysis of the simulation. In the context of this problem, an analysis of a BAM simulation is a set of diagnostic plots that visualise the history of the simulation, dynamics that can be presented, calculates estimates of the eccentricity, and any other diagnostic tool that is useful for a BAM simulation.

A typical pattern is for a long running program to have diagnostic plots generated once the program has finished. However one of the requirements identified early was to make any analysis capable of being executed on demand and not have to wait for the simulation to finish a cycle. There was also a desire to be able to share diagnostic plots with others so that they could be discussed. Inspired by the results web pages generated for LALInference [275] jobs, the intention was to create diagnostic plots that could be accessed through a web interface. However user accessible directories from which diagnostic plots could be served over the web did not exist on all the HPC systems BAM is currently used on. Based on these early observations several use cases were considered.

7.2.2 Use cases

A primary used case is for users to execute programs that manipulate data over an Secure Shell (SSH) session. This might be as simple as initiating an SSH session and executing commands on a remote machine, or it could mean establishing a local SSH mount of remote data for processing. The specific details of these different types of SSH based analysis have been encapsulated in use case I.

Use case name	**I. Command line interface request**	
Goal in Context	The expected output from the CLI program is provided for the user	
Main Success Scenario	**Step**	**Action**
	1	End user initial SSH session with relevant server
	2	Sever authenticates user
	3	User executes CLI action
	4	User observes successful program execution
	5	User terminates SSH session

In many situations, the same remote machines are accessed and the same programs are executed over and over again. This type of use case can have some, if not all of its constituent parts executed automatically, making sure to execute parts in the order of which parts depend on others. All of the programs in this workflow of dependent parts can be represented as a single composite application, where the inputs to the application are the union of all user input parameters of the constituent parts. In this representation, it does not matter if the application is executed on a local machine or a remote machine, as long as there is a mechanism to provide inputs. Additionally the user who provides the inputs does not have to be responsible for managing the application. This execution pattern is the same as a very common software architecture style called Representational State Transfer (REST) [125]. In this context the application inputs are interpreted as the *application state* which is transferred from the user to the application, the application is executed, and any relevant information returned to the user. This is an abstract idea, but a very common implementation of a REST application programming interface (API) is using a Hypertext Transfer Protocol (HTTP) request. The HTTP request provides the mechanism for a user to provide inputs to the application. A machine that serves a REST API responds to a specific set of HTTP requests, also know as *endpoints*, where the application inputs are mapped to the *parameters* of the HTTP request. Requests can be dispatched to the machine, which could be local or remote, that will then execute the application, and provide results. GraceDB [179] is an example of an application used in research settings that provides a HTTP REST API. There are many ways that this composite application could be encapsulated, however the prevalence of existing REST APIs outside of research settings could provide many benefits down the line. Use case I can be elevated to use a REST API. This is presented in use case II.

Most users will not be familiar with how to make a HTTP request with a payload of data. However a natural step further beyond a HTTP request is to make that request through a web interface. With a simple REST API wrapped with a web interface commonly repeated use processes can be replaced with a single button press. A simple web request example is presented in use case III

A use case diagram is presented in Fig. 7.2. This does not provide as much detail as the tabular based uses cases, however it does presented a good overview of the types of specific

Use case name	**II. HTTP request**	
Goal in Context	The user receives a HTTP payload with expected output or success confirmation that action was performed on remote server	
Main Success Scenario	**Step**	**Action**
	1	End user queries a HTTP endpoint
	2	A command line interface request is made
	Include::Command line interface request	
	3	User receives HTTP payload from server

Use case name	**III. Web request**	
Goal in Context	The web interface is updated with expected output or user receives email with links to generated resources	
Main Success Scenario	**Step**	**Action**
	1	End user triggers event in web interface
	2	A HTTP request is made
	Include::HTTP request	
	3	Web interface is updated or email sent to user

tasks that a user will want to perform based on the workflow discussed in Sec. 7.2.1. In particular a key CLI request that would need to be handled is to generate an analysis of a BAM simulation.

7.3 Solution

The primary actors in this system are end users who are not developers of any of these tools, and are not required to have any specific knowledge of how the tools are implemented. While the use cases were not intended to be informed by candidate implementations, a natural identification of use cases formed the same hierarchy that mirrors and implementation, command line interface tools are build, command line interface tools are exposed through HTTP endpoints and finally HTTP endpoints are wrapped with front end web interfaces.

One of the primary implementation objectives was to minimise user installation requirements, and wherever possible eliminate them entirely. A second implementation objective was to minimise the amount of time and precision required by an end user to carry out a use case.

The final implementation presented a simple web interface to the user as displayed in Fig. 7.3. The user would put in only the strictly necessary parameters for their simulation that is or was running. Once that web request has been made it is stored in the users browsers local storage so that subsequent requests can be made at a press of a button. The HTTP request is then made the a REST server. In this case it turns out that the CI infrastructure used in Chapter 6 also exposes a configurable REST API. Analysis programs can therefore be deployed to the CI infrastructure and executed when requests are made. The analysis is

then performed and that is sent to a separate web server for storage. An example analysis page can be see in Fig. 7.4.A schematic representation of the full implemented solution is presented in Fig. 7.5.

7.4 Discussion

In this chapter a web-based service for analysing `BAM` simulations was presented. While the context of NR is not widely applicable to others, the software design pattern is. Modular and distributed analysis systems can be applied in and context where data visualisation is required.

One of the key features of `bam-guardian` is modularity. The dotted lines represent physical systems. Any one of those systems can be replaced or swapped out, as long as the lines connecting the different systems maintain a the same interface signatures, then everything will still continue to function. For example `BAM` is now used on three different systems. In order to perform analysis for simulations on any one of those systems simply requires a remote address and SSH key pair and nothing else needs to be set up. New systems can be added and removed as required.

This first version of the `bam-guardian` service has been used over 5000 times to analyse `BAM` simulations. It is possible for the analysis to fail. Currently there is no way for an end user to know if an analysis has failed, it will do so silently. Future versions should provide a mechanism for users to check the progress of an analysis, or send an email if it fails. There is also no interface to browse past analysis pages. Having such an interface would not only benefit current users but future users would quickly be able to investigate past simulations. This is also planned for future versions.

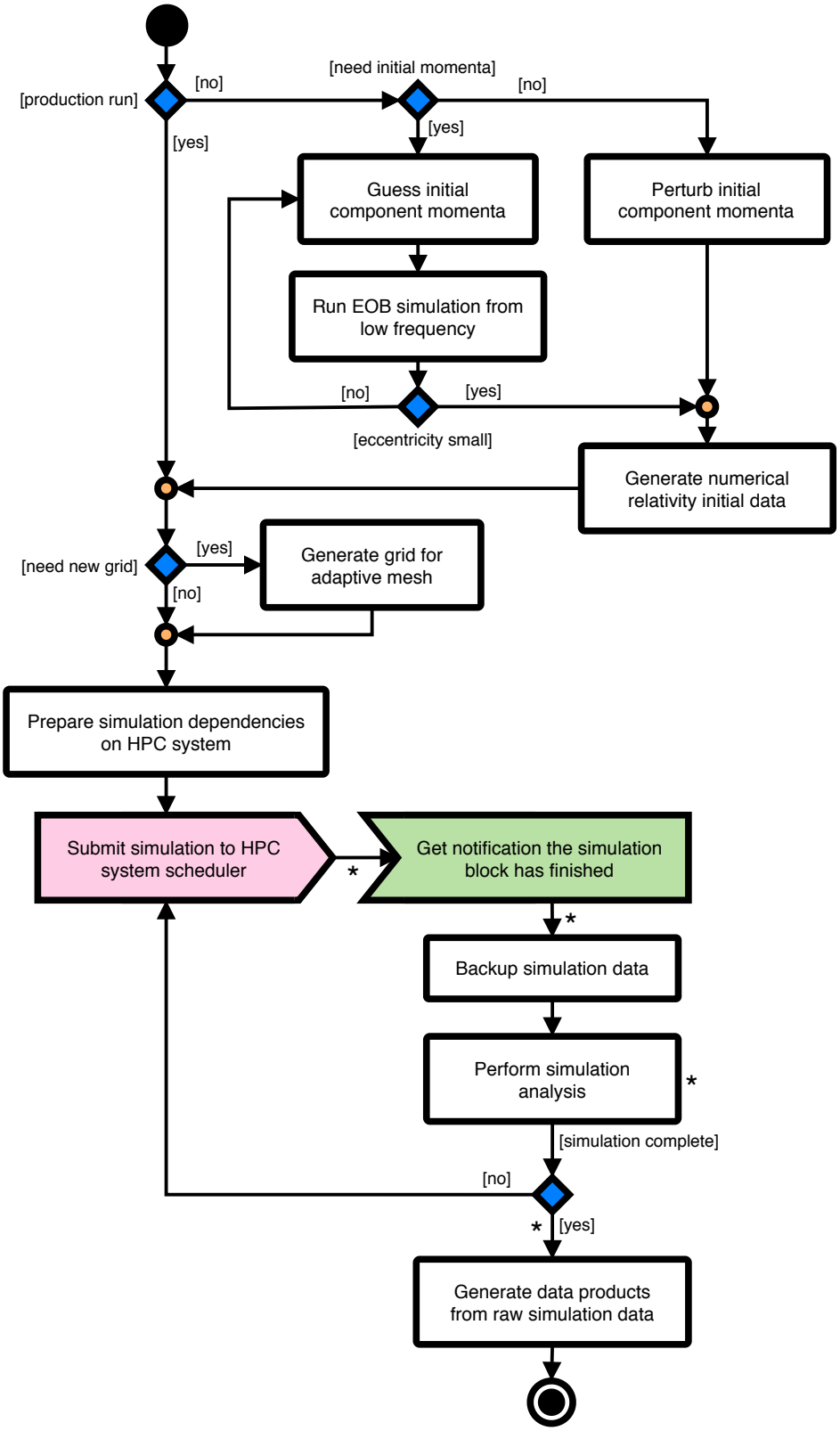

Figure 7.1: Schematic representation of a general binary black hole simulation performed with `BAM`. This workflow may need to be repeated several times if a simulation requires manual iterations of component momenta to reduce eccentricity in the quasi-circular orbits of the binary system. Connections and blocks marked with * indicate times when simulation analysis may be required.

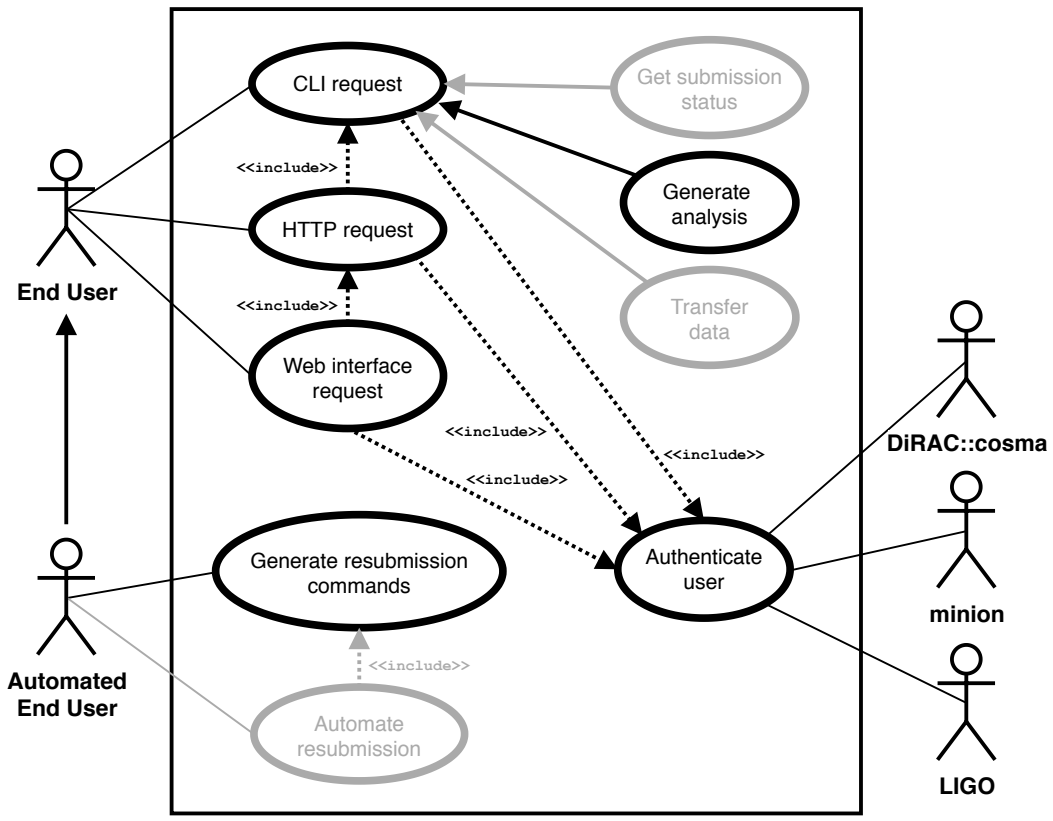

Figure 7.2: Use case diagram for a candidate for BAM data analysis service. There are several actors, which includes end users who execute requests, and administrators and machines who are responsible for managing and authenticating end users. Actions in light gray are candidate features for future versions of this BAM data analysis service however have not been implemented in the current version.

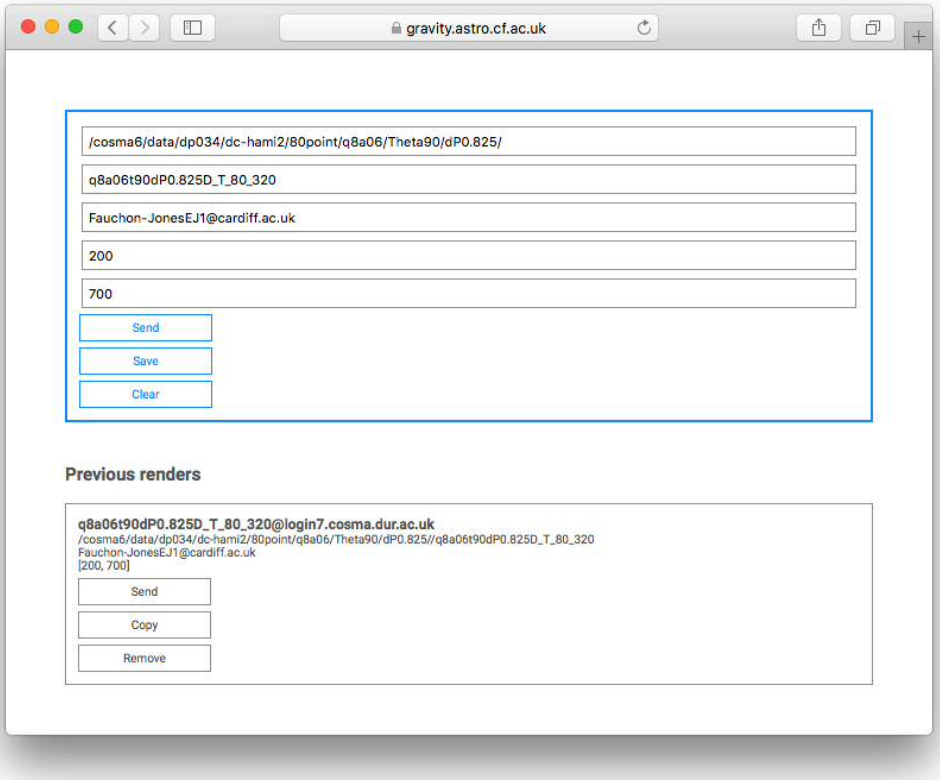

Figure 7.3: Screen shot of the web-app interface to `bam-guardian`.

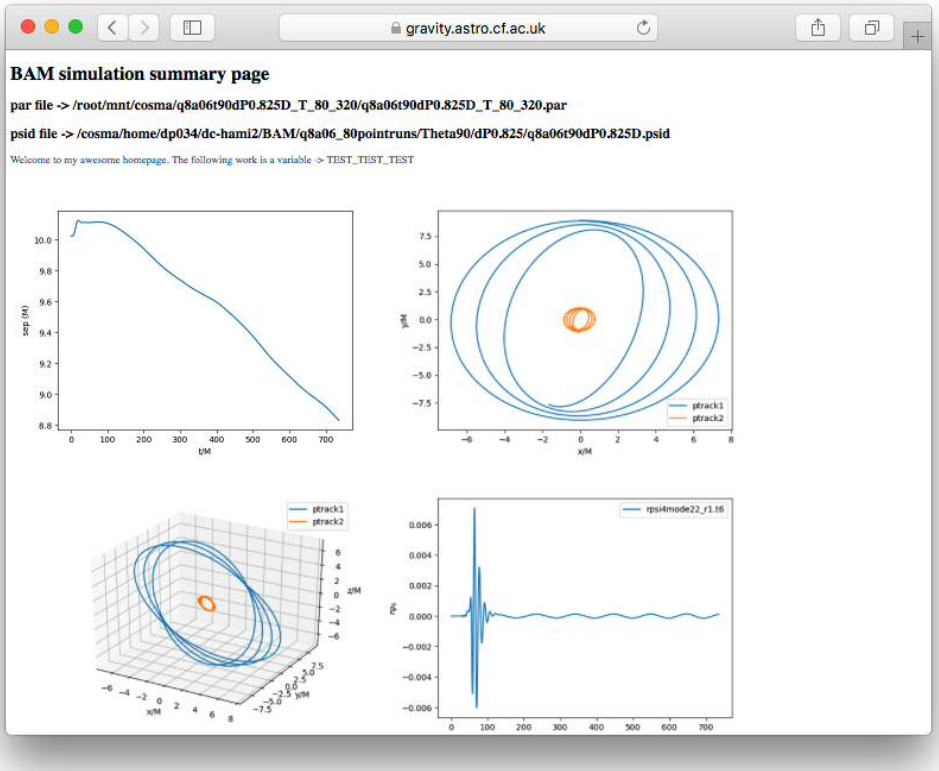

Figure 7.4: Screen shot of an analysis page generated by `bam-guardian`.

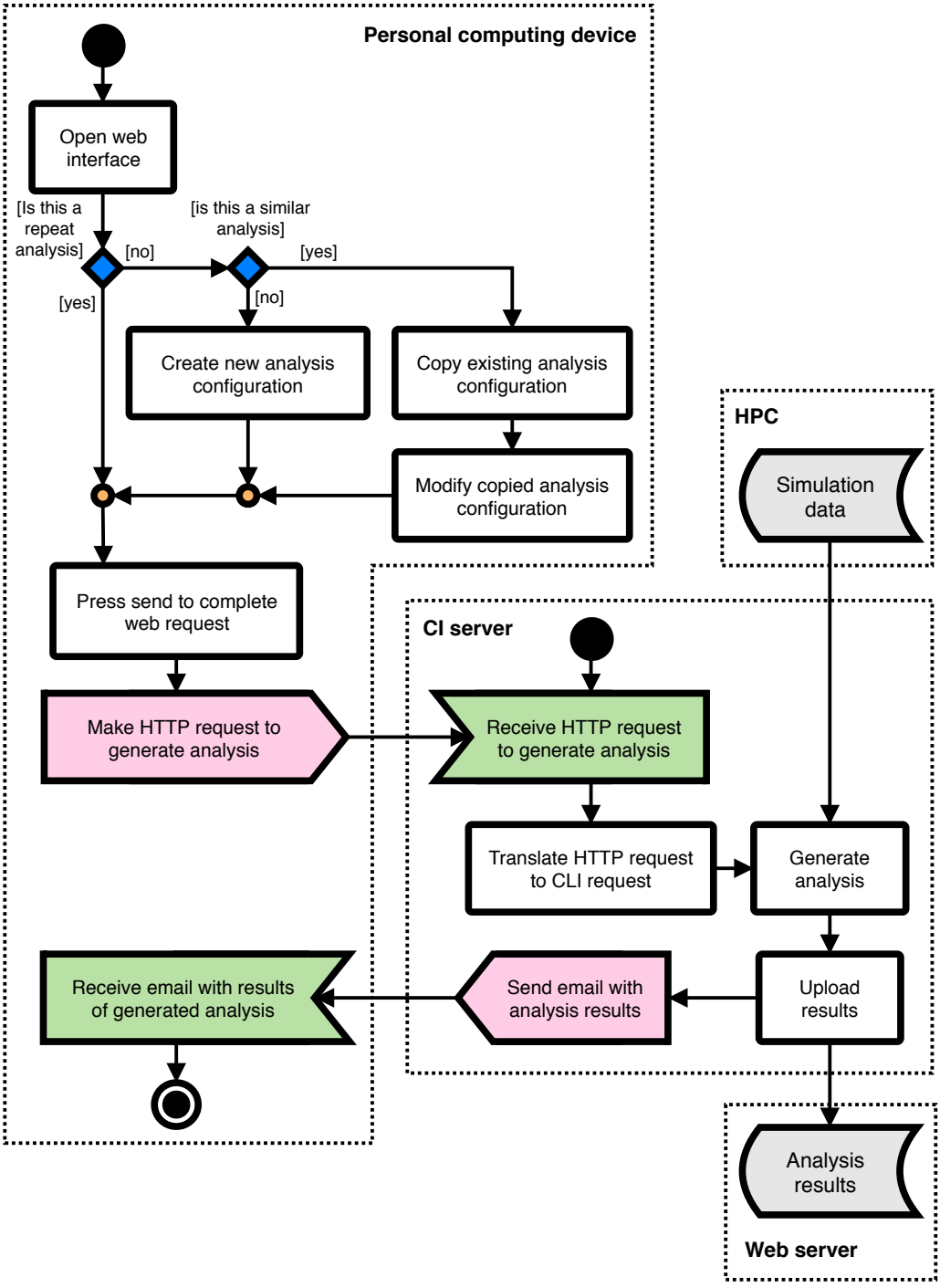

Figure 7.5: Schematic representation of the implemented web-based service to perform analysis of a `BAM` simulation.

Bibliography

[1] LIGO sensitivity curves. LIGO-P1200087-v42, September 2017.

[2] J. Aasi et al. Parameter estimation for compact binary coalescence signals with the first generation gravitational-wave detector network. *Phys. Rev.*, D88:062001, 2013, 1304.1775.

[3] J. Aasi et al. Advanced LIGO. *Class. Quant. Grav.*, 32:074001, 2015, 1411.4547.

[4] B. P. Abbott et al. LIGO: The Laser interferometer gravitational-wave observatory. *Rept. Prog. Phys.*, 72:076901, 2009, 0711.3041.

[5] B. P. Abbott et al. Binary Black Hole Mergers in the first Advanced LIGO Observing Run. *Phys. Rev.*, X6(4):041015, 2016, 1606.04856. [erratum: Phys. Rev.X8,no.3,039903(2018)].

[6] B. P. Abbott et al. Characterization of transient noise in Advanced LIGO relevant to gravitational wave signal GW150914. *Class. Quant. Grav.*, 33(13):134001, 2016, 1602.03844.

[7] B. P. Abbott et al. Directly comparing GW150914 with numerical solutions of Einstein's equations for binary black hole coalescence. *Phys. Rev.*, D94(6):064035, 2016, 1606.01262.

[8] B. P. Abbott et al. GW151226: Observation of Gravitational Waves from a 22-Solar-Mass Binary Black Hole Coalescence. *Phys. Rev. Lett.*, 116(24):241103, 2016, 1606.04855.

[9] B. P. Abbott et al. Observation of Gravitational Waves from a Binary Black Hole Merger. *Phys. Rev. Lett.*, 116(6):061102, 2016, 1602.03837.

[10] B. P. Abbott et al. Effects of waveform model systematics on the interpretation of GW150914. *Class. Quant. Grav.*, 34(10):104002, 2017, 1611.07531.

[11] B. P. Abbott et al. Exploring the Sensitivity of Next Generation Gravitational Wave Detectors. *Class. Quant. Grav.*, 34(4):044001, 2017, 1607.08697.

[12] B. P. Abbott et al. GW170104: Observation of a 50-Solar-Mass Binary Black Hole Coalescence at Redshift 0.2. *Phys. Rev. Lett.*, 118(22):221101, 2017, 1706.01812. [Erratum: Phys. Rev. Lett.121,no.12,129901(2018)].

[13] B. P. Abbott et al. Prospects for Observing and Localizing Gravitational-Wave Transients with Advanced LIGO, Advanced Virgo and KAGRA. *Living Rev. Rel.*, 21(1):3, 2018, 1304.0670.

[14] B. P. Abbott et al. A gravitational-wave measurement of the Hubble constant following the second observing run of Advanced LIGO and Virgo. 2019, 1908.06060.

[15] B. P. Abbott et al. All-sky search for continuous gravitational waves from isolated neutron stars using Advanced LIGO O2 data. *Phys. Rev.*, D100(2):024004, 2019, 1903.01901.

[16] B. P. Abbott et al. All-Sky Search for Short Gravitational-Wave Bursts in the Second Advanced LIGO and Advanced Virgo Run. *Phys. Rev.*, D100(2):024017, 2019, 1905.03457.

[17] B. P. Abbott et al. An Optically Targeted Search for Gravitational Waves emitted by Core-Collapse Supernovae during the First and Second Observing Runs of Advanced LIGO and Advanced Virgo. 2019, 1908.03584.

[18] B. P. Abbott et al. Binary Black Hole Population Properties Inferred from the First and Second Observing Runs of Advanced LIGO and Advanced Virgo. *Astrophys. J.*, 882(2):L24, 2019, 1811.12940.

[19] B. P. Abbott et al. GWTC-1: A Gravitational-Wave Transient Catalog of Compact Binary Mergers Observed by LIGO and Virgo during the First and Second Observing Runs. *Phys. Rev.*, X9(3):031040, 2019, 1811.12907.

[20] B. P. Abbott et al. Properties of the binary neutron star merger GW170817. *Phys. Rev.*, X9(1):011001, 2019, 1805.11579.

[21] B. P. Abbott et al. Search for gravitational-wave signals associated with gamma-ray bursts during the second observing run of Advanced LIGO and Advanced Virgo. *Astrophys. J.*, 886:75, 2019, 1907.01443.

[22] B. P. Abbott et al. Search for intermediate mass black hole binaries in the first and second observing runs of the Advanced LIGO and Virgo network. *Phys. Rev.*, D100(6):064064, 2019, 1906.08000.

[23] B. P. Abbott et al. Search for the isotropic stochastic background using data from Advanced LIGO's second observing run. *Phys. Rev.*, D100(6):061101, 2019, 1903.02886.

[24] B. P. Abbott et al. Tests of General Relativity with the Binary Black Hole Signals from the LIGO-Virgo Catalog GWTC-1. *Phys. Rev.*, D100(10):104036, 2019, 1903.04467.

[25] B. P. Abbott et al. A guide to LIGO-Virgo detector noise and extraction of transient gravitational-wave signals. *Class. Quant. Grav.*, 37(5):055002, 2020, 1908.11170.

[26] B. P. Abbott et al. GW190425: Observation of a Compact Binary Coalescence with Total Mass $\sim 3.4 M_{\odot}$. 2020, 2001.01761.

[27] M. Abernathy et al. Einstein gravitational wave Telescope conceptual design study. ET-0106C-10, Jun 2011.

[28] T. Accadia et al. Status of the virgo project. *Classical and Quantum Gravity*, 28(11):114002, May 2011.

[29] F. Acernese et al. Virgo status. *Classical and Quantum Gravity*, 25(18):184001, Sep 2008.

[30] F. Acernese et al. Advanced Virgo: a second-generation interferometric gravitational wave detector. *Class. Quant. Grav.*, 32(2):024001, 2015, 1408.3978.

[31] F. Acernese et al. Advanced Virgo Status. *J. Phys. Conf. Ser.*, 1342(1):012010, 2020.

[32] C. Affeldt, K. Danzmann, K. L. Dooley, H. Grote, M. Hewitson, S. Hild, J. Hough, J. Leong, H. Lück, M. Prijatelj, S. Rowan, A. Rüdiger, R. Schilling, R. Schnabel, E. Schreiber, B. Sorazu, K. A. Strain, H. Vahlbruch, B. Willke, W. Winkler, and H. Wittel. Advanced techniques in GEO 600. *Classical and Quantum Gravity*, 31(22):224002, Nov 2014.

[33] P. Ajith, S. Babak, Y. Chen, M. Hewitson, B. Krishnan, A. M. Sintes, J. T. Whelan, B. Brügmann, P. Diener, N. Dorband, J. Gonzalez, M. Hannam, S. Husa, D. Pollney, L. Rezzolla, L. Santamaría, U. Sperhake, and J. Thornburg. Template bank for gravitational waveforms from coalescing binary black holes: Nonspinning binaries. *Phys. Rev. D*, 77:104017, May 2008, 0710.2335.

[34] P. Ajith et al. Phenomenological template family for black-hole coalescence waveforms. *Class. Quant. Grav.*, 24:S689–S700, 2007, 0704.3764.

[35] P. Ajith et al. A Template bank for gravitational waveforms from coalescing binary black holes. I. Non-spinning binaries. *Phys. Rev.*, D77:104017, 2008, 0710.2335. [Erratum: Phys. Rev.D79,129901(2009)].

[36] P. Ajith et al. Inspiral-merger-ringdown waveforms for black-hole binaries with non-precessing spins. *Phys. Rev. Lett.*, 106:241101, 2011, 0909.2867.

[37] P. Ajith et al. The NINJA-2 catalog of hybrid post-Newtonian/numerical-relativity waveforms for non-precessing black-hole binaries. *Class. Quant. Grav.*, 29:124001, 2012, 1201.5319. [Erratum: Class. Quant. Grav.30,199401(2013)].

[38] M. Alcubierre. *Introduction to 3+1 Numerical Relativity*. International Series of Monogr. Oxford University Press, 2008.

[39] M. Alcubierre, G. Allen, B. Bruegmann, T. Dramlitsch, J. A. Font, P. Papadopoulos, E. Seidel, N. Stergioulas, W.-M. Suen, and R. Takahashi. Towards a stable numerical evolution of strongly gravitating systems in general relativity: The Conformal treatments. *Phys. Rev.*, D62:044034, 2000, gr-qc/0003071.

[40] M. Alcubierre, G. Allen, B. Bruegmann, E. Seidel, and W.-M. Suen. Towards an understanding of the stability properties of the (3+1) evolution equations in General Relativity. *Phys. Rev.*, D62:124011, 2000, gr-qc/9908079.

[41] M. Alcubierre, S. Brandt, B. Bruegmann, C. Gundlach, J. Masso, E. Seidel, and P. Walker. Test beds and applications for apparent horizon finders in numerical relativity. *Class. Quant. Grav.*, 17:2159–2190, 2000, gr-qc/9809004.

[42] M. Alcubierre and B. Bruegmann. Simple excision of a black hole in (3+1)-numerical relativity. *Phys. Rev.*, D63:104006, 2001, gr-qc/0008067.

[43] M. Alcubierre, B. Bruegmann, P. Diener, M. Koppitz, D. Pollney, E. Seidel, and R. Takahashi. Gauge conditions for long term numerical black hole evolutions without excision. *Phys. Rev.*, D67:084023, 2003, gr-qc/0206072.

[44] B. Allen, W. G. Anderson, P. R. Brady, D. A. Brown, and J. D. E. Creighton. FINDCHIRP: An Algorithm for detection of gravitational waves from inspiraling compact binaries. *Phys. Rev.*, D85:122006, 2012, gr-qc/0509116.

[45] B. Allen, B. Knispel, J. M. Cordes, J. S. Deneva, J. W. T. Hessels, D. Anderson, C. Aulbert, O. Bock, A. Brazier, S. Chatterjee, P. B. Demorest, H. B. Eggenstein, H. Fehrmann, E. V. Gotthelf, D. Hammer, V. M. Kaspi, M. Kramer, A. G. Lyne, B. Machenschalk, M. A. McLaughlin, C. Messenger, H. J. Pletsch, S. M. Ransom, I. H. Stairs, B. W. Stappers, N. D. R. Bhat, S. Bogdanov, F. Camilo, D. J. Champion, F. Crawford, G. Desvignes, P. C. C. Freire, G. Heald, F. A. Jenet, P. Lazarus, K. J. Lee, J. van Leeuwen, R. Lynch, M. A. Papa, R. Prix, R. Rosen, P. Scholz, X. Siemens, K. Stovall, A. Venkataraman, and W. Zhu. The Einstein@Home Search for Radio Pulsars and PSR J2007+2722 Discovery. ApJ, 773(2):91, Aug. 2013, 1303.0028.

[46] D. S. and. Status of the LIGO detectors. *Classical and Quantum Gravity*, 25(11):114041, May 2008.

[47] G. M. H. and. Advanced LIGO: the next generation of gravitational wave detectors. *Classical and Quantum Gravity*, 27(8):084006, Apr 2010.

[48] H. G. and. The status of GEO 600. *Classical and Quantum Gravity*, 25(11):114043, May 2008.

[49] D. P. Anderson, C. Christensen, and B. Allen. Designing a runtime system for volunteer computing. In *Proceedings of the 2006 ACM/IEEE Conference on Supercomputing*, SC '06, page 126–es, New York, NY, USA, 2006. Association for Computing Machinery.

[50] M. Ando and the TAMA collaboration. Current status of TAMA. *Classical and Quantum Gravity*, 19(7):1409–1419, Mar 2002.

[51] T. A. Apostolatos. Search templates for gravitational waves from precessing, inspiraling binaries. *Phys. Rev.*, D52:605–620, 1995.

[52] T. A. Apostolatos, C. Cutler, G. J. Sussman, and K. S. Thorne. Spin induced orbital precession and its modulation of the gravitational wave forms from merging binaries. *Phys. Rev.*, D49:6274–6297, 1994.

[53] R. L. Arnowitt, S. Deser, and C. W. Misner. The Dynamics of general relativity. *Gen. Rel. Grav.*, 40:1997–2027, 2008, gr-qc/0405109.

[54] K. G. Arun, A. Buonanno, G. Faye, and E. Ochsner. Higher-order spin effects in the amplitude and phase of gravitational waveforms emitted by inspiraling compact binaries: Ready-to-use gravitational waveforms. *Phys. Rev.*, D79:104023, 2009, 0810.5336. [Erratum: Phys. Rev.D84,049901(2011)].

[55] G. Ashton et al. BILBY: A user-friendly Bayesian inference library for gravitational-wave astronomy. *Astrophys. J. Suppl.*, 241(2):27, 2019, 1811.02042.

[56] Y. Aso, Y. Michimura, K. Somiya, M. Ando, O. Miyakawa, T. Sekiguchi, D. Tatsumi, and H. Yamamoto. Interferometer design of the KAGRA gravitational wave detector. *Phys. Rev.*, D88(4):043007, 2013, 1306.6747.

[57] B. Aylott et al. Testing gravitational-wave searches with numerical relativity waveforms: Results from the first Numerical INJection Analysis (NINJA) project. *Class. Quant. Grav.*, 26:165008, 2009, 0901.4399.

[58] V. Baibhav, E. Berti, D. Gerosa, M. Mapelli, N. Giacobbo, Y. Bouffanais, and U. N. Di Carlo. Gravitational-wave detection rates for compact binaries formed in isolation: LIGO/Virgo O3 and beyond. *Phys. Rev.*, D100(6):064060, 2019, 1906.04197.

[59] E. Baird, S. Fairhurst, M. Hannam, and P. Murphy. Degeneracy between mass and spin in black-hole-binary waveforms. *Phys. Rev.*, D87(2):024035, 2013, 1211.0546.

[60] J. M. Bardeen, W. H. Press, and S. A. Teukolsky. Rotating Black Holes: Locally Nonrotating Frames, Energy Extraction, and Scalar Synchrotron Radiation. ApJ, 178:347–370, Dec. 1972.

[61] L. Barsotti, P. Fritschel, M. Evans, and S. Gras. Updated Advanced LIGO sensitivity design curve. LIGO-T1800044-v5, Apr 2018.

[62] D. Baskaran and L. P. Grishchuk. Components of the gravitational force in the field of a gravitational wave. *Class. Quant. Grav.*, 21:4041–4062, 2004, gr-qc/0309058.

[63] T. W. Baumgarte, S. A. Hughes, and S. L. Shapiro. Evolving Einstein's field equations with matter: The 'Hydro without hydro' test. *Phys. Rev.*, D60:087501, 1999, gr-qc/9902024.

[64] T. W. Baumgarte and S. L. Shapiro. On the numerical integration of Einstein's field equations. *Phys. Rev.*, D59:024007, 1999, gr-qc/9810065.

[65] T. W. Baumgarte and S. L. Shapiro. Numerical relativity and compact binaries. *Phys. Rept.*, 376:41–131, 2003, gr-qc/0211028.

[66] T. W. Baumgarte and S. L. Shapiro. *Numerical Relativity: Solving Einstein's Equations on the Computer*. Cambridge University Press, 2010. 10.1017/CBO9781139193344.

[67] M. J. Berger and J. Oliger. Adaptive mesh refinement for hyperbolic partial differential equations. *Journal of Computational Physics*, 53(3):484 – 512, 1984.

[68] E. Berti, V. Cardoso, and C. M. Will. Gravitational-wave spectroscopy of massive black holes with the space interferometer lisa. *Phys. Rev. D*, 73:064030, Mar 2006.

[69] L. Blanchet. Gravitational Radiation from Post-Newtonian Sources and Inspiralling Compact Binaries. *Living Rev. Rel.*, 17:2, 2014, 1310.1528.

[70] T. Boch and P. Fernique. Aladin Lite: Embed your Sky in the Browser. In N. Manset and P. Forshay, editors, *Astronomical Data Analysis Software and Systems XXIII*, volume 485 of *Astronomical Society of the Pacific Conference Series*, page 277, May 2014.

[71] A. Bohé, L. Shao, A. Taracchini, A. Buonanno, S. Babak, I. W. Harry, I. Hinder, S. Ossokine, M. Pürrer, V. Raymond, T. Chu, H. Fong, P. Kumar, H. P. Pfeiffer, M. Boyle, D. A. Hemberger, L. E. Kidder, G. Lovelace, M. A. Scheel, and B. Szilágyi. Improved effective-one-body model of spinning, nonprecessing binary black holes for the era of gravitational-wave astrophysics with advanced detectors. Phys. Rev. D, 95(4):044028, Feb 2017, 1611.03703.

[72] A. Bohé et al. Improved effective-one-body model of spinning, nonprecessing binary black holes for the era of gravitational-wave astrophysics with advanced detectors. *Phys. Rev.*, D95(4):044028, 2017, 1611.03703.

[73] A. Bohé, S. Marsat, and L. Blanchet. Next-to-next-to-leading order spin–orbit effects in the gravitational wave flux and orbital phasing of compact binaries. *Class. Quant. Grav.*, 30:135009, 2013, 1303.7412.

[74] C. Bona, J. Masso, E. Seidel, and J. Stela. A New formalism for numerical relativity. *Phys. Rev. Lett.*, 75:600–603, 1995, gr-qc/9412071.

[75] R. Bondarescu, G. Allen, G. Daues, I. Kelley, M. Russell, E. Seidel, J. Shalf, and M. Tobias. The astrophysics simulation collaboratory portal: a framework for effective distributed research. *Future Generation Computer Systems*, 21(2):259 – 270, 2005. Advanced Grid Technologies.

[76] F. Bonnarel, P. Fernique, O. Bienaymé, D. Egret, F. Genova, M. Louys, F. Ochsenbein, M. Wenger, and J. G. Bartlett. The ALADIN interactive sky atlas. A reference tool for identification of astronomical sources. A&AS, 143:33–40, Apr. 2000.

[77] J. M. Bowen and J. W. York. Time-asymmetric initial data for black holes and black-hole collisions. *Phys. Rev. D*, 21:2047–2056, Apr 1980.

[78] M. Boyle et al. The SXS Collaboration catalog of binary black hole simulations. 2019, 1904.04831.

[79] S. Brandt and B. Bruegmann. A Simple construction of initial data for multiple black holes. *Phys. Rev. Lett.*, 78:3606–3609, 1997, gr-qc/9703066.

[80] M. Breschi, S. Bernuzzi, F. Zappa, M. Agathos, A. Perego, D. Radice, and A. Nagar. Kilohertz gravitational waves from binary neutron star remnants: Time-domain model and constraints on extreme matter. *Phys. Rev. D*, 100:104029, Nov 2019.

[81] D. R. Brill and R. W. Lindquist. Interaction energy in geometrostatics. *Phys. Rev.*, 131:471–476, Jul 1963.

[82] D. Brown, S. Fairhurst, B. Krishnan, R. A. Mercer, R. K. Kopparapu, L. Santamaria, and J. T. Whelan. Data formats for numerical relativity waves. 2007, 0709.0093. LIGO-T070072.

[83] B. Bruegmann, W. Tichy, and N. Jansen. Numerical simulation of orbiting black holes. *Phys. Rev. Lett.*, 92:211101, 2004, gr-qc/0312112.

[84] B. Brügmann, J. A. González, M. Hannam, S. Husa, U. Sperhake, and W. Tichy. Calibration of moving puncture simulations. *Phys. Rev. D*, 77:024027, Jan 2008, gr-qc/0610128.

[85] A. Buonanno, Y.-b. Chen, and M. Vallisneri. Detecting gravitational waves from precessing binaries of spinning compact objects: Adiabatic limit. *Phys. Rev.*, D67:104025, 2003, gr-qc/0211087. [Erratum: Phys. Rev.D74,029904(2006)].

[86] A. Buonanno, B. Iyer, E. Ochsner, Y. Pan, and B. S. Sathyaprakash. Comparison of post-Newtonian templates for compact binary inspiral signals in gravitational-wave detectors. *Phys. Rev.*, D80:084043, 2009, 0907.0700.

[87] J. Calderón Bustillo, A. Bohé, S. Husa, A. M. Sintes, M. Hannam, and M. Pürrer. Comparison of subdominant gravitational wave harmonics between post-Newtonian and numerical relativity calculations and construction of multi-mode hybrids. 2015, 1501.00918.

[88] M. Campanelli, C. O. Lousto, P. Marronetti, and Y. Zlochower. Accurate evolutions of orbiting black-hole binaries without excision. *Phys. Rev. Lett.*, 96:111101, 2006, gr-qc/0511048.

[89] M. Campanelli, C. O. Lousto, Y. Zlochower, B. Krishnan, and D. Merritt. Spin Flips and Precession in Black-Hole-Binary Mergers. *Phys. Rev.*, D75:064030, 2007, gr-qc/0612076.

[90] S. Carroll, S. Carroll, and Addison-Wesley. *Spacetime and Geometry: An Introduction to General Relativity*. Addison Wesley, 2004.

[91] G. Carullo et al. Empirical tests of the black hole no-hair conjecture using gravitational-wave observations. *Phys. Rev.*, D98(10):104020, 2018, 1805.04760.

[92] S. Caudill, S. E. Field, C. R. Galley, F. Herrmann, and M. Tiglio. Reduced Basis representations of multi-mode black hole ringdown gravitational waves. *Class.Quant.Grav.*, 29:095016, 2012, 1109.5642.

[93] K. Chakravarti et al. Systematic effects from black hole-neutron star waveform model uncertainties on the neutron star equation of state. *Phys. Rev.*, D99(2):024049, 2019, 1809.04349.

[94] K. Chatziioannou, A. Klein, N. Yunes, and N. Cornish. Constructing Gravitational Waves from Generic Spin-Precessing Compact Binary Inspirals. *Phys. Rev.*, D95(10):104004, 2017, 1703.03967.

[95] M. W. Choptuik. *The Binary Black Hole Grand Challenge Project*, volume 12 of *Astronomical Society of the Pacific Conference Series*, page 305. 1997.

[96] D. Christodoulou. Reversible and irreversible transforations in black hole physics. *Phys. Rev. Lett.*, 25:1596–1597, 1970.

[97] D. Christodoulou and R. Ruffini. Reversible transformations of a charged black hole. *Phys. Rev. D*, 4:3552–3555, Dec 1971.

[98] J. A. Clark, A. Bauswein, N. Stergioulas, and D. Shoemaker. Observing Gravitational Waves From The Post-Merger Phase Of Binary Neutron Star Coalescence. *Class. Quant. Grav.*, 33(8):085003, 2016, 1509.08522.

[99] T. L. S. Collaboration, the Virgo Collaboration, R. Abbott, et al. Open data from the first and second observing runs of advanced ligo and advanced virgo, 2019, 1912.11716.

[100] R. Cotesta, A. Buonanno, A. Bohé, A. Taracchini, I. Hinder, and S. Ossokine. Enriching the Symphony of Gravitational Waves from Binary Black Holes by Tuning Higher Harmonics. *Phys. Rev.*, D98(8):084028, 2018, 1803.10701.

[101] M. W. Coughlin and T. Dietrich. Can a black hole–neutron star merger explain GW170817, AT2017gfo, and GRB170817A? *Phys. Rev.*, D100(4):043011, 2019, 1901.06052.

[102] C. Cutler and E. E. Flanagan. Gravitational waves from merging compact binaries: How accurately can one extract the binary's parameters from the inspiral wave form? *Phys. Rev.*, D49:2658–2697, 1994, gr-qc/9402014.

[103] T. Dietrich, S. Bernuzzi, and W. Tichy. Closed-form tidal approximants for binary neutron star gravitational waveforms constructed from high-resolution numerical relativity simulations. *Phys. Rev. D*, 96(12):121501(R), 2017, 1706.02969.

[104] T. Dietrich et al. Matter imprints in waveform models for neutron star binaries: Tidal and self-spin effects. *Phys. Rev.*, D99(2):024029, 2019, 1804.02235.

[105] T. Dietrich, A. Samajdar, S. Khan, N. K. Johnson-McDaniel, R. Dudi, and W. Tichy. Improving the NRTidal model for binary neutron star systems. 2019, 1905.06011.

[106] K. L. Dooley, J. R. Leong, T. Adams, C. Affeldt, A. Bisht, C. Bogan, J. Degallaix, C. Gräf, S. Hild, J. Hough, A. Khalaidovski, N. Lastzka, J. Lough, H. Lück, D. Macleod, L. Nuttall, M. Prijatelj, R. Schnabel, E. Schreiber, J. Slutsky, B. Sorazu, K. A. Strain, H. Vahlbruch, M. Wąs, B. Willke, H. Wittel, K. Danzmann, and H. Grote. GEO 600 and the GEO-HF upgrade program: successes and challenges. *Classical and Quantum Gravity*, 33(7):075009, Mar 2016.

[107] N. Draper and H. Smith. *Applied regression analysis*. Wiley series in probability and mathematical statistics. Wiley, New York [u.a.], 1966.

[108] O. Dreyer, B. Krishnan, D. Shoemaker, and E. Schnetter. Introduction to isolated horizons in numerical relativity. *Phys. Rev.*, D67:024018, 2003, gr-qc/0206008.

[109] R. Dudi, F. Pannarale, T. Dietrich, M. Hannam, S. Bernuzzi, F. Ohme, and B. Brügmann. Relevance of tidal effects and post-merger dynamics for binary neutron star parameter estimation. *Phys. Rev.*, D98(8):084061, 2018, 1808.09749.

[110] F. W. Dyson, A. S. Eddington, and C. Davidson. IX. A determination of the deflection of light by the sun's gravitational field, from observations made at the total eclipse of May 29, 1919. *Philosophical Transactions of the Royal Society of London. Series A*, 220(571-581):291–333, 1920.

[111] A. Einstein. Zur elektrodynamik bewegter körper. *Annalen der Physik*, 322(10):891–921, 1905.

[112] A. Einstein. Erklärung der Perihelbewegung des Merkur aus der allgemeinen Relativitätstheorie. *Sitzungsber. Preuss. Akad. Wiss. Berlin (Math. Phys.)*, pages 831–839, 1915.

[113] A. Einstein. Grundgedanken der allgemeinen relativitätstheorie und anwendung dieser theorie in der astronomie. *Sitzungsber. Preuss. Akad. Wiss. Berlin (Math. Phys.)*, page 315, 1915.

[114] A. Einstein. Grundgedanken der allgemeinen relativitätstheorie und anwendung dieser theorie in der astronomie. *Sitzungsber. Preuss. Akad. Wiss. Berlin (Math. Phys.)*, page 844–847, 1915.

[115] A. Einstein. Zur allgemeinen relativitätstheorie. *Sitzungsber. Preuss. Akad. Wiss. Berlin (Math. Phys.)*, pages 778–786, 1915.

[116] A. Einstein. Die grundlage der allgemeinen relativitätstheorie. *Ann. Phys*, 354(7):769–822, 1916.

[117] A. Einstein. Näherungsweise Integration der Feldgleichungen der Gravitation. *Sitzungsber. Preuss. Akad. Wiss. Berlin (Math. Phys.)*, pages 688–696, 1916.

[118] A. Einstein. Über Gravitationswellen. *Sitzungsber. Preuss. Akad. Wiss. Berlin (Math. Phys.)*, pages 154–167, 1918.

[119] K. R. Eppley. *The numerical evolution of the collision of two black holes*. PhD thesis, Princeton Univ., NJ., Jan. 1975.

[120] E. Fauchon-Jones, E. Hamilton, C. Hoy, A. Vano-Vinuales, C. Kalaghatgi, D. Yeeles, J. Thompson, L. Terrell London, M. Hannam, and S. Khan. BAM catalogue of binary black hole simulations. In preparation, 2020.

[121] E. J. Fauchon-Jones and lvcnrpy contributors. lvcnrpy. git.ligo.org/waveforms/lvcnrpy, 2018.

[122] G. Faye, S. Marsat, L. Blanchet, and B. R. Iyer. The third and a half post-Newtonian gravitational wave quadrupole mode for quasi-circular inspiralling compact binaries. *Class. Quant. Grav.*, 29:175004, 2012, 1204.1043.

[123] S. E. Field, C. R. Galley, F. Herrmann, J. S. Hesthaven, E. Ochsner, and M. Tiglio. Reduced basis catalogs for gravitational wave templates. *Phys. Rev. Lett.*, 106:221102, 2011, 1101.3765.

[124] S. E. Field, C. R. Galley, J. S. Hesthaven, J. Kaye, and M. Tiglio. Fast prediction and evaluation of gravitational waveforms using surrogate models. *Phys. Rev.*, X4(3):031006, 2014, 1308.3565.

[125] R. T. Fielding. *Architectural Styles and the Design of Network-based Software Architectures*. Ph.D., University of California, Irvine, Irvine, 2000.

[126] É. É. Flanagan and T. Hinderer. Constraining neutron star tidal Love numbers with gravitational wave detectors. *Phys. Rev. D*, 77:021502(R), 2008, 0709.1915.

[127] E. E. Flanagan and S. A. Hughes. Measuring gravitational waves from binary black hole coalescences: 2. The Waves' information and its extraction, with and without templates. *Phys. Rev.*, D57:4566–4587, 1998, gr-qc/9710129.

[128] E. E. Flanagan and S. A. Hughes. The Basics of gravitational wave theory. *New J. Phys.*, 7:204, 2005, gr-qc/0501041.

[129] F. Foucart. Black Hole-Neutron Star Mergers: Disk Mass Predictions. *Phys. Rev.*, D86:124007, 2012, 1207.6304.

[130] F. Foucart, L. Buchman, M. D. Duez, M. Grudich, L. E. Kidder, I. MacDonald, A. Mroue, H. P. Pfeiffer, M. A. Scheel, and B. Szilagyi. First direct comparison of nondisrupting neutron star-black hole and binary black hole merger simulations. *Phys. Rev.*, D88(6):064017, 2013, 1307.7685.

[131] F. Foucart et al. Gravitational waveforms from spectral Einstein code simulations: Neutron star-neutron star and low-mass black hole-neutron star binaries. *Phys. Rev.*, D99(4):044008, 2019, 1812.06988.

[132] F. Foucart, T. Hinderer, and S. Nissanke. Remnant baryon mass in neutron star-black hole mergers: Predictions for binary neutron star mimickers and rapidly spinning black holes. *Phys. Rev.*, D98(8):081501, 2018, 1807.00011.

[133] C. R. Galley and P. Schmidt. Fast and efficient evaluation of gravitational waveforms via reduced-order spline interpolation. 2016, 1611.07529.

[134] GitHub, Inc. and Git LFS contributors. Git Large File Storage. github.com/git-lfs/git-lfs, 2020.

[135] E. Gourgoulhon. 3+1 formalism and bases of numerical relativity. 2007, gr-qc/0703035.

[136] C. Gundlach. Pseudospectral apparent horizon finders: An Efficient new algorithm. *Phys. Rev.*, D57:863–875, 1998, gr-qc/9707050.

[137] T. Günther. Getting started with Git LFS, 2017. about.gitlab.com/blog/2017/01/30/getting-started-with-git-lfs-tutorial/.

[138] S. G. Hahn and R. W. Lindquist. The two-body problem in geometrodynamics. *Annals of Physics*, 29(2):304 – 331, 1964.

[139] M. Hannam, D. A. Brown, S. Fairhurst, C. L. Fryer, and I. W. Harry. When can gravitational-wave observations distinguish between black holes and neutron stars? *Astrophys. J.*, 766:L14, 2013, 1301.5616.

[140] M. Hannam, S. Husa, F. Ohme, and P. Ajith. Length requirements for numerical-relativity waveforms. *Phys. Rev.*, D82:124052, 2010, 1008.2961.

[141] M. Hannam, S. Husa, F. Ohme, D. Muller, and B. Bruegmann. Simulations of black-hole binaries with unequal masses or nonprecessing spins: Accuracy, physical properties, and comparison with post-Newtonian results. *Phys. Rev.*, D82:124008, 2010, 1007.4789.

[142] M. Hannam, S. Husa, D. Pollney, B. Bruegmann, and N. O'Murchadha. Geometry and regularity of moving punctures. *Phys. Rev. Lett.*, 99:241102, 2007, gr-qc/0606099.

[143] M. Hannam, P. Schmidt, A. Bohé, L. Haegel, S. Husa, F. Ohme, G. Pratten, and M. Pürrer. Simple Model of Complete Precessing Black-Hole-Binary Gravitational Waveforms. *Phys. Rev. Lett.*, 113(15):151101, 2014, 1308.3271.

[144] S. Hassani. *Mathematical Physics: A Modern Introduction to Its Foundations*. Springer International Publishing, 2013.

[145] C.-J. Haster, I. Mandel, and W. M. Farr. Efficient method for measuring the parameters encoded in a gravitational-wave signal. *Class. Quant. Grav.*, 32(23):235017, 2015, 1502.05407.

[146] W. K. Hastings. Monte Carlo sampling methods using Markov chains and their applications. *Biometrika*, 57(1):97–109, 04 1970, https://academic.oup.com/biomet/article-pdf/57/1/97/23940249/57-1-97.pdf.

[147] J. Healy, C. O. Lousto, J. Lange, R. O'Shaughnessy, Y. Zlochower, and M. Campanelli. Second RIT binary black hole simulations catalog and its application to gravitational waves parameter estimation. *Phys. Rev.*, D100(2):024021, 2019, 1901.02553.

[148] C. Helstrom, D. Fry, L. Costrell, and K. Kandiah. *Statistical Theory of Signal Detection: International Series of Monographs in Electronics and Instrumentation*. International series of monographs on electronics and instrumentation. Elsevier Science, 2013.

[149] J. Hess. git-annex. git-annex.branchable.com, 2020.

[150] E. Hewitt and R. E. Hewitt. The gibbs-wilbraham phenomenon: An episode in fourier analysis. *Archive for History of Exact Sciences*, 21(2):129–160, Jun 1979.

[151] S. Hild, S. Chelkowski, and A. Freise. Pushing towards the ET sensitivity using 'conventional' technology. 2008, 0810.0604.

[152] S. Hild et al. Sensitivity Studies for Third-Generation Gravitational Wave Observatories. *Class. Quant. Grav.*, 28:094013, 2011, 1012.0908.

[153] T. Hinderer. Tidal Love numbers of neutron stars. *Astrophys. J.*, 677:1216–1220, 2008, 0711.2420.

[154] T. Hinderer, A. Taracchini, F. Foucart, A. Buonanno, J. Steinhoff, M. Duez, L. E. Kidder, H. P. Pfeiffer, M. A. Scheel, B. Szilagyi, K. Hotokezaka, K. Kyutoku, M. Shibata, and C. W. Carpenter. Effects of neutron-star dynamic tides on gravitational waveforms within the effective-one-body approach. *Phys. Rev. Lett.*, 116:181101, May 2016.

[155] K. Hotokezaka, K. Kyutoku, Y.-i. Sekiguchi, and M. Shibata. Measurability of the tidal deformability by gravitational waves from coalescing binary neutron stars. *Phys. Rev.*, D93(6):064082, 2016, 1603.01286.

[156] R. A. Hulse and J. H. Taylor. Discovery of a pulsar in a binary system. ApJ, 195:L51–L53, Jan. 1975.

[157] S. Husa, J. A. Gonzalez, M. Hannam, B. Bruegmann, and U. Sperhake. Reducing phase error in long numerical binary black hole evolutions with sixth order finite differencing. *Class. Quant. Grav.*, 25:105006, 2008, 0706.0740.

[158] S. Husa, M. Hannam, J. A. Gonzalez, U. Sperhake, and B. Bruegmann. Reducing eccentricity in black-hole binary evolutions with initial parameters from post-Newtonian inspiral. *Phys. Rev.*, D77:044037, 2008, 0706.0904.

[159] S. Husa, S. Khan, M. Hannam, M. Pürrer, F. Ohme, X. Jiménez Forteza, and A. Bohé. Frequency-domain gravitational waves from nonprecessing black-hole binaries. I. New numerical waveforms and anatomy of the signal. *Phys. Rev.*, D93(4):044006, 2016, 1508.07250.

[160] K. Jani, J. Healy, J. A. Clark, L. London, P. Laguna, and D. Shoemaker. Georgia Tech Catalog of Gravitational Waveforms. *Class. Quant. Grav.*, 33(20):204001, 2016, 1605.03204.

[161] X. Jiménez-Forteza, D. Keitel, S. Husa, M. Hannam, S. Khan, and M. Pürrer. Hierarchical data-driven approach to fitting numerical relativity data for nonprecessing binary black holes with an application to final spin and radiated energy. *Phys. Rev.*, D95(6):064024, 2017, 1611.00332.

[162] C. Kalaghatgi, M. Hannam, and V. Raymond. Parameter Estimation with a Spinning Multi-Mode Waveform Model: IMRPhenomHM. 2019, 1909.10010.

[163] S. Khan, K. Chatziioannou, M. Hannam, and F. Ohme. Phenomenological model for the gravitational-wave signal from precessing binary black holes with two-spin effects. *Phys. Rev. D*, 100:024059, Jul 2019.

[164] S. Khan, S. Husa, M. Hannam, F. Ohme, M. Pürrer, X. Jiménez Forteza, and A. Bohé. Frequency-domain gravitational waves from nonprecessing black-hole binaries. II. A phenomenological model for the advanced detector era. *Phys. Rev.*, D93(4):044007, 2016, 1508.07253.

[165] S. Khan, F. Ohme, K. Chatziioannou, and M. Hannam. Including higher order multipoles in gravitational-wave models for precessing binary black holes. *Phys. Rev.*, D101(2):024056, 2020, 1911.06050.

[166] L. Kidder et al. Spectral Einstein Code. black-holes.org/SpEC.

[167] L. E. Kidder, C. M. Will, and A. G. Wiseman. Coalescing binary systems of compact objects to (post)**(5/2)-Newtonian order. 3. Transition from inspiral to plunge. *Phys. Rev.*, D47:3281–3291, 1993.

[168] B. Knispel, B. Allen, J. M. Cordes, J. S. Deneva, D. Anderson, C. Aulbert, N. D. R. Bhat, O. Bock, S. Bogdanov, A. Brazier, F. Camilo, D. J. Champion, S. Chatterjee, F. Crawford, P. B. Demorest, H. Fehrmann, P. C. C. Freire, M. E. Gonzalez, D. Hammer, J. W. T. Hessels, F. A. Jenet, L. Kasian, V. M. Kaspi, M. Kramer, P. Lazarus, J. van Leeuwen, D. R. Lorimer, A. G. Lyne, B. Machenschalk, M. A. McLaughlin, C. Messenger, D. J. Nice, M. A. Papa, H. J. Pletsch, R. Prix, S. M. Ransom, X. Siemens, I. H. Stairs, B. W. Stappers, K. Stovall, and A. Venkataraman. Pulsar Discovery by Global Volunteer Computing. *Science*, 329(5997):1305, Sept. 2010, 1008.2172.

[169] K. Kyutoku, S. Fujibayashi, K. Hayashi, K. Kawaguchi, K. Kiuchi, M. Shibata, and M. Tanaka. On the possibility of GW190425 being a black hole–neutron star binary merger. *Astrophys. J.*, 890(1):L4, 2020, 2001.04474.

[170] K. Kyutoku, H. Okawa, M. Shibata, and K. Taniguchi. Gravitational waves from spinning black hole-neutron star binaries: dependence on black hole spins and on neutron star equations of state. *Phys. Rev.*, D84:064018, 2011, 1108.1189.

[171] K. Kyutoku, M. Shibata, and K. Taniguchi. Gravitational waves from nonspinning black hole-neutron star binaries: dependence on equations of state. *Phys. Rev.*, D82:044049, 2010, 1008.1460. [Erratum: Phys. Rev.D84,049902(2011)].

[172] B. D. Lackey, K. Kyutoku, M. Shibata, P. R. Brady, and J. L. Friedman. Extracting equation of state parameters from black hole-neutron star mergers: aligned-spin black holes and a preliminary waveform model. *Phys. Rev.*, D89(4):043009, 2014, 1303.6298.

[173] B. D. Lackey, M. Pürrer, A. Taracchini, and S. Marsat. Surrogate model for an aligned-spin effective-one-body waveform model of binary neutron star inspirals using gaussian process regression. *Phys. Rev. D*, 100:024002, Jul 2019.

[174] B. D. Lackey and L. Wade. Reconstructing the neutron-star equation of state with gravitational-wave detectors from a realistic population of inspiralling binary neutron stars. *Phys. Rev.*, D91(4):043002, 2015, 1410.8866.

[175] J. Lange et al. Parameter estimation method that directly compares gravitational wave observations to numerical relativity. *Phys. Rev.*, D96(10):104041, 2017, 1705.09833.

[176] E. Leaver. An Analytic representation for the quasi normal modes of Kerr black holes. *Proc.Roy.Soc.Lond.*, A402:285–298, 1985.

[177] L. Lehner, M. Huq, and D. Garrison. Causal differencing in adm and conformal adm formulations: A comparison in spherical symmetry. *Phys. Rev. D*, 62:084016, Sep 2000.

[178] LIGO Laboratory. Python Gravitational Wave Interferometer Noise Calculator. git.ligo.org/gwinc/pygwinc.

[179] LIGO Scientific Collaboration. GraceDB. gracedb.ligo.org. (GraceDB API, gracedb.ligo.org/api).

[180] LIGO Scientific Collaboration. LIGO Algorithm Library - LALSuite. free software (GPL), 2018.

[181] L. Lindblom, B. J. Owen, and D. A. Brown. Model Waveform Accuracy Standards for Gravitational Wave Data Analysis. *Phys. Rev.*, D78:124020, 2008, 0809.3844.

[182] T. B. Littenberg and N. J. Cornish. Bayesian inference for spectral estimation of gravitational wave detector noise. *Phys. Rev.*, D91(8):084034, 2015, 1410.3852.

[183] L. London. Modeling ringdown II: non-precessing binary black holes. *arXiv:1801.08208.*, 2018, 1801.08208.

[184] L. London and E. Fauchon-Jones. On modeling for Kerr black holes: Basis learning, QNM frequencies, and spherical-spheroidal mixing coefficients. *Class. Quant. Grav.*, 36(23):235015, 2019, 1810.03550.

[185] L. London, E. Fauchon-Jones, and E. Z. Hamilton. llondon6/positive: charge, Jul 2019. 10.5281/zenodo.3356975.

[186] L. London, S. Khan, E. Fauchon-Jones, C. García, M. Hannam, S. Husa, X. Jiménez-Forteza, C. Kalaghatgi, F. Ohme, and F. Pannarale. First higher-multipole model of gravitational waves from spinning and coalescing black-hole binaries. *Phys. Rev. Lett.*, 120(16):161102, 2018, 1708.00404.

[187] L. London, D. Shoemaker, and J. Healy. Modeling ringdown: Beyond the fundamental quasinormal modes. *Phys. Rev.*, D90(12):124032, 2014, 1404.3197.

[188] A. E. H. Love. The yielding of the earth to disturbing forces. *Proceedings of the Royal Society of London. Series A, Containing Papers of a Mathematical and Physical Character*, 82(551):73–88, 1909, https://royalsocietypublishing.org/doi/pdf/10.1098/rspa.1909.0008.

[189] H. Luck et al. The upgrade of GEO600. *J. Phys. Conf. Ser.*, 228:012012, 2010, 1004.0339.

[190] H. Lueck. The upgrade of GEO 600. In *On recent developments in theoretical and experimental general relativity, astrophysics and relativistic field theories. Proceedings, 12th Marcel Grossmann Meeting on General Relativity, Paris, France, July 12-18, 2009. Vol. 1-3*, pages 1726–1728, 2010, 1004.0338.

[191] M. Maggiore. *Gravitational Waves: Volume 1: Theory and Experiments*. Gravitational Waves. OUP Oxford, 2008.

[192] M. Mapelli and N. Giacobbo. The cosmic merger rate of neutron stars and black holes. *Monthly Notices of the Royal Astronomical Society*, 479(4):4391–4398, 06 2018.

[193] A. Matas, A. Buonanno, T. Dietrich, and T. Hinderer. SEOBNRv4_ROM_NRTidalv2_NSBH: An aligned-spin neutron-star–black-hole waveform in the effective-one-body framework. In preparation, 2020.

[194] D. J. A. McKechan, C. Robinson, and B. S. Sathyaprakash. A tapering window for time-domain templates and simulated signals in the detection of gravitational waves from coalescing compact binaries. *Class. Quant. Grav.*, 27:084020, 2010, 1003.2939.

[195] S. T. McWilliams, B. J. Kelly, and J. G. Baker. Observing mergers of non-spinning black-hole binaries. *Phys. Rev.*, D82:024014, 2010, 1004.0961.

[196] N. Metropolis, A. W. Rosenbluth, M. N. Rosenbluth, A. H. Teller, and E. Teller. Equation of state calculations by fast computing machines. *The Journal of Chemical Physics*, 21(6):1087–1092, 1953, https://doi.org/10.1063/1.1699114.

[197] A. A. Michelson and E. W. Morley. On the relative motion of the Earth and the luminiferous ether. *American Journal of Science*, 34(203):333–345, Nov. 1887.

[198] B. Mikoczi, M. Vasuth, and L. A. Gergely. Self-interaction spin effects in inspiralling compact binaries. *Phys. Rev.*, D71:124043, 2005, astro-ph/0504538.

[199] C. Misner, C. John Archibald Wheeler, U. Misner, K. Thorne, J. Wheeler, W. Freeman, and Company. *Gravitation*. Gravitation. W. H. Freeman, 1973.

[200] E. H. Moore. On the reciprocal of the general algebraic matrix. *Bulletin of the American Mathematical Society*, 26:394–395, 1920.

[201] A. Nagar et al. Time-domain effective-one-body gravitational waveforms for coalescing compact binaries with nonprecessing spins, tides and self-spin effects. *Phys. Rev.*, D98(10):104052, 2018, 1806.01772.

[202] E. T. Newman and R. Penrose. Note on the bondi-metzner-sachs group. *Journal of Mathematical Physics*, 7(5):863–870, 1966, https://doi.org/10.1063/1.1931221.

[203] A. H. Nitz, T. Dent, G. S. Davies, S. Kumar, C. D. Capano, I. Harry, S. Mozzon, L. Nuttall, A. Lundgren, and M. Tápai. 2-OGC: Open Gravitational-wave Catalog of binary mergers from analysis of public Advanced LIGO and Virgo data. 2019, 1910.05331.

[204] A. H. Nitz, A. B. Nielsen, and C. D. Capano. Potential Gravitational-wave and Gamma-ray Multi-messenger Candidate from 2015 October 30. *Astrophys. J.*, 876(1):L4, 2019, 1902.09496. [Astrophys. J. Lett.876,L4(2019)].

[205] L. K. Nuttall. Characterizing transient noise in the LIGO detectors. *Phil. Trans. Roy. Soc. Lond.*, A376(2120):20170286, 2018, 1804.07592.

[206] F. Ohme. Analytical meets numerical relativity - status of complete gravitational waveform models for binary black holes. *Class. Quant. Grav.*, 29:124002, 2012, 1111.3737.

[207] F. Ohme. *Bridging the gap between post-Newtonian theory and numerical relativity in gravitational-wave data analysis*. Doctoral Thesis, Universität Potsdam, 2012. urn:nbn:de:kobv:517-opus-60346.

[208] F. Ohme, M. Hannam, and S. Husa. Reliability of complete gravitational waveform models for compact binary coalescences. *Phys. Rev.*, D84:064029, 2011, 1107.0996.

[209] F. Ohme, P. Hopkins, and S. Anderson. Git annex repository for NR data. `Waveforms/NR/gitannexRepository`, Oct 2016.

[210] J. R. Oppenheimer and G. M. Volkoff. On massive neutron cores. *Phys. Rev.*, 55:374–381, Feb 1939.

[211] Y. Pan, A. Buonanno, A. Taracchini, L. E. Kidder, A. H. Mroué, H. P. Pfeiffer, M. A. Scheel, and B. Szilágyi. Inspiral-merger-ringdown waveforms of spinning, precessing black-hole binaries in the effective-one-body formalism. *Phys. Rev.*, D89(8):084006, 2014, 1307.6232.

[212] V. Pandit and Z. Y. Khairullah. Stepwise regression choosing the proper level of significance. In N. K. Malhotra, editor, *Proceedings of the 1985 Academy of Marketing Science (AMS) Annual Conference*, pages 395–398, Cham, 2015. Springer International Publishing.

[213] F. Pannarale, E. Berti, K. Kyutoku, B. D. Lackey, and M. Shibata. Aligned spin neutron star-black hole mergers: a gravitational waveform amplitude model. *Phys. Rev.*, D92(8):084050, 2015, 1509.00512.

[214] F. Pannarale, E. Berti, K. Kyutoku, B. D. Lackey, and M. Shibata. Gravitational-wave cutoff frequencies of tidally disruptive neutron star-black hole binary mergers. *Phys. Rev.*, D92(8):081504, 2015, 1509.06209.

[215] F. Pannarale, E. Berti, K. Kyutoku, and M. Shibata. Nonspinning black hole-neutron star mergers: a model for the amplitude of gravitational waveforms. *Phys. Rev.*, D88(8):084011, 2013, 1307.5111.

[216] F. Pannarale, L. Rezzolla, F. Ohme, and J. S. Read. Will black hole-neutron star binary inspirals tell us about the neutron star equation of state? *Phys. Rev.*, D84:104017, 2011, 1103.3526.

[217] R. Penrose. A generalized inverse for matrices. *Mathematical Proceedings of the Cambridge Philosophical Society*, 51(3):406–413, 1955.

[218] R. Penrose. Asymptotic properties of fields and space-times. *Phys. Rev. Lett.*, 10:66–68, 1963.

[219] E. Poisson. Gravitational waves from inspiraling compact binaries: The Quadrupole moment term. *Phys. Rev.*, D57:5287–5290, 1998, gr-qc/9709032.

[220] E. Poisson and C. M. Will. Gravitational waves from inspiraling compact binaries: Parameter estimation using second postNewtonian wave forms. *Phys. Rev. D*, 52:848–855, 1995, gr-qc/9502040.

[221] G. Pratten, S. Husa, C. Garcia-Quiros, M. Colleoni, A. Ramos-Buades, H. Estelles, and R. Jaume. Setting the cornerstone for the IMRPhenomX family of models for gravitational waves from compact binaries: The dominant harmonic for non-precessing quasi-circular black holes. 2020, 2001.11412.

[222] W. H. Press, S. A. Teukolsky, W. T. Vetterling, and B. P. Flannery. *Numerical Recipes in C: The Art of Scientific Computing*, pages 204–208. Cambridge University Press, second edition, 1992.

[223] F. Pretorius. Evolution of binary black hole spacetimes. *Phys. Rev. Lett.*, 95:121101, 2005, gr-qc/0507014.

[224] M. Punturo et al. The third generation of gravitational wave observatories and their science reach. *Class. Quant. Grav.*, 27:084007, 2010.

[225] M. Purrer, S. Husa, and M. Hannam. An Efficient iterative method to reduce eccentricity in numerical-relativity simulations of compact binary inspiral. *Phys. Rev.*, D85:124051, 2012, 1203.4258.

[226] M. Pürrer. Frequency domain reduced order models for gravitational waves from aligned-spin compact binaries. *Class. Quant. Grav.*, 31(19):195010, 2014, 1402.4146.

[227] M. Pürrer and C.-J. Haster. Ready for what lies ahead? – Gravitational waveform accuracy requirements for future ground based detectors. 2019, 1912.10055.

[228] M. Rakhmanov, J. D. Romano, and J. T. Whelan. High-frequency corrections to the detector response and their effect on searches for gravitational waves. *Class. Quant. Grav.*, 25:184017, 2008, 0808.3805.

[229] J. Ramsay. How Git Partial Clone lets you fetch only the large file you need, 2020. about.gitlab.com/blog/2020/03/13/partial-clone-for-massive-repositories/.

[230] J. S. Read, C. Markakis, M. Shibata, K. b. o. Uryū, J. D. E. Creighton, and J. L. Friedman. Measuring the neutron star equation of state with gravitational wave observations. *Phys. Rev. D*, 79:124033, Jun 2009.

[231] C. Reisswig and D. Pollney. Notes on the integration of numerical relativity waveforms. *Class. Quant. Grav.*, 28:195015, 2011, 1006.1632.

[232] M. Ruiz, R. Takahashi, M. Alcubierre, and D. Nunez. Multipole expansions for energy and momenta carried by gravitational waves. *Gen. Rel. Grav.*, 40:2467, 2008, 0707.4654.

[233] L. Santamaria et al. Matching post-Newtonian and numerical relativity waveforms: systematic errors and a new phenomenological model for non-precessing black hole binaries. *Phys. Rev.*, D82:064016, 2010, 1005.3306.

[234] B. Sathyaprakash et al. Scientific Objectives of Einstein Telescope. *Class. Quant. Grav.*, 29:124013, 2012, 1206.0331. [Erratum: Class. Quant. Grav.30,079501(2013)].

[235] B. S. Sathyaprakash. LAL - LIGO Scientific Collaboration Algorithm Library. lalsuite@757fd2e, Dec 2004.

[236] B. S. Sathyaprakash and S. V. Dhurandhar. Choice of filters for the detection of gravitational waves from coalescing binaries. *Phys. Rev. D*, 44:3819–3834, Dec 1991.

[237] B. S. Sathyaprakash and B. F. Schutz. Physics, Astrophysics and Cosmology with Gravitational Waves. *Living Rev. Rel.*, 12:2, 2009, 0903.0338.

[238] W. Schiesser. *The Numerical Method of Lines: Integration of Partial Differential Equations*. Elsevier Science, 2012.

[239] W. E. Schiesser and G. W. Griffiths. *A Compendium of Partial Differential Equation Models: Method of Lines Analysis with Matlab*. Cambridge University Press, 2009.

[240] P. Schmidt, M. Hannam, and S. Husa. Towards models of gravitational waveforms from generic binaries: A simple approximate mapping between precessing and non-precessing inspiral signals. *Phys. Rev.*, D86:104063, 2012, 1207.3088.

[241] P. Schmidt, I. W. Harry, and H. P. Pfeiffer. Numerical Relativity Injection Infrastructure. 2017, 1703.01076.

[242] P. Schmidt, F. Ohme, and M. Hannam. Towards models of gravitational waveforms from generic binaries II: Modelling precession effects with a single effective precession parameter. *Phys. Rev.*, D91(2):024043, 2015, 1408.1810.

[243] B. F. Schutz. Networks of gravitational wave detectors and three figures of merit. *Class. Quant. Grav.*, 28:125023, 2011, 1102.5421.

[244] B. F. Schutz and M. Tinto. Antenna patterns of interferometric detectors of gravitational waves - I. Linearly polarized waves. MNRAS, 224:131–154, Jan. 1987.

[245] G. Schwarz. Estimating the Dimension of a Model. *Annals of Statistics*, 6:461–464, July 1978.

[246] Y. Setyawati, M. Pürrer, and F. Ohme. Regression methods in waveform modeling: a comparative study. *Class. Quant. Grav.*, 37(7):075012, 2020, 1909.10986.

[247] M. Shibata and T. Nakamura. Evolution of three-dimensional gravitational waves: Harmonic slicing case. *Phys. Rev. D*, 52:5428–5444, Nov 1995.

[248] M. Shibata and K. Taniguchi. Merger of black hole and neutron star in general relativity: Tidal disruption, torus mass, and gravitational waves. *Phys. Rev.*, D77:084015, 2008, 0711.1410.

[249] D. Shoemaker. Advanced LIGO anticipated sensitivity curves. LIGO-T0900288, Jan 2010.

[250] J. Skilling. Nested sampling. *AIP Conference Proceedings*, 735(1):395–405, 2004, https://aip.scitation.org/doi/pdf/10.1063/1.1835238.

[251] J. Skilling. Nested sampling for general Bayesian computation. *Bayesian Analysis*, 1(4):833–859, 2006.

[252] L. Smarr, A. Cadez, B. S. DeWitt, and K. Eppley. Collision of Two Black Holes: Theoretical Framework. *Phys. Rev.*, D14:2443–2452, 1976.

[253] A. Smith. Managing large files with Git LFS, 2015. github.blog/2015-10-14-managing-large-files-with-git-lfs/.

[254] J. R. Smith. The Path to the enhanced and advanced LIGO gravitational-wave detectors. *Class. Quant. Grav.*, 26:114013, 2009, 0902.0381.

[255] K. Somiya. Detector configuration of KAGRA: The Japanese cryogenic gravitational-wave detector. *Class. Quant. Grav.*, 29:124007, 2012, 1111.7185.

[256] J. S. Speagle. dynesty: A Dynamic Nested Sampling Package for Estimating Bayesian Posteriors and Evidences. *arXiv e-prints*, page arXiv:1904.02180, Apr 2019, 1904.02180.

[257] J. Steinhoff, T. Hinderer, A. Buonanno, and A. Taracchini. Dynamical tides in general relativity: Effective action and effective-one-body hamiltonian. *Phys. Rev. D*, 94:104028, Nov 2016.

[258] D. Stolee. Bring your monorepo down to size with sparse-checkout, 2020. github.blog/2020-01-17-bring-your-monorepo-down-to-size-with-sparse-checkout/.

[259] P. J. Sutton, G. Jones, S. Chatterji, P. Kalmus, I. Leonor, S. Poprocki, J. Rollins, A. Searle, L. Stein, M. Tinto, and M. Was. X-pipeline: an analysis package for autonomous gravitational-wave burst searches. *New Journal of Physics*, 12(5):053034, may 2010, 0908.3665.

[260] L. B. Szabados. Quasi-Local Energy-Momentum and Angular Momentum in General Relativity. *Living Rev. Rel.*, 12:4, 2009.

[261] A. Taracchini, A. Buonanno, Y. Pan, T. Hinderer, M. Boyle, D. A. Hemberger, L. E. Kidder, G. Lovelace, A. H. Mroué, H. P. Pfeiffer, M. A. Scheel, B. Szilágyi, N. W. Taylor, and A. Zenginoglu. Effective-one-body model for black-hole binaries with generic mass ratios and spins. *Phys. Rev. D*, 89:061502, Mar 2014.

[262] A. Taracchini, Y. Pan, A. Buonanno, E. Barausse, M. Boyle, T. Chu, G. Lovelace, H. P. Pfeiffer, and M. A. Scheel. Prototype effective-one-body model for nonprecessing spinning inspiral-merger-ringdown waveforms. *Phys. Rev. D*, 86:024011, Jul 2012.

[263] S. A. Teukolsky. Rotating black holes: Separable wave equations for gravitational and electromagnetic perturbations. *Phys. Rev. Lett.*, 29:1114–1118, Oct 1972.

[264] J. E. Thompson, E. Fauchon-Jones, S. Khan, E. Nitoglia, F. Pannarale, T. Dietrich, and M. Hannam. Modeling the gravitational wave signature of neutron star black hole coalescences. *Phys. Rev. D*, 101(12):124059, 2020, 2002.08383.

[265] K. S. Thorne. Multipole expansions of gravitational radiation. *Rev. Mod. Phys.*, 52:299–339, Apr 1980.

[266] K. S. Thorne. Three hundred years of gravitation. Philosophiae Naturalis, Principia Mathematica, chapter 9, page 368. Cambridge University Press, 1989.

[267] R. C. Tolman. Effect of inhomogeneity on cosmological models. *Proceedings of the National Academy of Sciences*, 20(3):169–176, 1934.

[268] R. C. Tolman. Static solutions of einstein's field equations for spheres of fluid. *Phys. Rev.*, 55:364–373, Feb 1939.

[269] K. W. Tsang, T. Dietrich, and C. Van Den Broeck. Modeling the postmerger gravitational wave signal and extracting binary properties from future binary neutron star detections. *Phys. Rev. D*, 100:044047, Aug 2019.

[270] S. A. Usman, A. H. Nitz, I. W. Harry, C. M. Biwer, D. A. Brown, M. Cabero, C. D. Capano, T. D. Canton, T. Dent, S. Fairhurst, M. S. Kehl, D. Keppel, B. Krishnan, A. Lenon, A. Lundgren, A. B. Nielsen, L. P. Pekowsky, H. P. Pfeiffer, P. R. Saulson, M. West, and J. L. Willis. The PyCBC search for gravitational waves from compact binary coalescence. *Classical and Quantum Gravity*, 33(21):215004, oct 2016, 1508.02357.

[271] M. Vallisneri, J. Kanner, R. Williams, A. Weinstein, and B. Stephens. The LIGO Open Science Center. *J. Phys. Conf. Ser.*, 610(1):012021, 2015, 1410.4839.

[272] V. Varma and P. Ajith. Effects of nonquadrupole modes in the detection and parameter estimation of black hole binaries with nonprecessing spins. *Phys. Rev.*, D96(12):124024, 2017, 1612.05608.

[273] V. Varma, S. E. Field, M. A. Scheel, J. Blackman, D. Gerosa, L. C. Stein, L. E. Kidder, and H. P. Pfeiffer. Surrogate models for precessing binary black hole simulations with unequal masses. *Phys. Rev. Research.*, 1:033015, 2019, 1905.09300.

[274] V. Varma, S. E. Field, M. A. Scheel, J. Blackman, L. E. Kidder, and H. P. Pfeiffer. Surrogate model of hybridized numerical relativity binary black hole waveforms. *Phys. Rev. D*, 99:064045, Mar 2019.

[275] J. Veitch, V. Raymond, B. Farr, W. Farr, P. Graff, S. Vitale, B. Aylott, K. Blackburn, N. Christensen, M. Coughlin, W. Del Pozzo, F. Feroz, J. Gair, C.-J. Haster, V. Kalogera, T. Littenberg, I. Mandel, R. O'Shaughnessy, M. Pitkin, C. Rodriguez, C. Röver, T. Sidery, R. Smith, M. Van Der Sluys, A. Vecchio, W. Vousden, and L. Wade. Parameter estimation for compact binaries with ground-based gravitational-wave observations using the lalinference software library. *Phys. Rev. D*, 91:042003, Feb 2015, 1409.7215.

[276] T. Venumadhav, B. Zackay, J. Roulet, L. Dai, and M. Zaldarriaga. New Binary Black Hole Mergers in the Second Observing Run of Advanced LIGO and Advanced Virgo. 2019, 1904.07214.

[277] R. Wald. *General Relativity*. University of Chicago Press, 1984.

[278] P. Welch. The use of fast fourier transform for the estimation of power spectra: A method based on time averaging over short, modified periodograms. *IEEE Transactions on Audio and Electroacoustics*, 15(2):70–73, June 1967.

[279] K. Yagi and N. Yunes. Approximate Universal Relations for Neutron Stars and Quark Stars. *Phys. Rept.*, 681:1–72, 2017, 1608.02582.

[280] T. Yamamoto, M. Shibata, and K. Taniguchi. Simulating coalescing compact binaries by a new code (sacra). *Phys. Rev. D*, 78:064054, Sep 2008.

[281] J. York, J. W. Kinematics and dynamics of general relativity. In L. L. Smarr, editor, *Sources of Gravitational Radiation*, pages 83–126, Jan. 1979.

[282] F. Zappa, S. Bernuzzi, F. Pannarale, M. Mapelli, and N. Giacobbo. Black-Hole Remnants from Black-Hole–Neutron-Star Mergers. *Phys. Rev. Lett.*, 123(4):041102, 2019, 1903.11622.